

DEVELOPMENT OF A MULTISPECTRAL SENSOR FOR CROP CANOPY
TEMPERATURE MEASUREMENT

A Thesis

presented to

the Faculty of the Graduate School
at the University of Missouri-Columbia

In Partial Fulfillment

of the Requirements for the Degree

Master of Science

by

PHILIP DREW

Dr. Kenneth A. Sudduth, Thesis Supervisor

DECEMBER 2017

The undersigned, appointed by the dean of the Graduate School, have examined the thesis entitled

DEVELOPMENT OF A MULTISPECTRAL SENSOR FOR CROP CANOPY
TEMPERATURE MEASUREMENT

presented by Philip Drew,

a candidate for the degree of master of science,

and hereby certify that, in their opinion, it is worthy of acceptance.

Professor Kenneth A. Sudduth

Professor Allen Thompson

Professor E. John Sadler

ACKNOWLEDGEMENTS

Many people deserve thanks for the assistance they provided during the course of this research. My advisor, Dr. Kenneth Sudduth, provided guidance and support throughout the lifetime of my research. The suggestion and advice by the other members of my committee, Dr. Allen Thompson and Dr. John Sadler were also important. Employees in the Cropping Systems and Water Quality Research Unit, USDA-ARS, Columbia, Missouri, provided assistance in fixture construction and data analysis integral to the completion of this research. Finally, thanks to my family and friends for their support, which supplied me with the confidence needed to accomplish my goals.

TABLE OF CONTENTS

ACKNOWLEDGEMENTS	ii
LIST OF FIGURES	v
LIST OF TABLES	x
ABSTRACT	xi
CHAPTER 1. INTRODUCTION	1
OBJECTIVES	4
CHAPTER 2. REVIEW OF LITERATURE	5
SPATIAL VARIABILITY IN PRECISION AGRICULTURE	5
CROP CANOPY MEASUREMENTS	6
IMAGE PROCESSING	11
SENSOR CALIBRATION	13
CHAPTER 3. DEVELOPMENT OF A MULTISPECTRAL SENSOR FOR CROP TEMPERATURE MEASUREMENT	16
ABSTRACT	16
INTRODUCTION	16
Objectives	20
MATERIALS AND METHODS	20
Instrument Design	20
Calibration	25
Field Trials	30
RESULTS AND DISCUSSION	32
Calibration	32
Field Operation	40
Image Segmentation	45
CONCLUSION	52
CHAPTER 4. APPLICATIONS OF A MOBILE MULTISPECTRAL CROP CANOPY TEMPERATURE SENSOR	54
ABSTRACT	54
INTRODUCTION	54
Objectives	60
MATERIALS AND METHODS	60
Hardware and Platform	60
Experiment Description	62
Image Processing	65
RESULTS AND DISCUSSION	67
Image Processing	67
Plot A Results	72
Plot B Results	79
CONCLUSION	87
CHAPTER 5. CONCLUSIONS	90
SUGGESTIONS FOR FURTHER STUDY	92

APPENDIX 1. ELECTRONIC SCHEMATICS	95
MSICC SCHEMATIC	95
THERMOELECTRIC MODULE CONTROL SYSTEM SCHEMATIC	103
APPENDIX 2. SOFTWARE REFERENCES	104
LIST OF REFERENCES	105

LIST OF FIGURES

Figure		
3.1.	Block diagram of the components and PCB interfaces of the MSICC.	24
3.2.	The populated PCB used in the MSICC system with red arrows denoting the Teensy development board, the Lepton LWIR camera, and the ArduCAM visible camera.	24
3.3.	A side view diagram of the calibration test setup used to create a blackbody approximation for LWIR imaging.	27
3.4.	Test conditions for LWIR camera calibration experiments with data points separated by camera temperature control type.....	30
3.5.	Field of views for IRT and LWIR lenses.....	31
3.6.	Multispectral system deployed on an arm in a soybean field.	32
3.7.	a) Plot of the observed values from the validation set and the predicted values from the linear regression model, equation 3.1, estimating target temperature from camera body and sensor temperature, and camera raw output. b) Plot of the validation residuals from the linear regression model.	36
3.8.	a) Plot of the observed values from the validation set and the predicted values from the quadratic regression model, equation 3.2, relating camera body and sensor temperature, target temperature, and camera raw output. b) Plot of the validation residuals from the quadratic regression model.....	37
3.9.	Plot of measured thermocouple (a) and IRT (b) values with predictive models, equations 3.3 and 3.4 respectively.....	38
3.10.	a) Plot of the observed TC temperatures, adjusted with equation 3.3, and the predicted scene temperatures from the linear regression model, equation 1. b) Plot of the observed TC temperatures, adjusted with equation 3.3, and the predicted scene temperatures from the quadratic regression model, equation 3.2.....	39
3.11.	a) LWIR image of mature soybean plant canopy with soil visible from day 263 of 2016 at 1246 CDT. b) Daytime measurements from day 263, with median and standard deviation of each image, plotted with IRT temperature and hourly air temperature. c) Time-series of histograms of each image plotted with IRT temperature and hourly air temperature	42

Figure

3.12.	a) LWIR image of mature soybean plants with complete canopy and no soil visible from day 268 of 2016 at 1245 CDT b) Daytime measurements from day 263, with median and standard deviation of each image, plotted with IRT temperature and hourly air temperature. c) Time-series of histograms of each image plotted with IRT temperature and hourly air temperature.....	43
3.13.	a) LWIR image of young soybean plants from day 273 of 2016 at 1244 CDT. b) Daytime measurements from day 273, with median and standard deviation of each image, plotted with IRT temperature and hourly air temperature. c) Time-series of histograms of each image plotted with IRT temperature and hourly air temperature.....	44
3.14.	Processing steps for image segmentation. Visible (a) and LWIR (b) images were obtained. The intensity mask (c) was derived from processing the visible image. This binary mask was then applied to the LWIR image to form a region of interest (d). Red arrows note location of the alignment target described in the text.....	46
3.15.	a) Visible image of open canopy, mature soybean scene representative of day 263. b) LWIR Image displaying contrast map of scene c) Thermal image created after applying equation 3.2 to LWIR pixels d) Segmented thermal image produced from processing visible and thermal images.....	47
3.16.	a) Visible image of complete canopy, mature soybean scene representative of day 268 b) LWIR Image displaying contrast map of scene c) Thermal image created after applying equation 2 to LWIR pixels d) Segmented thermal image produced from processing visible and thermal images.....	48
3.17.	a) Visible image of young soybean scene representative of day 273 b) LWIR Image displaying contrast map of scene c) Thermal image created after applying equation 2 to LWIR pixels d) Segmented thermal image produced from processing visible and thermal images.....	49
3.18.	Difference in median temperature between the segmented and full thermal images for (a) mature, open canopy, (b) mature complete canopy, and (c) young plants with exposed soil.....	51
4.1.	Diagram of tripod and boom structure used to capture images with the MSICC up to four rows away from the vehicle position.....	62
4.2.	The MSICC is shown capturing data within Plot A. The flags in the photo on the right denote a location to be sampled.....	63

Figure

4.3.	a) Imaging locations within plot A with location code. b) Locations of points within each B plot.	65
4.4.	A LWIR image overlaid on a corrected visible image using the in-field target as alignment.	66
4.5.	a) Visible camera image cropped to LWIR camera field of view on June 9. b) LWIR image with calibration applied. c) Segmented image using ExG technique. d) Segmented image using ExGR technique.....	67
4.6.	Left: Visible camera image cropped to LWIR camera field of view on June 12. Center: LWIR image with calibration applied. Right: Segmented image using ExG technique.	69
4.7.	a) Visible camera image cropped to LWIR camera field of view on June 15. b) LWIR image with calibration applied. c) Segmented image using ExG technique. d) Segmented image using ExGR technique.....	70
4.8.	Left: Visible camera image cropped to LWIR camera field of view on June 19. Center: LWIR image with calibration applied. Right: Segmented image using ExGR technique.	70
4.9.	Left: Visible camera image cropped to LWIR camera field of view on June 24. Center: LWIR image with calibration applied. Right: Segmented image using ExGR technique.	71
4.10.	Left: Visible camera image cropped to LWIR camera field of view on June 27. Center: LWIR image with calibration applied. Right: Segmented image using ExGR technique.	71
4.11	Data recorded within Plot A on June 9. Each point represents an average value from four measurements: LWIR full and segmented temperatures, IRT temperature, and percentage cover. Sections are labeled with codes described in figure 4.3a.	73
4.12.	Data recorded within Plot A on June 12. Each point represents an average value from four measurements: LWIR full and segmented temperatures, IRT temperature, and percentage cover. Sections are labeled with codes described in figure 4.3a.....	74
4.13.	Data recorded within Plot A on June 15. Each point represents an average value from four measurements: LWIR full and segmented temperatures, IRT temperature, and percentage cover. Sections are labeled with codes described in figure 4.3a.....	74

Figure

4.14.	Data recorded within Plot A on June 19. Each point represents an average value from four measurements: LWIR full and segmented temperatures, IRT temperature, and percentage cover. Sections are labeled with codes described in figure 4.3a.	75
4.15.	Data recorded within Plot A on June 24. Each point represents an average value from four measurements: LWIR full and segmented temperatures, IRT temperature, and percentage cover. Sections are labeled with codes described in figure 4.3a.	76
4.16.	Data recorded within Plot A on June 27. Each point represents an average value from four measurements: LWIR full and segmented temperatures, IRT temperature, and percentage cover. Sections are labeled with codes described in figure 4.3a.	77
4.17.	Difference between segmented median temperature and current air temperature plotted by location within each treatment area. Each point is an average of three measurements taken on the given day. The codes for location within plot A are shown in figure 4.3a. Plot position increases towards the south.	78
4.18	Data recorded within Plot B on June 12. Each point represents an average value from four measurements: LWIR full and segmented temperatures, IRT temperature, and percentage cover. Plot changes are denoted by a section break.	80
4.19	Data recorded within Plot B on June 15. Each point represents an average value from four measurements: LWIR full and segmented temperatures, IRT temperature, and percentage cover. Plot changes are denoted by a section break.	81
4.20	Data recorded within Plot B on June 19. Each point represents an average value from four measurements: LWIR full and segmented temperatures, IRT temperature, and percentage cover. Plot changes are denoted by a section break.	81
4.21	Data recorded within Plot B on June 22. Each point represents an average value from four measurements: LWIR full and segmented temperatures, IRT temperature, and percentage cover. Plot changes are denoted by a section break.	82
4.22	Data recorded within Plot B on June 27. Each point represents an average value from four measurements: LWIR full and segmented temperatures, IRT temperature, and percentage cover. Plot changes are denoted by a section break.	83

Figure

4.23. The difference between the median of the segmented temperature and air temperature at the eight locations within each plot is plotted for June 12, 15, and 19. Two measurements at each location are shown for June 12, representing the two separate boom lengths used. See figure 4.3b for location of each point.84

LIST OF TABLES

Table

3.1.	RMSE and R^2 for linear and quadratic equations developed from the calibration set and equation applied to the randomly selected validation set.	34
4.1.	Significance of F tests for TD, NS, and their interaction on LWIR median temperatures for segmented and full images, IRT values, and percent of image used in segmentation. For each dependent variable, bolded data are significantly different at $\alpha=0.05$	85
4.2.	Least squares means for LWIR median temperatures for segmented and full images, IRT values, and percent of image used in segmentation. These are separated by date and classified by TD and NS. Low TD plots B1 and B2 are depth 1, deep TD plots B3 and B4 are depth 2. Measurements taken on the northern side of the plot are listed as 1, south as 2. No interaction terms are shown because no significance was found. For each dependent variable, data within a column with the same superscript are not significantly different at $\alpha=0.05$	86

ABSTRACT

The Multispectral System for Imaging of a Crop Canopy (MSICC) that combines a miniature long wavelength infrared (LWIR) camera with a visible camera was developed to capture a field of view and derive a plant specific temperature measurement. The overall project included the development of electronics and firmware used to integrate the two cameras into a deployable system, the calibration that converted LWIR images into thermal measurements, the post-processing techniques used on visible camera images, and the field operation of the instrument as a static and mobile device.

The electronic system used a microprocessor to control the operations of the LWIR and visible cameras and to save and display images. The LWIR camera was calibrated for thermal measurement to an accuracy of 0.65 °C by relating pixel output to a temperature measurement. The visible camera, through processing to identify plants within an image, provided a binary mask to identify crop/non-crop components within its field of view. The mask was then used to obtain a region of interest (ROI) from the thermal image over which data were integrated to create a crop temperature measurement.

The MSICC, paired with an infrared thermometer for comparison, collected data at high temporal resolution on three different soybean plots during September and October 2016. It was capable of removing shaded areas and soil from the ROI, based upon monochrome image intensity, from thermal images to produce temperature measurements more representative of the plant canopy.

Hardware, software, and image processing improvements facilitated use of the MSICC as a mobile sensor to identify spatial variability. This instrument gathered high

spatial resolution data on two different sets of corn plots during June 2017. The effectiveness of two color-based vegetative indices for defining the ROI was gauged on plots with different percent canopy cover. The MSICC was able to discern a significant difference in temperature between plants growing in shallow and deep topsoil plots on a day with high temperature and low soil moisture. Due to its ability to remove non-crop background, this instrument should be able to provide accurate crop temperature measurements earlier in the growing season than other methods.

CHAPTER 1

INTRODUCTION

Precision agriculture involves the quantification of site-specific properties to inform management of inputs so they can be applied at the right place and the right time within a field (Mulla, 2013). Such practices require the measurement of in-field variability, which is influenced by biological or chemical factors, caused by weather or topography, or driven by man-made changes. Quantifying these properties and their effects on agricultural practices requires the capture and application of spatially and temporally high resolution data.

Variable rate technologies use measured field scale variability to create maps that can be used by application equipment for dynamic control of water and nutrient application. Monitoring the canopy of a crop can quantify stress variability throughout a field that can relate to landscape or input factors. The temperature of a plant in relation to other plants or ambient temperature can be used as one such stress indicator (Tanner, 1963). A well-watered plant transpires, and its evaporation cools its leaves. A water stressed plant contracts its leaf stomata, restricting transpiration, reducing latent energy loss, and increasing temperature to satisfy its energy balance.

Spectral reflectance indices in visible and near-infrared wavelength ranges and crop canopy temperature measurements by the use of thermographic or radiometric methods, generally in the long wavelength infrared (LWIR) 8-14 μ m wavelength range have been used to identify stress within a crop (Fuchs and Tanner, 1966; Bartholic et al., 1972; Bockhold et al., 2011). Ground-based canopy temperature measurement has been widely practiced using non-contact single point radiometric sensors, such as infrared

thermometers (IRT), that can unobtrusively give accurate measurements of a single point. The capability of measuring temperature on a moving platform is useful in determining a water stress index for scheduling irrigation. To maximize accuracy of these single point sensors requires measurements be obtained without the influence of non-crop components. Because soil temperature can be much higher than plant and ambient temperature, accurately estimating canopy temperature in this manner requires eliminating the effect of the soil background in the sensor's field of view. Thus, a complete canopy is ideal in order to make the most accurate measurements of plant temperature with a single point sensor. These sensors, robust and economical, have been implemented with a high temporal resolution (Sadler et al., 2002; O'Shaughnessy et al., 2012).

A thermal imager is capable of capturing temperature measurements of a crop with higher spatial resolution than a single point sensor. These cameras make it possible to gather data on spatial variability of crop stress from a large area. Pairing a thermal camera that can read the temperature of a spot with a visible light camera allows the capture of canopy temperature measurements by discerning a region of interest through image processing. The increased resolution of a thermal imager increases cost as well as sensitivity of its environment. Pairing two high resolution images together also requires more equipment and processing abilities, so most imager-based experiments have focused on capturing high resolution spatial data at the cost of temporal resolution.

Innovations in uncooled LWIR sensor technology have sped the adoption of such sensors in proximal sensing. LWIR camera sensors produce a representation of their sensor's radiometric response. The generated output signal of each pixel is related to the

radiant flux between it and the scene temperature (DeWitt and Nutter, 1988). Uncooled LWIR cameras can be calibrated at the factory, but high accuracy in specific applications requires additional calibration tailored to the environment they will be used in. To calibrate a LWIR camera to be used as a thermal imager, the radiant flux of a scene needs to be known and related to the generated output signal of the camera itself (Budzier and Gerlach, 2015).

Machine vision techniques have been utilized in precision agriculture to discriminate areas within an image based upon vegetative properties. This can be done using indices that identify whether a pixel is part of a plant or not based upon its intensity or color relative to the entire image. Methods are chosen based upon processing time and computational power available. The performance of each index varies based upon lighting conditions, shadows, and the complexity of the background (Hamuda et al., 2016).

Packaging a visible and a LWIR camera together would make a multispectral imaging system with the capability of capturing crop canopy temperature data at high spatial resolution. Using miniature cameras and incorporating them into a compact system for data logging in the field would lead to an instrument that could be installed within a field to record data at high temporal resolution. Such a system would be an economical approach to deploying an array of sensors, similar to the way IRTs have been utilized. The individual resolution of each miniature sensor might not be as high, but its portability and high sampling capabilities would allow for high-resolution mapping of variability in a field throughout a growing season.

Objectives

The overall objective of this research was to create a multispectral system capable of accurately measuring the temperature of a plant canopy by discriminating crop from non-crop areas within a field of view. This system could then be used to identify variability of plant stress throughout a field. The specific objectives were:

- Develop an electronic system capable of capturing multispectral images from board level LWIR and visible cameras with high temporal resolution from either a static location within a field or mounted on a mobile platform with high spatial resolution, for the purpose of measuring crop canopy temperature.
- Design and perform a radiometric calibration procedure that produces a model relating raw camera output to temperature.
- Evaluate vegetative indices for creating a region of interest that identifies a plant within the field of view of a visible image.
- Create post-processing procedures that combine a region of interest defined by the visible image with radiometric interpretations of LWIR images to produce a meaningful temperature measurement of a crop within a field of view.
- Demonstrate within-field use of the instrument to identify spatial variability in canopy temperature.

CHAPTER 2

REVIEW OF LITERATURE

Spatial Variability in Precision Agriculture

Economic pressure on agriculture has driven the adoption of technologies that help lower the cost of crop production while increasing crop yields. Furthermore, efforts to reduce environmental impacts and create sustainable farming practices have also been a catalyst for innovation (Adamchuck et al., 2011). Precision agriculture's goal is to create a management system that uses site-specific properties to determine the correct inputs at the right place at the right time (Mulla, 2013). Such practices require the measurement of in-field variability, which is influenced by biological or chemical factors, caused by weather or topography, or driven by man-made changes. Precision agriculture seeks to quantify this variability by utilizing sensor technologies to capture data with high spatial and temporal resolution. (Lee et al., 2010).

Traditional farming practices do not account for spatial variability and manage an entire field as a single zone, applying inputs uniformly. Therefore, management practices for a field base input rates only on year to year variability, or apply inputs at a given rate without regard to variability. Precision agriculture looks to break the field into separate management zones to appropriately manage the landscape. Manual collection of samples, such as soil samples, and subsequent laboratory analysis for chemical, biological, and physical properties have been practiced for decades (Adamchuck et al., 2011). Identifying site-specific properties in a field through manual sampling is time and cost intensive. It is also difficult to obtain enough samples to capture landscape variability.

Capturing variability during a growing season is difficult using manual methods and requires expansion into automated domains. Real-time data collection also allows characterization of higher spatial resolutions than manual methods. Quantifying spatial and temporal variability can be used in site-specific management through the use of variable rate technology for irrigation and nutrient application (Lee et al., 2010). For example, it has been shown that a sensor-based approach for nitrogen application in corn was more effective than producers' standard practices (Scharf et al., 2011).

Electronic sensors can reduce errors and provide a way to make repeatable, accurate measurements from field to field. Proximal or aerial remote sensors can be used to capture this data that may then be applied for identifying targets for inputs or recording changes. Satellite based remote sensing has been used in agriculture to measure interaction of electromagnetic radiation with soil and vegetation. Remotely sensed data is capable of providing useful spectral data for precision agriculture management, but it is reliant on cloud free conditions and consistent irradiance between measurements. Lag time between data acquisition and availability is often greater compared to proximal sensing and the data require calibrating and correcting for true reflectance and atmospheric interference. Ground based proximal sensing allows real-time data gathering and processing that can be used in site specific management of inputs (Mulla, 2013).

Crop Canopy Measurements

Crop canopy measurements have become a way to capture crop stress throughout a field within a growing season. Approaches to plant stress detection have focused on spectral reflectance indices in visible and near-infrared wavelength ranges and crop canopy temperature measurements by the use of thermographic or radiometric methods,

generally in the long wave infrared (LWIR) 8-14 μ m wavelength range (Fuchs and Tanner, 1966; Bartholic et al., 1972; Bockhold et al., 2001).

Monitoring temperature of a plant in relation to other plants or ambient temperature can be used as a stress indicator (Tanner, 1963). Canopy temperature provides an indicator of plant and soil water status. Due to the large latent heat of vaporization relative to heat capacity, a plant uses transpiration to cool its leaves. Reduction in soil moisture results in a decrease of transpiration and an increase in leaf temperature to satisfy the energy balance of the system. (Van Bavel et al., 1965)

The energy flux, R , of a given band of electromagnetic radiation, in this case 8-14 μ m, from a surface of emissivity ϵ , is related to the surface temperature, T in degrees K, by

$$R = \epsilon \sigma T^4 \quad (2.1)$$

where σ is the Stefan-Boltzman constant.

By correcting for the emissivity of the plant surface, Fuchs and Tanner (1963) showed that an infrared thermometer could be used to accurately determine the temperature of a canopy. Early experiments by Wiegand and Namken (1966) used a hand-held radiometer to measure cotton leaf temperature and determine variations in plant moisture stress. It was noted that solar radiation had a stronger influence on leaf temperature than air temperature at the time of measurement.

Water stress indices were developed to more effectively relate measured canopy temperatures to plant stress. One such index, the crop water stress index (CWSI), was formulated by Jackson et al. (1981) and has been applied to irrigation scheduling for crops including soybean, vineyards, and sorghum (Nielsen, 1990; Möller et al., 2007;

O'Shaughnessy et al., 2012). The CWSI has been mostly applied in arid and semi-arid environments, while other temperature threshold calculations derived from multi-day temperature measurements have been used in more humid environments (Bockhold et al., 2011; Wanjura et al., 1995).

Plant stress of this nature can also be tied to such factors as soil depth and even leaf diseases (Lee et al., 2010). Sensing of canopy temperature has been widely practiced using single point radiometric sensors, such as infrared thermometers (IRT). Canopy temperature methods are useful in determining a water stress index for scheduling irrigation. Sadler et al. (2002) accomplished this by mounting multiple IRTs on a center pivot irrigation system to measure temperature of corn and identify spatial variations. The spatial variability of crop water stress has been mapped throughout a field (O'Shaughnessy et al., 2011a).

Later approaches to monitoring canopy temperature have integrated sensors into wireless mesh networks to provide remote data acquisition. A wireless sensor network mounted on a moving irrigation pivot was used to automate irrigation scheduling. Feedback provided from sensor measurements on remote nodes was used to make irrigation decisions throughout a growing season (O'Shaughnessy and Evett, 2013).

Accurately measuring canopy temperature with IRTs requires eliminating the effect of the soil background in the sensor's field of view. One approach for minimizing soil background is to mount the IRT at an angle from vertical and pointed toward the crop row (Sadler et al., 2002; Bockhold et al., 2011). In an attempt to reduce errors from non-crop components introduced by the excess height of an irrigation pivot, O'Shaughnessy et al. (2011b) integrated an industrial IRT with a narrow field of view into a wireless

sensor network. It was found the accuracy was comparable to hand-held and wired IRTs, but the varying temperature of the sensor when used in an outdoor environment produced inconsistent measurements. An IRT is only a single point measurement, requiring many sensors and the uniformity provided by a complete canopy to attain adequate resolution within a field (Sadler et al., 2002; Cohen et al., 2005). Increasing the resolution of the sensor through the use of thermal cameras improves spatial information and allows quantification of intra-field-of-view thermal variations (Gonzalez-Dugo et al., 2012).

Thermal imaging has been used as a way to spatially identify changes in crop stress. Bartholic et al. (1972) showed that airborne thermal scanners could create thermal images of entire fields from altitudes of several hundred meters. These airborne thermal scanners were used to determine differences in water stress of cotton in various treatments. With the development of two-dimensional radiometric arrays, attempts were made to pair thermal cameras with visible and near-infrared (NIR) imagers to predict surface temperature measurements without the need of full ground cover. The capture of visible and NIR reflectance images facilitated calculation of vegetative indices that could be used to estimate the percentage of crop captured within an image. An index was created to use the percentage of ground cover to determine the influence of vegetation and to estimate crop temperature from airborne sensors (Clarke, 1997; Moran et al. 1994).

Advances in digital imaging in the LWIR and visible spectra made it possible to segment a thermal image based upon a visible image aligned with the same field of view (Cohen et al., 2005). Vegetation indices could be used to identify a region of interest within the visible image that then could be applied to segment the non-crop area included

within the thermal image (Lee et al., 2010). Image segmentation provided improved accuracy compared to the approach of calculating crop temperature based on percentage of cover within a field of view as was done by Clarke (1997). This multispectral method is not limited by a full canopy or crop growth stage (Zia et al., 2013; Mangus et al., 2016). However, implementing this method has been more cumbersome than the use of IRT's, requiring more equipment and processing capabilities.

Thermal imaging of a crop canopy from above requires that a sufficient altitude over the crop be attained to capture a wide area in a field of view. Thermal imagers have been used in vineyards while mounted 15m above the canopy on truck cranes, producing a resolution of 1.7 cm/pixel (Möller et al., 2007). When imaging pistachio trees, Gonzalez-Dugo et al. (2015) used an unmanned aerial vehicle (UAV) to meet to this height requirement. The large physical size of trees along with discontinuous canopies makes it possible to use systems that capture a larger field of view with a lower resolution, such as 12 cm (Gonzalez-Dugo et al., 2012). Although thermal imaging has been used on agronomic crops in a greenhouse (Mangus et al., 2016), previous field-based approaches have been focused on tree and vine crops.

Within a field, the practical use of thermographic and thermometric approaches to mapping variability has encountered challenges. The high cost of use of thermal imaging systems, paired with the high resolutions required for the physical characteristics of the crop canopy has limited the use of this approach in grain crops. Infrared thermometers can be mounted on in-field equipment, but there are limitations in this approach, as the field of view of the IRT needs to be positioned to include only crop

components, which limits measurement during early crop growth stages (O'Shaughnessy et al., 2011b).

Image Processing

Machine vision has been utilized in precision agriculture to discriminate areas within an image based upon vegetative properties. Algorithms that can automatically accomplish this can be used for mechanical or chemical site-specific treatments (Guijarro et al., 2011). Hamuda et al. (2016) reviewed methods of identifying vegetation contained within a color image. The first stage of a two-step process was to apply pre-processing procedures such as color correction and contrast enhancement. In the second stage, a binary image was formed from classifying each pixel as background or as a plant (Meyer and Neto, 2008). There are three primary approaches relied on for this extraction: color index-based, threshold based, and learning based (Hamuda et al., 2016).

Commercial digital cameras provide an image output in which each pixel value is composed of components of red, green, and blue (RGB). Chromatic coordinates, r , g and b , are derived from the normalized RGB components, R^* , G^* , and B^* . These chromatic coordinates are used to create indices that focus on specific colors of interest.

$$R^* = \frac{R}{R_{max}}, \quad G^* = \frac{G}{G_{max}}, \quad B^* = \frac{B}{B_{max}} \quad (2.2)$$

where:

R , G , and B are the separate color components of each specific pixel

R_{max} , G_{max} , and B_{max} are the maximum values of each color component within an image

$$r = \frac{R^*}{R^*+G^*+B^*}, \quad g = \frac{G^*}{R^*+G^*+B^*}, \quad b = \frac{B^*}{R^*+G^*+B^*} \quad (2.3)$$

Woebbecke et al. (1995) concluded from a comparison of several color vegetative indices that the Excess Green Index (ExG) was most successful due to its near-binary output separating plant from soil.

$$ExG = 2g - r - b \quad (2.4)$$

Meyer et al. (1999) used the Excess Red Index (ExR) as vegetative index coupled with shape parameters to identify types of plants within an image.

$$ExR = 1.3r - g \quad (2.5)$$

Otsu (1979) developed a method that converted pixels from a grayscale image to binary values based on intra-image intensity. Segmentation of the image was accomplished by deriving a threshold that treated the image histogram as bimodal, separating foreground and background by reducing in-class variance. Although this method is widely used, it suffers from mis-identification of pixels and slow processing when compared with using the mean intensity within an image for object discrimination (Hamuda et al., 2016; Guijarro et al., 2011). Meyer and Neto (2008) tested the efficacy of applying Otsu's method for thresholding to ExG. This was compared against the normalized difference index (NDI; Perez et al., 2000), and the creation of a binary image from subtracting a modified version of ExR vegetative index from ExG with a threshold set at zero.

$$NDI = \frac{G-R}{G+R} \quad (2.6)$$

$$ExG - ExR = 3g - 2.3r - b \quad (2.7)$$

It was found that ExG-ExR and ExG+Otsu had similar performance with around 90% success when compared with manually processed images. The ExG-ExR identified singular plants in a variety of backgrounds well because ExG is heavily weighted by soil.

Learning-based approaches have provided slight improvements in segmentation in varying illumination conditions through clustering to extract plant textures and the use of alternate color spaces besides RGB. These adaptive approaches require more complex computations, and as such, use for in-field applications has been limited. Overall, the performance of each method has varied based upon lighting conditions, shadows, and the complexity of the background (Hamuda et al., 2016).

Sensor Calibration

A radiometer measures radiant flux in the portion of the electromagnetic spectrum that the sensor is sensitive to. Non-contact thermometers, such as IRTs, output a value that must be calibrated to temperature. Bugbee et al. (1998) created a calibration experiment by imaging a water bath while recording its temperature with a contact thermometer. Water was used because it has an emissivity similar to that of a healthy plant, $\epsilon \approx 0.98$. This calibration procedure used water as a blackbody approximation and assumed that the temperature of the sensor did not affect the IRT output. In this method, the resolution and accuracy of the thermocouple that measured water temperature was the limiting factor. Calibrating a thermal imager is more involved as it has an entire array of sensors that need to be corrected and calibrated. Bower et al. (2009) showed that a medium wavelength infrared camera could be calibrated in a similar fashion by using water as an economical temperature-controlled target.

An uncooled LWIR imager does not record temperature, but only a representation of the radiometric response from its sensor. The output signal generated by each pixel is related to the radiant flux between it and the scene temperature (DeWitt and Nutter,

1988). To create a radiometric calibration of a LWIR camera the radiant flux of a scene needs to be known and related to the output signal generated by the camera (Budzier and Gerlach, 2015). In operation, each pixel, which is a single sensor itself, drifts due to physical properties of the sensor and the influence of other parts of the camera (housing, electronics, and neighboring pixels) causing variation in its recording of the raw value (Budzier and Gerlach, 2015). To compensate for this, a non-uniformity correction (NUC) exposes the entire array to a known value. In practice this is done by the closing of a shutter and capturing the response or image.

The NUC compensates for the internal variability of the camera, but uncooled LWIR cameras are influenced by environmental temperatures as well. Nugent et al. (2013) were able to calibrate a thermal camera with an accuracy of 0.75°C , better than the manufacturers specified 2°C , for use in an outdoor environment. This was accomplished by forming a mathematical model to compensate for the changing temperature a camera would see in a field application. The error in this experiment was primarily attributed to the emissivity and temperature of the calibration source (blackbody approximation). A detailed calibration, requiring multiple steps, is necessary before using a thermal camera as a precise instrument.

Summary

Quantifying the variability in attributes that affect crop growth is a step toward reducing the environmental and economic costs of agriculture. Instantaneous temperature measurements by IRTs have been used to identify crop characteristics and schedule

irrigation. These non-contact temperature sensors are robust and economical enough to be installed on in-field infrastructure to obtain high temporal resolution data.

LWIR sensors have been calibrated to be used as thermal imagers in outdoor environments, whether for environmental monitoring or capturing real-time agricultural data. Coupling a visible spectrum camera with a thermal camera allows the capture of canopy temperature measurements by discerning a region of interest through image processing. These thermographic based experiments have been focused on capturing high resolution spatial data at specific times of day, resulting in limited temporal resolution.

CHAPTER 3

DEVELOPMENT OF A MULTISPECTRAL SENSOR FOR CROP

TEMPERATURE MEASUREMENT

ABSTRACT

A system has been developed that combines a miniature long wavelength infrared (LWIR) camera with a visible, or RGB, camera to capture a field of view and derive a plant-specific temperature measurement. This chapter encompasses the electronic and software development of the instrument, including calibration, field operation, and post-processing of data. Calibration of the LWIR camera was accurate to 0.65°C, when relating pixel output to a thermal measurement, allowing it to act as a thermal camera. The visible camera, through processing to identify plants within an image, provided a binary mask to identify crop/non-crop components within its field of view. The mask was then used to obtain a crop-only region of interest (ROI) from the thermal image, over which data were integrated to create a temperature measurement. This instrument was tested against an infrared thermometer on three different plots during September and October 2016. It was capable of removing shaded areas and soil from thermal images to produce temperature measurements more representative of the plant canopy.

INTRODUCTION

Proximal quantification of spatial and temporal variability has precision agriculture applications in controlling variable rate technology. Real-time quantification of in-field variables can also be used to create maps to inform management decisions. Determining within-season crop stress through optical canopy measurements has been

used to identify within-field variability. Specifically, monitoring temperature of a plant in relation to ambient temperature can be used as a stress indicator (Tanner, 1963). A well-watered plant transpires, and its evaporation cools its leaves. A water stressed plant contracts its leaf stomata, reducing transpiration and raising its temperature to satisfy its energy balance. Canopy temperature provides an indicator of this response to stress. This relationship has been related to soil water content and used by Jackson et al. (1981) to formulate a crop water stress index that has been applied to irrigation scheduling (Möller et al., 2007; O'Shaughnessy et al., 2011b). Plant stress of this nature can also be tied to such factors as soil depth and even leaf diseases (Lee et al., 2010).

Approaches to plant stress detection have focused on spectral reflectance indices in visible and near-infrared wavelength ranges and crop canopy temperature measurements by the use of thermographic or radiometric methods, generally in the long wave infrared (LWIR) 8-14 μ m wavelength range (Fuchs and Tanner, 1966). Sensing of canopy temperature has been widely practiced using single point radiometric sensors, such as infrared thermometers (IRT). Canopy temperature methods are useful in determining a water stress index for scheduling irrigation. To garner useful information about spatial variability throughout a field, instruments need to be deployed to capture data spatially and for significant periods of time. Sadler et al. (2002) utilized a center pivot irrigation tower to mount multiple IRTs to measure changes in temperature and map spatial variability. There are limitations to IRT application because the field of view can include non-crop components, particularly soil, which can make the plant canopy temperature measurement inaccurate. Accurately estimating canopy temperature in this manner requires eliminating the effect of the soil background in the field of view of the

sensor. Thus, a complete canopy is desirable to make the most accurate measurements of plant temperature with an IRT.

Thermal imaging has been used to measure temperature within a field of view and to identify parts of the image that are non-crop components. A thermal infrared camera captures electromagnetic emission of a surface, which would be critical in identifying a stressed plant (Cohen et al., 2005). Visible images capture light reflected from a surface, allowing identification of soil or shaded leaves within a field of view (Lee et al. 2010). By compiling these two spectral images together, it is possible to segment the region of interest (i.e., unshaded plant), eliminating the unwanted noise that would contribute to error in an aggregate measurement. This multispectral method is not limited by a full canopy or crop growth stage (Zia et al., 2013; Mangus et al., 2016). However, implementation of this method has been more cumbersome than the use of IRTs, requiring more equipment and processing abilities.

Thermal imaging of a crop canopy from above requires a sufficient distance above the crop to capture a sufficiently wide area in a field of view. A truck crane for vineyards (Möller et al., 2007) and an unmanned aerial vehicle (UAV) in a pistachio orchard (Gonzalez-Dugo et al., 2015) have been used to fulfill this height requirement. Although thermal imaging has been used on agronomic crops in a greenhouse (Mangus et al., 2015), previous field-based approaches have been focused on tree and vine crops. Their discontinuous canopies and large physical size make it possible to use systems that capture a larger field of view with a lower resolution, such as 12 cm (Gonzalez-Dugo et al., 2012). The high cost of these systems, along with the high resolution required due to

the physical characteristics of the crop canopy has limited the use of this approach in grain crops.

Machine vision has been utilized in precision agriculture and elsewhere to discriminate areas within an image based upon vegetative properties. Algorithms that can automatically accomplish this can be used for mechanical or chemical site-specific treatments (Guijarro et al., 2011). The first stage in a two-step process is applying pre-processing procedures such as color correction and contrast enhancement. In the second stage, a binary image is formed by classifying each pixel as background or as a plant (Meyer and Neto, 2008). Otsu (1979) developed a method that converts pixels from a grayscale image to binary values based on intra-image intensity. Segmentation of the image was accomplished by deriving a threshold by treating the image histogram as bimodal, separating foreground and background by reducing in-class variance. Although this method is widely used, it suffers from incorrect identification of pixels and slow processing when compared with using the mean intensity within an image for object discrimination. (Hamuda et al., 2016; Guijarro et al., 2011)

There have been limitations to using thermographic and thermometric approaches to mapping within-field variability. Infrared thermometers can be mounted on in-field equipment but single point sensors do not provide the resolution of thermal cameras. Using an IRT to measure temperature of a complete canopy would eliminate bias from soil, but temperatures of shaded areas of a crop can vary significantly from sunlit portions (Han et al., 2016). A system designed using miniature long wave infrared (LWIR) and visible light cameras would be an economical approach to deploying an array of sensors similar to how IRTs have been utilized. The individual resolution of each sensor might

not be as high as a standard LWIR camera, but its portability and its relatively high speed sampling capabilities would allow for a temporally and spatially high resolution mapping of plant water stress throughout a field.

Objectives

The overall objective of this research was to create a system using multiple cameras that was capable of measuring the temperature of a plant canopy by discriminating a crop within a field of view. The specific objectives were:

- Develop an electronic system capable of capturing multispectral images from board level LWIR and visible cameras with high temporal resolution, either from a static location within a field or mounted on a mobile platform with high spatial resolution, for the purpose of measuring crop canopy temperature.
- Design and perform a radiometric calibration procedure to produce a model relating raw camera output to temperature.
- Create post-processing procedures that combine a region of interest defined by the RGB image with radiometric interpretations of LWIR images to produce a meaningful temperature measurement of a crop within a field of view.

MATERIALS AND METHODS

Instrument Design

An electronic system incorporating a number of components needed to be designed and built to achieve the objectives of this research. The design of the Multispectral System for Imaging of a Crop Canopy (MSICC) required that it meet the following specifications:

- Image capture and storage from LWIR and RGB cameras must be automated at specified time-intervals
- LWIR camera image must be output to an external screen to easily identify the current field of view
- Platform must be expandable to allow attachment of external analog or digital components (e.g. RS-232, thermometers)
- Instrument and associated peripherals must be capable of unsupervised data logging in the laboratory and in the field

The basic design of this system centered around selecting camera components and a processor that controlled operations. Board level cameras, whether visible or LWIR, are produced to be used in embedded systems and are often used in mobile devices. Accessible low-level functions of these imagers allowed their integration into a customized system. An open source microprocessor platform was chosen to provide access to existing device drivers of necessary components. The Teensy USB Development Board v3.2 (PJRC.COM LLC, Sherwood, OR), powered by an 72MHz ARM Cortex M4 processor, was utilized as the central processing unit (CPU) because of its compatibility with the Arduino (Arduino LLC, Turin, Italy) environment's C++ libraries. The board coupled the microprocessor with a boot-loader that allowed firmware programming over a USB port. The use of a microprocessor as CPU allowed real-time control of camera functions such as interrupt processes that captured images based on a timer. Such strict timing of operation was necessary to meet the requirements for this design, specifically retrieving coincident frames from both cameras to be displayed or stored, and communicating with other processor based systems.

The most important feature of the MSICC design was the miniature infrared camera component. In addition to its size, the Lepton LWIR camera (FLIR Systems, Wilsonville, OR) was chosen because its availability and cost (approximately \$175) allowed for integration into a specialized low-cost design. The Lepton's array of 80x60 pixels was sensitive to 8-14 μ m wavelengths and packaged with a 51° horizontal field of view lens. Used at 1m distance from its target this gave a resolution of 1.2cm/pixel. On-board signal processing integrated data from its sensor and output a 16-bit value for each pixel that corresponded to radiant flux. These values could be normalized to form a grayscale image or a color map could be applied to form a false color image. The Command and Control Interface (CCI) of the Lepton, accessed by the CPU through an Inter-Integrated Circuit (I2C) bus, provided read and write commands such as triggering the shutter, changing various camera modes, and obtaining shutter and sensor temperatures. Video output from the LWIR camera transmitted frames to the CPU over a Serial Peripheral Interface (SPI) channel.

The visible camera used in this design was chosen because its form factor was similar to that of the LWIR camera and because of the availability of software usable with the microprocessor. The ArduCAM Mini (arducam.com) was a packaged daughterboard with a 2 megapixel OV2640 sensor (OmniVision Technologies, Santa Clara, CA), onboard image buffer, and a standard S-mount interchangeable lens. Firmware to run this camera was implemented using code from the manufacturer modified to work with the chosen processor. Camera operations of the ArduCAM were controlled by an onboard chip, while the CPU was needed to transfer the images to a storage medium. A 3.6mm lens was used on this camera corresponding to a 52° field of

view on its 3.6x2.7 mm sensor. Similar to the Lepton, commands to the ArduCAM were sent over the I2C bus, while frames were transferred over SPI.

A printed circuit board (PCB) designed around components interfacing to the microprocessor functioned as a development board to test firmware, make lab-based measurements for calibration, and as a prototype to be field deployable either independently or as part of another data-logging system. The overall cost of the PCB, components, cameras, and microprocessor development board was about US\$400.

The PCB incorporated the electronics needed to interface the microprocessor with cameras, storage, and display components into a single package. The modular form of the development board allowed its 2.5 mm headers to be easily plugged into the developed PCB. The chip select (CS) lines of the SPI were multiplexed (MUX) and the clock and data lines were buffered out of the microprocessor. A microSD socket for external storage and an LCD display, both accessed over SPI, were added for storage and display of images, respectively. An RS-232 conversion chip was added to the processor's serial communication as an interface to communicate with off-board devices such as a data logger. Other chips included on the board but ultimately not implemented, such as high speed differential serial (RS-422) and serial RAM were SPI-based. The development board's input pins not discretely implemented were broken out on the MSICC and were used as additional analog and digital signal inputs.

Power on the board was regulated from a 12V source to provide 5V, 3.3V, and 2.8V. Voltage translators shifted 3.3V I2C clock and data lines and the four SPI signals from the microprocessor to component specific levels, either to 2.8V for the camera or 5V for the LCD screen.

The schematic for the board is in Appendix 1 and the block diagram for the design is shown in figure 3.1. The PCB with the cameras mounted is shown in figure 3.2.

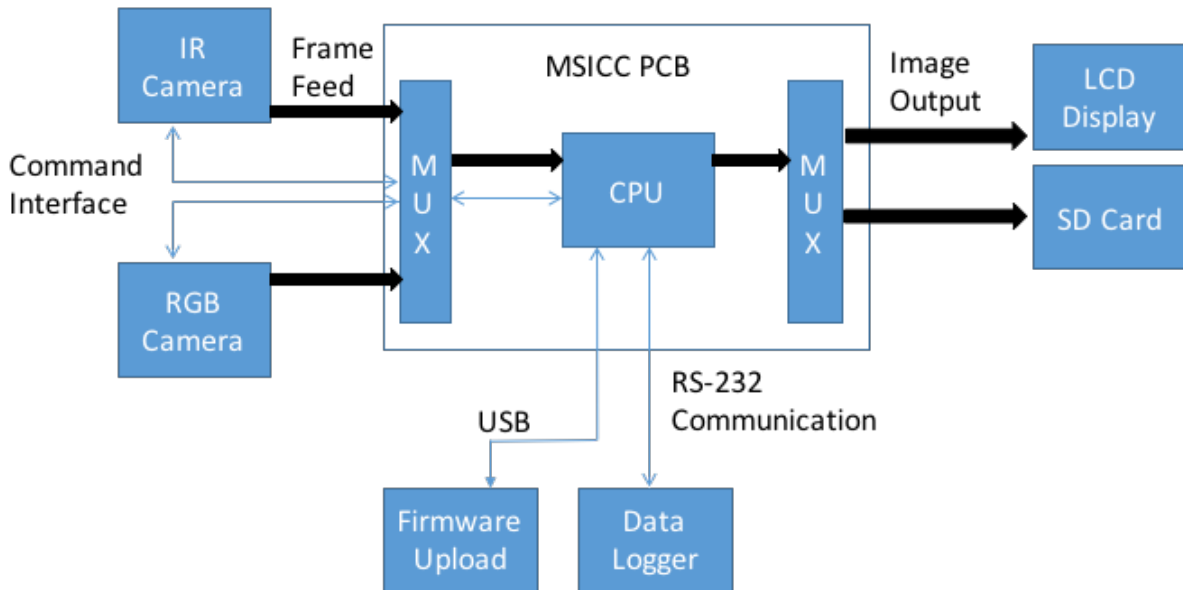


Figure 3.1. Block diagram of the components and PCB interfaces of the MSICC.

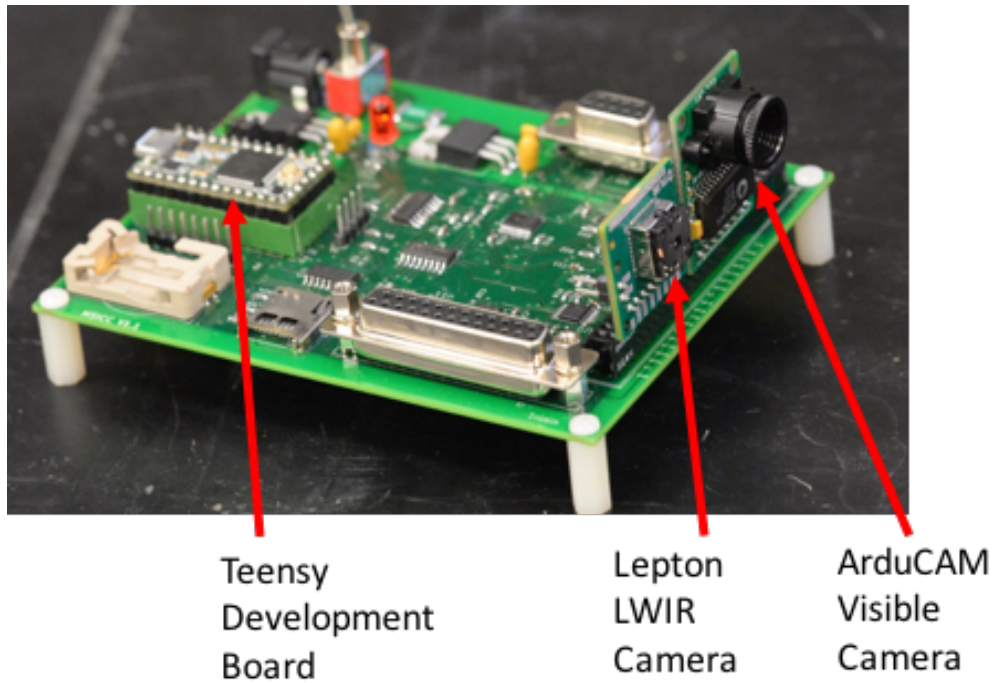


Figure 3.2. The populated PCB used in the MSICC system with red arrows denoting the Teensy development board, the Lepton LWIR camera, and the ArduCAM visible camera.

The firmware for the MSICC was written with a focus on data-logging type functions. Code written for field deployment obtained adjustable settings (such as system warmup time, lapse time between frames, and number of images to capture in a burst) from text files that could be edited and placed on the microSD card so that adjustments did not require reprogramming. The drivers for the instrument came from either specialized code developed for this research or modified open source drivers. Appendix 2 details where the code originated and/or what changes were made to accommodate it into the system. Prototypes of this instrument were customized for evaluation and experimentation as well as for dedicated data logging. The flexibility of the design allowed the system to be used as a slave responding to serial commands, or as a master that recorded data and controlled external devices on its own timing as was the case when used in laboratory calibration experiments.

Calibration

To calibrate LWIR camera output to a thermal response, relationship between scene temperature and three independent variables -- raw pixel output value, LWIR sensor temperature, and camera temperature -- was postulated. Bower et al. (2009) showed that water can be used as an economical temperature-controlled target (relative to a commercial blackbody) for calibrating a thermal camera. Water has an emissivity similar to that of a healthy plant, $\epsilon \approx 0.98$, reflecting small amounts of energy in the 8-14 μm range where the LWIR camera is sensitive. The temperature of water can be easily regulated to simulate field conditions in the range of 20-40°C. Coupling this water bath with an independent control of the thermal camera temperature created an experimental

setup that provided the ability to calibrate the output of the thermal camera as a radiometric device.

The circulating two-bath system that was used in the calibration was modeled after the test setup in Bower et al. (2009). Expanding on their test fixture, the source and water baths were covered to reduce the influence of outside radiation on measurements. The test fixture (fig. 3.3) used an ice chest with its lid removed coupled with an immersion heater as an alternative to the recirculating water bath. A piece of foam insulation enclosed the chamber and supported the instrument cluster. The chamber was then filled with 35 L of chilled water which was heated gradually with the immersion heater regulated by a rheostat. To create the target bath that acted as the blackbody approximation, a 7.6 L bucket was placed inside the chamber with risers that elevated the top of it above the surface of the source bath. A submersible pump with a flow rate of 2.7 L/min was placed inside the source bath with its output plumbed through a spigot in the base of the bucket. The pump was in constant operation, forcing water from the bottom of the bucket upward, overflowing, and flowing back into the source bath. This apparatus ensured constant circulation between the source and target water baths working to create a uniform temperature throughout the system.

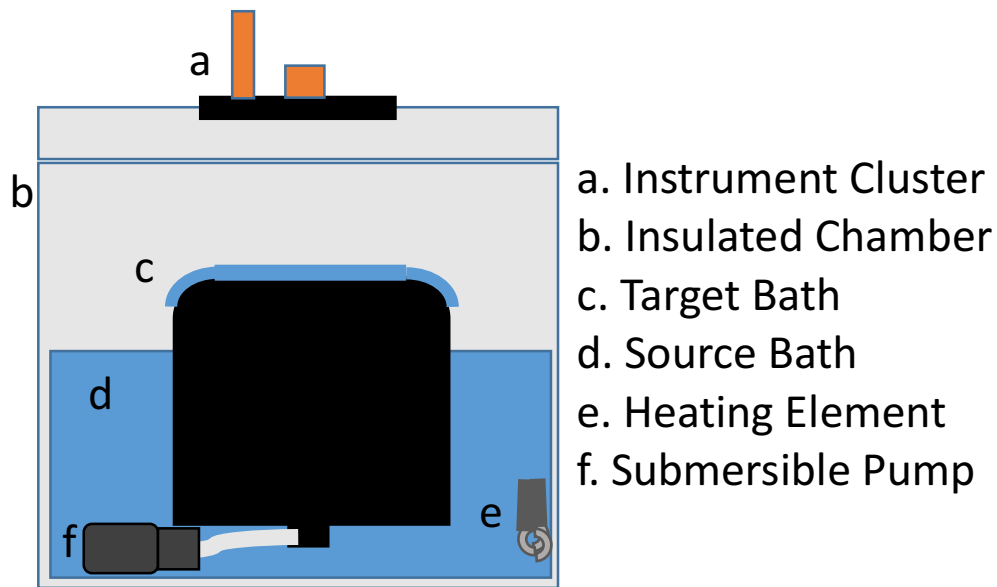


Figure 3.3. A side view diagram of the calibration test setup used to create a blackbody approximation for LWIR calibration.

The top of the chamber was made out of foam insulation with a 13 cm circular hole used as a window for the infrared imager. A sheet of acetyl resin, chosen for its low thermal conductivity, was placed over this window to minimize ambient environmental effects on the chamber. Small holes were drilled into the resin plate acting as windows for the LWIR camera and an IRT to view the inside of the chamber. The LWIR camera was housed inside a small copper shroud attached to a thermoelectric module (TEM). This housing allowed the temperature of the camera to be increased or decreased separately from environmental conditions. The TEM was driven by a control circuit operated by a pulse width modulation (PWM) signal from the MSICC and an external switching circuit (schematic shown in Appendix 1). The PWM varied the output of the TEM based upon the experiment set point and the camera's self-reported shutter temperature. The addition of an Apogee SI-411 IRT (Apogee Instruments, Logan, UT), placed directly adjacent to the infrared imager, allowed relating the target temperature to the IRT temperature. The temperature of the water, or imaging target, was measured 5 cm

below the surface. Submerging a thermometer instead of suspending it on the surface allowed recording the temperature of the target bath without creating bias at the air/water interface. All of these instruments were connected to the MSICC, which controlled and recorded measurements during the experimental runs.

During each experimental run, chilled water was slowly heated over 4-6 hours depending on the initial and final temperature of the water. Immediately before each image was captured, a non-uniformity correction (NUC) was made. A correction was necessary because each of the pixels on the focal plane array (FPA) has unique operating characteristics. The NUC compensates for these differences by imaging a uniform surface (the shutter) and converting the output of each pixel using a standard compensation curve (Budzier and Gerlach, 2015). A frame was captured every 60 seconds, and the temperature of the shutter and sensor at this time were recorded. Average temporal resolution of each experiment yielded one measurement per 0.13° C change in bath temperature. A scatter plot of the sampled conditions is shown in figure 3.4. Each image was matched with an IRT measurement taken at the same time and water temperature measurements taken just below the surface of the flowing water. Data recording for this experiment was automated using the MSICC to log images and measurements.

Two sets of experiments were conducted using similar methods, but relying on different measurements in the target bath. The initial calibration experiment was conducted with the thermal imager and an IRT aimed at the water surface, along with a K-type thermocouple (TC) 5 cm below the surface. During these experiments, the temperature of the camera was held at 30° C. Initially, only a TC was used to record water temperature, but then it was determined that the K-type TC was not accurate

enough to be used as a reference for this test. To increase the accuracy of the measurement of the target temperature, a thermistor was used alongside the thermocouple. The following experiments were run with both the thermistor and TC:

- The camera temperature was floating, or not controlled (i.e., the chamber temperature would raise or lower the camera temperature similar to what would be expected in field conditions).
- The camera temperature was held static at a specific temperature, either 30° or 35°C.
- The camera temperature was stepped to set points between 20° and 45°C at 5° increments while the water heater was shut off. This test was performed at various water temperatures.

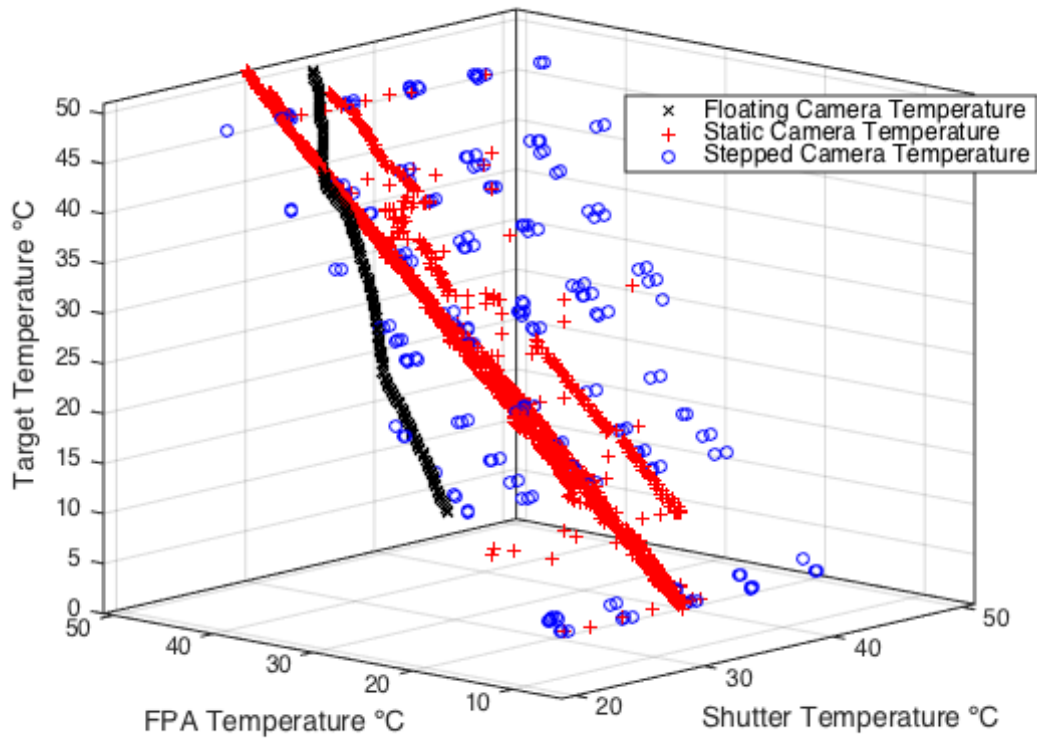


Figure 3.4. Test conditions for LWIR camera calibration experiments with data points separated by camera temperature control type.

Field Trials

Initial field tests were multiple-day time series taken at fixed locations. During these experiments, the MSICC was paired with a CR216 data-logger (Campbell Scientific, Logan, UT) and an IRT enclosed in an environmentally sealed package. The CR216 data-logger communicated with the IRT over its SDI-12 interface, acted as a time server, and controlled power to the board to conserve battery power. The CR216 was used only in this initial deployment, with its functions being later incorporated into the MSICC's firmware. Data were taken in the field in three different plots from late September through November 2016 at the University of Missouri's South Farm Research

Center. The system was suspended from an articulating arm 0.9 m above the crop canopy, yielding a field of view with 69x90 cm coverage. The IRT had a 44° viewing angle with a circular field of view and was mounted 5 cm away from the LWIR camera. The mechanical offset and the differing geometries encompassed by the two systems led to IRT measurements being more representational of the right side of the image. Shown in figure 3.5 is the overlapping field of view of the two instruments.

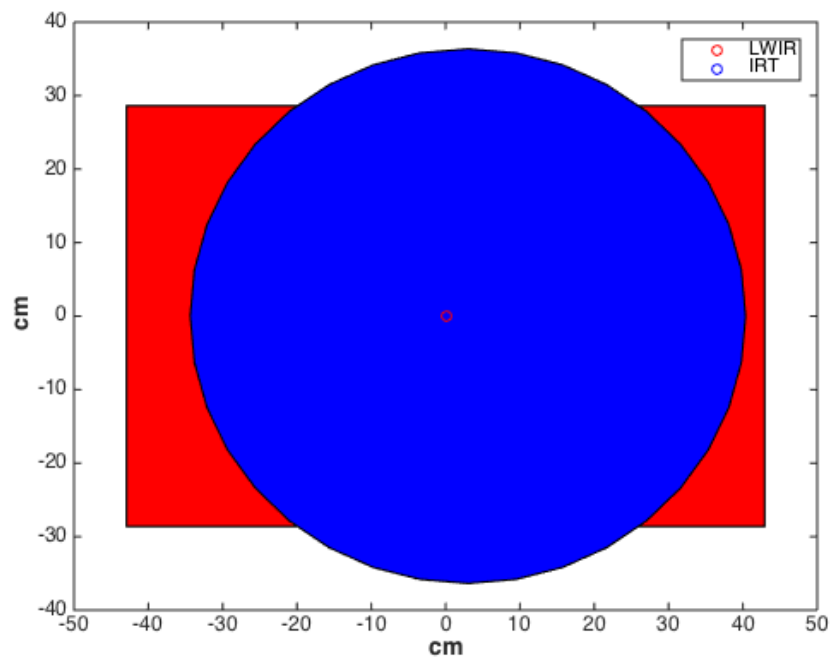


Figure 3.5. Field of views for IRT and LWIR lenses.

The first two sensing locations were in late-season soybean plots, one with a full canopy and the other with soil visible from the nadir. Temperature measurements from the MSICC and the SI-411 IRT were taken simultaneously with an overlapping field of view. Once these plants approached senescence, the system was then moved to a third plot of soybean plants planted in early September. An unusually warm fall allowed imaging of the plants as they matured. Different areas with varying amounts of soil

visible within the 8.5 x 3.7 m plot were imaged during this period. The instrument deployed in the field is shown in figure 3.6.



Figure 3.6. Multispectral system deployed on an arm in a soybean field.

RESULTS AND DISCUSSION

Calibration

The goal of the calibration exercise was to create an equation that could convert the response of each pixel into a temperature. The median raw pixel value of each image was extracted and used to represent the LWIR camera output at the given camera shutter temperature, camera sensor temperature, and surface temperature of the water. Only those calibration data that included thermistor measurements were used to create a model relating pixel values to temperature. A random block of 20% of the data from these measurements was set aside to be used for validation. Using the rest of the data, linear and quadratic regressions estimating scene temperature as a function of the independent variables were developed.

Tests where target temperature was measured only by TC were used as a secondary validation source for the best linear and quadratic models. To utilize data from tests that included only a TC, a linear model was created from all data points that included both thermistor and TC measurements to correct TC measurements to a thermistor reference. The same was done for the IRT measurements, but only for observations where the target temperature was under 30 °C. IRT measurements from higher temperatures in this experiment were not reliable because of errors resulting from condensation accruing on the lens.

Equations 3.1 and 3.2 describe linear and quadratic relationships, respectively, between the median of the camera raw pixel output and the temperature of that pixel. Statistics outlining the performance of the models are shown in Table 3.1. The quadratic model (equation 3.2) had an RMSE of 0.65°C when applied to the validation set, or 0.25°C better than the linear model in equation 3.1. Considering this, along with the lower RMSE of the calibration data, it can be said that the quadratic model was better than the linear model.

$$T_{pixel} = A * 0.064 + B * 4.314 - C * 4.1394 - 480.5 \quad (3.1)$$

$$T_{pixel} = A * 0.229 + B * 95.764 - C * 111.85 \quad (3.2)$$

$$-A * B * 0.009 + A * C * 0.011$$

$$-B * C * 2.611 - A^2 * (1.575 \times 10^{-5})$$

$$+ B^2 * 1.1355 + C^2 * 1.486 - 727.5$$

where:

T_{pixel} = temperature of pixel (°C)

A = raw counts of pixel

B = camera shutter temperature (°C)

C = temperature of the camera sensor (°C)

Table 3.1. RMSE and R² for linear and quadratic equations developed from the calibration set and for the calibration equations applied to the randomly selected validation set.

Model Type	Calibration		Validation	
	R ²	RMSE (°C)	R ²	RMSE (°C)
Linear	0.994	0.95	0.995	0.90
Quadratic	0.997	0.68	0.997	0.65

In the linear regression model (equation 3.1) all three independent variables were highly significant ($\alpha=0.0001$). Plotted in figure 3.7a are the observed and predicted values for the randomly chosen validation set. The residuals were mostly between -2 and 0 °C (fig 3.7b), but the scatter plot had a definite concave upward shape to it. Because of the apparent curve within the residual plot, a more complex model including quadratic and interaction terms was investigated.

The quadratic model (equation 3.2) included squared and interaction terms for each variable. All terms were highly significant ($\alpha=0.0001$). Figure 3.8a displays the observed versus predicted values for the validation set while figure 3.8b contains the residuals. The residual plot shows the majority of the points falling in the range of -1 to 1 °C. The random structure of the residuals reinforces the appropriateness of the quadratic regression with interactions.

Equations 3.3 and 3.4 relate the measured values from the TC and IRT, respectively, to the thermistor reference used in the camera radiometric models. Thermocouple measurements over the entire temperature range were transformed to the thermistor reference using the best-fit linear model:

$$TC_{\text{corr}} = TC_m * 1.114 - 3.388 \quad (3.3)$$

where:

TC_{corr} = corrected thermocouple temperature ($^{\circ}\text{C}$)

TC_{m} = measured thermocouple temperature ($^{\circ}\text{C}$)

IRT measurements under 30°C were transformed to the same reference with:

$$IRT_{\text{corr}} = IRT_{\text{m}} * 1.083 - 2.498 \quad (3.4)$$

where:

IRT_{corr} = corrected thermocouple temperature ($^{\circ}\text{C}$)

IRT_{m} = measured thermocouple temperature ($^{\circ}\text{C}$)

Figure 3.9a shows the thermocouple measurements with a strong correlation to the line of best fit. The regression relating TC temperature to thermistor temperature had an R^2 of 0.997 and an RMSE of 0.438°C . In figure 3.9b the measurement errors of the IRT are visible, but the line of best fit shows strong correlation. The regression to project IRT temperature to a thermistor reference temperature had an R^2 of 0.991 and an RMSE of 0.732°C . This plot also shows the effects of condensation on IRT temperature measurements above 30°C .

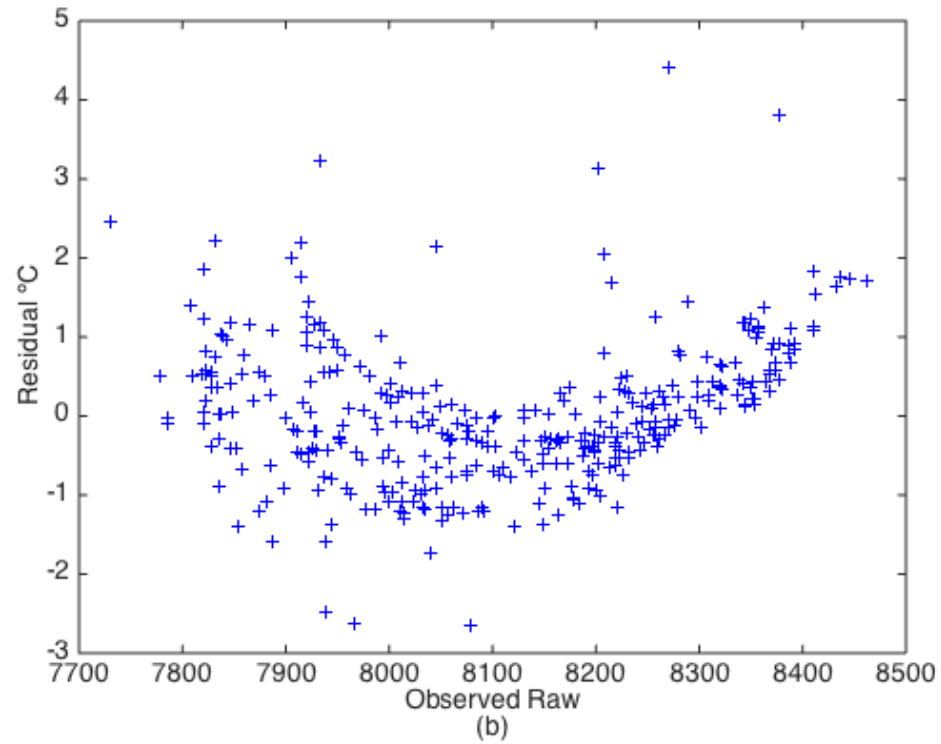
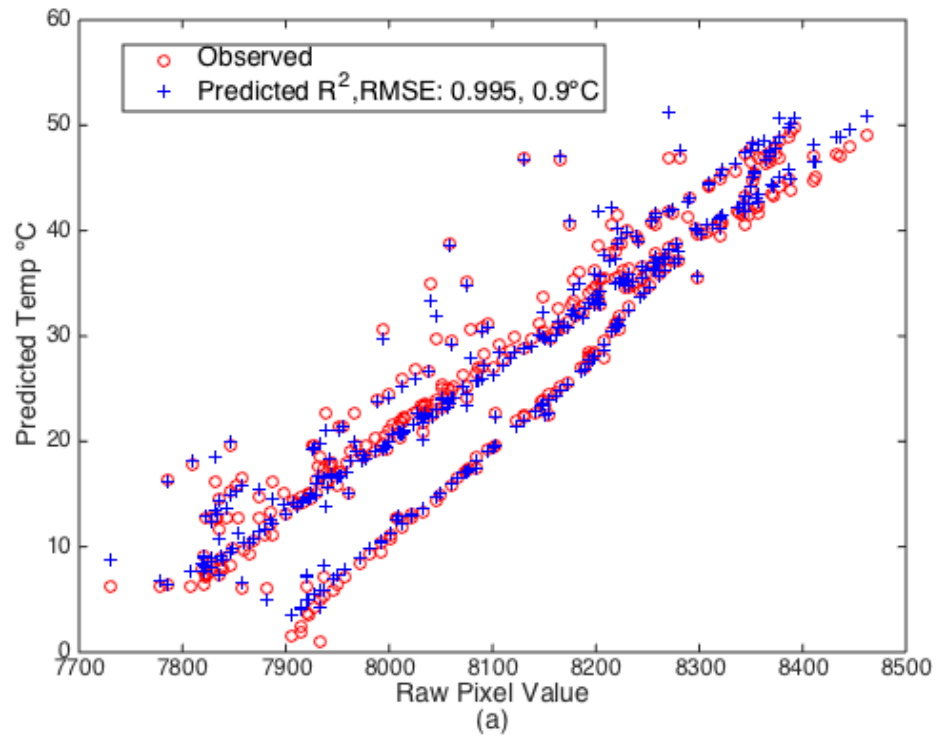


Figure 3.7. a) Plot of the observed values from the validation set and the predicted values from the linear regression model, equation 3.1, estimating target temperature from camera body and sensor temperature, and camera raw output. b) Plot of the validation residuals from the linear regression.

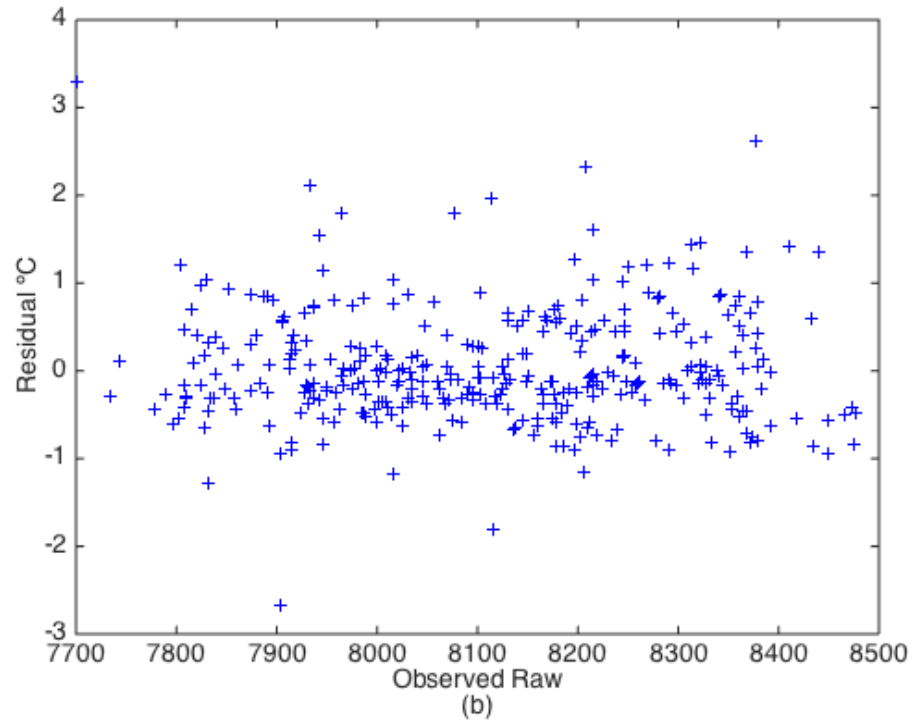
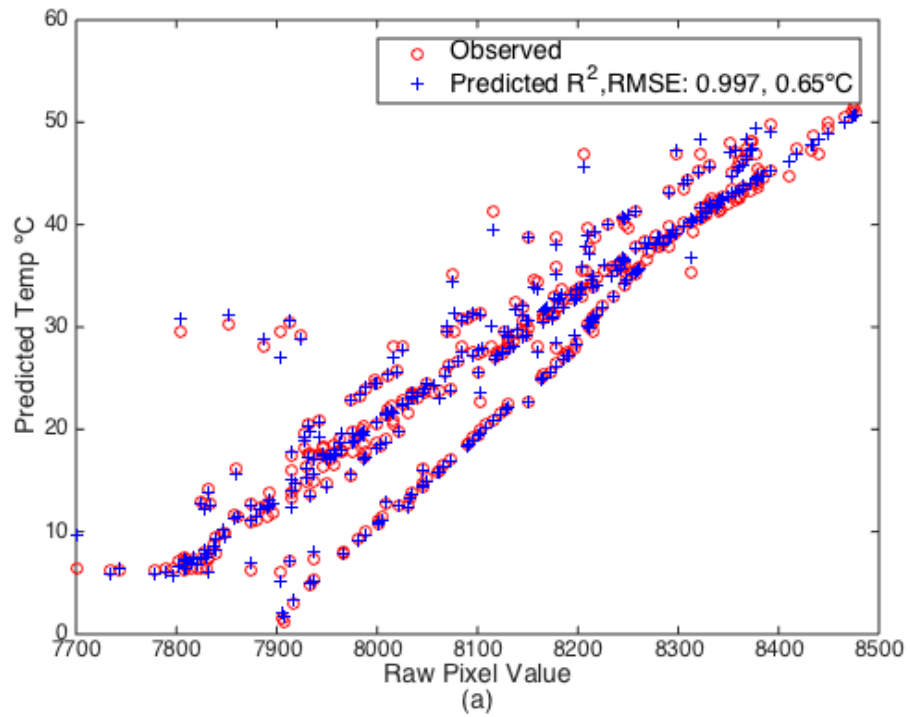


Figure 3.8. a) Plot of the observed values from the validation set and the predicted values from the quadratic regression model, equation 3.2, relating camera body and sensor temperature, target temperature, and camera raw output. b) Plot of the validation residuals from the quadratic regression model.

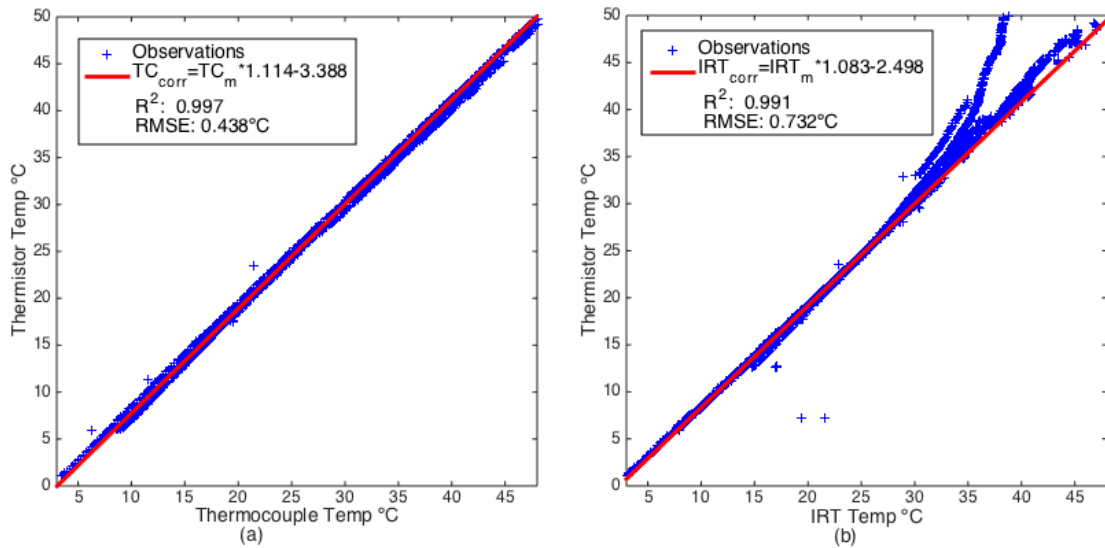


Figure 3.9. Plot of measured thermocouple (a) and IRT (b) values with predictive models, equations 3.3 and 3.4 respectively.

Figure 3.10a shows application of the linear model, equation 3.1, to the secondary validation set after adjusting the TC data with equation 3.3. Figure 3.10b shows application of the quadratic model, equation 3.2, to the secondary validation set after adjusting the TC data with equation 3.3. When using the models to predict temperature from the TC only test set, both linear and quadratic models exhibit essentially the same R^2 , 0.997. As with the other validation set, the quadratic model has a lower RMSE, 1.225°C , than the linear model, 1.391°C . The RMSE increased when compared with the primary validation set, but this can be attributed to the lower accuracy of TC measurements as well as the errors associated with equation 3.3.

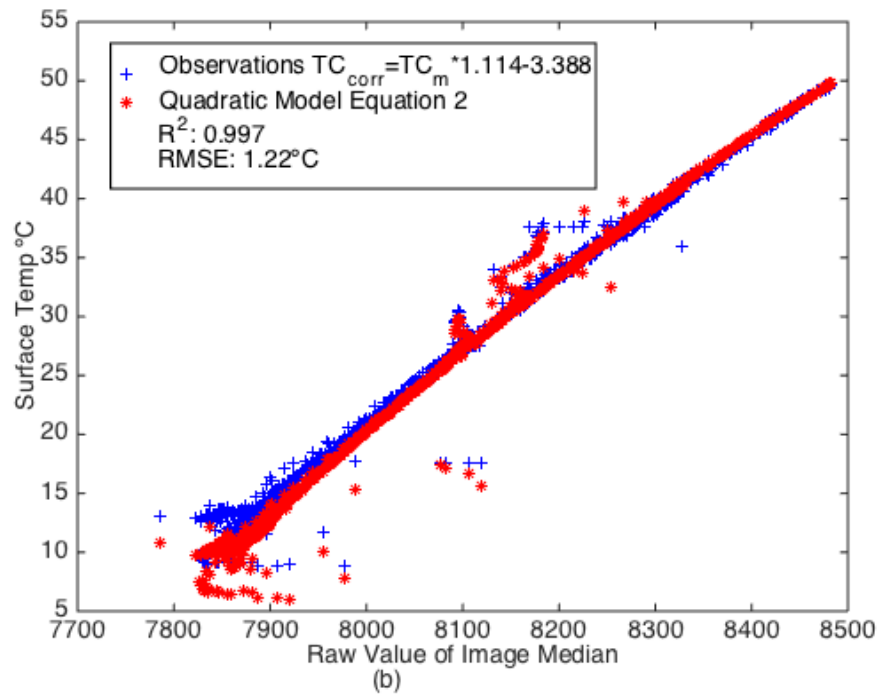
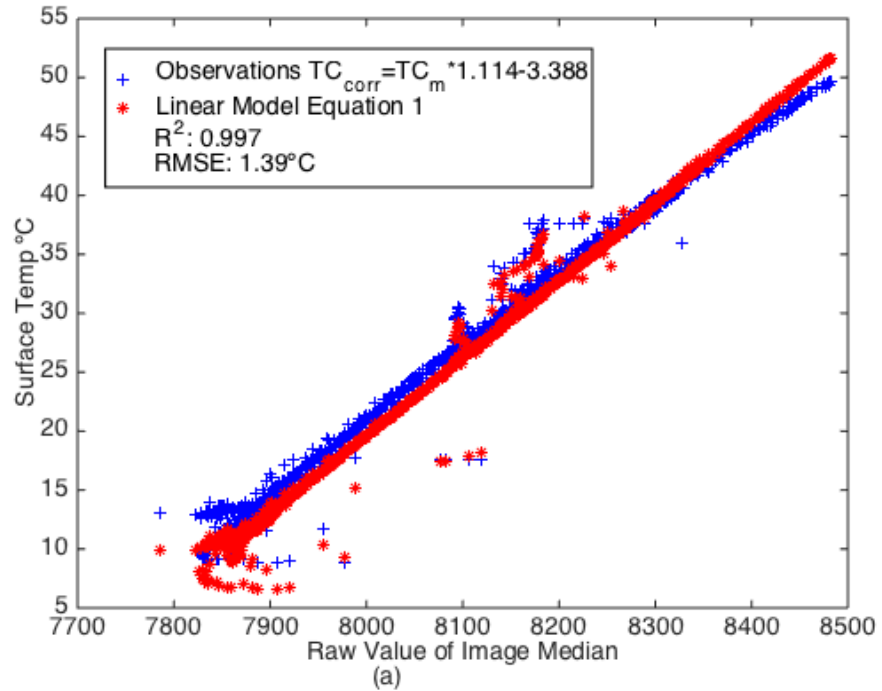


Figure 3.10. a) Plot of the observed TC temperatures, adjusted with equation 3.3, and the predicted scene temperatures from the linear regression model, equation 3.1. b) Plot of the observed TC temperatures, adjusted with equation 3.3, and the predicted scene temperatures from the quadratic regression model, equation 3.2.

Field Operation

The effectiveness of the LWIR camera calibration was evaluated by applying the derived models to data recorded in the 2016 field experiments. Time series from three days data collection on three different plots were chosen to represent different crop canopy topographies due to plant spacing and crop maturity: mature plants with some shaded soil, day 263, mature plants with full canopy, day 268, and recently emerged seedlings, day 273. A visible image from midday for each of these days is shown in figures 3.11a-3.13a.

A time series of images taken on an approximate five-minute interval throughout each day of field data collection enabled a visual comparison of instrument performance to an IRT. The median and standard deviation for each image is plotted in figures 3.11b-3.13b. Gaps in data occurred when the images captured were corrupted or the MSICC malfunctioned. The IRT and MSICC image temperatures follow the same warming and cooling trends throughout the day. Air temperature recorded less than 1 km away at the South Farm weather station operated by University of Missouri Extension is plotted as a reference.

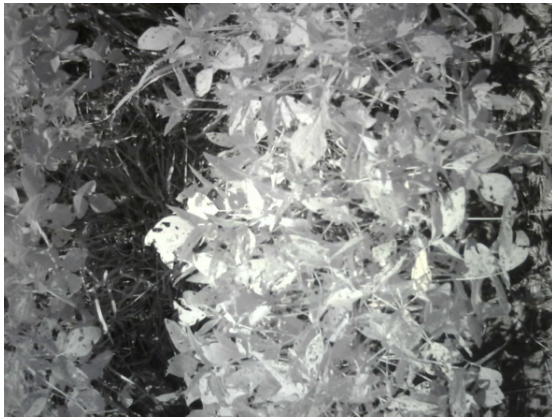
Histograms of each sample image throughout this time period displays the variation of temperatures within the field of view, providing evidence that the increased resolution compared to an IRT is beneficial. The histogram changes throughout a diurnal cycle, and this is visualized efficiently through a time series plot of histograms. These 3-D plots are shown in figures 3.11c-3.13c. The spread of the histogram early or late in the day is generally tighter than it is during the middle of the day. This was expected because

as the day warms up, the temperature of shaded scene elements does not increase as much as that of the exposed plant area.

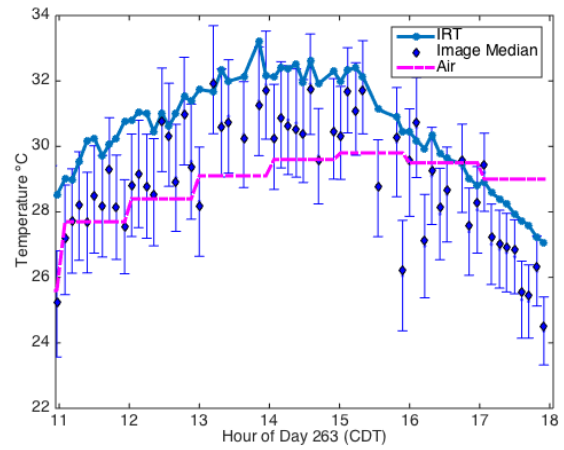
The temperature range of the open canopy scene (fig. 3.11) is visible in the spread of the time series histogram. The standard deviation of this scene ranged from 1.04 to 2.13 °C, which explains the difference between the camera and IRT measurements.

The full canopy scene (fig. 3.12) has a smaller standard deviation throughout the day, ranging from 0.56 to 1.41 °C. The histogram counts remain similar over the measurement period, regardless of the time of day. The lower difference is reflected by the IRT measurements being similar to the camera values.

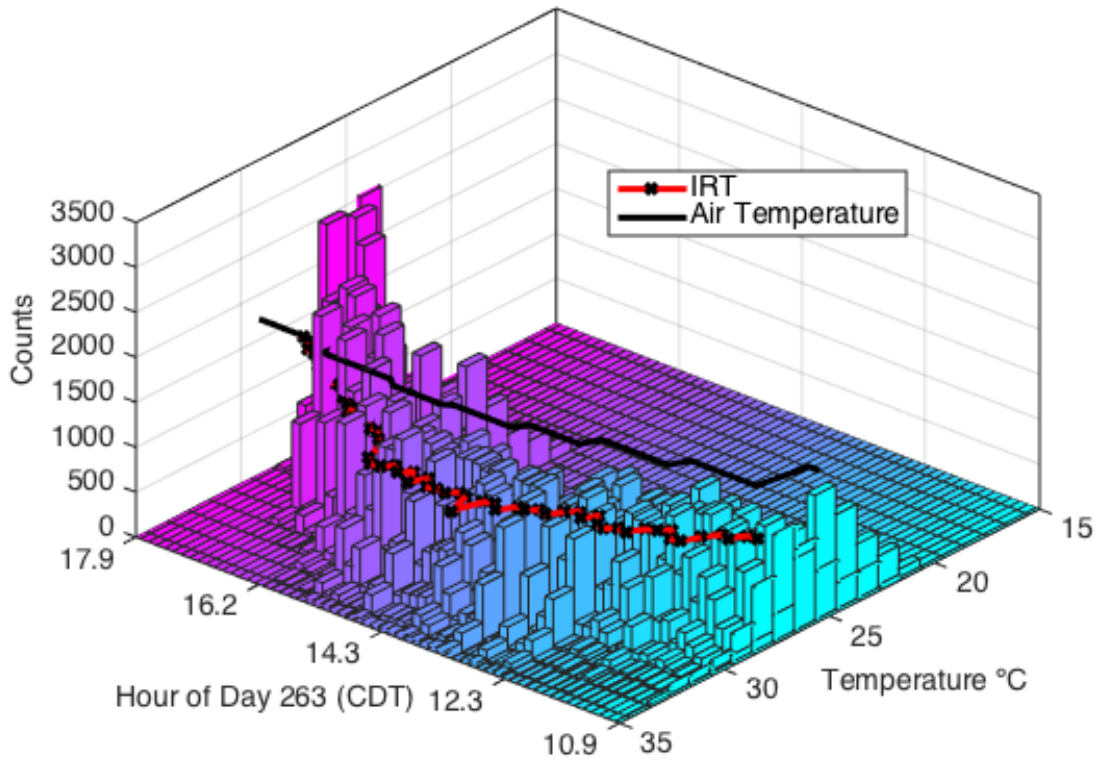
The visible image of day 273 (fig. 3.13a) shows curled leaves, indicating that the young plants were under stress. The left side of the image contains mostly plants and shaded soil, and the right side of the image has mostly sunlit soil. The IRT, whose field of view is biased to the right side of the image (fig. 3.5), measured a higher temperature than the mean from the camera. This discrepancy in temperature measurements from the two instruments can be attributed to the exposed, dry soil being at a much higher temperature than the plants. The spread of the error bars (fig. 3.13b) and the distribution of the histogram (fig. 3.13c) increase in the middle of the day, when solar radiation is greatest. This indicates that solar radiation greatly affects exposed soil temperature and can bias measurements from a single point sensor.



(a)



(b)

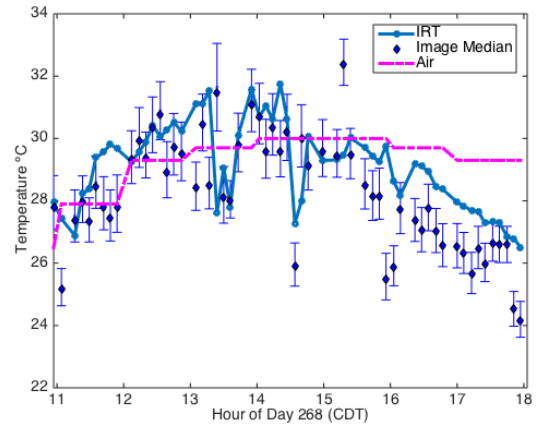


(c)

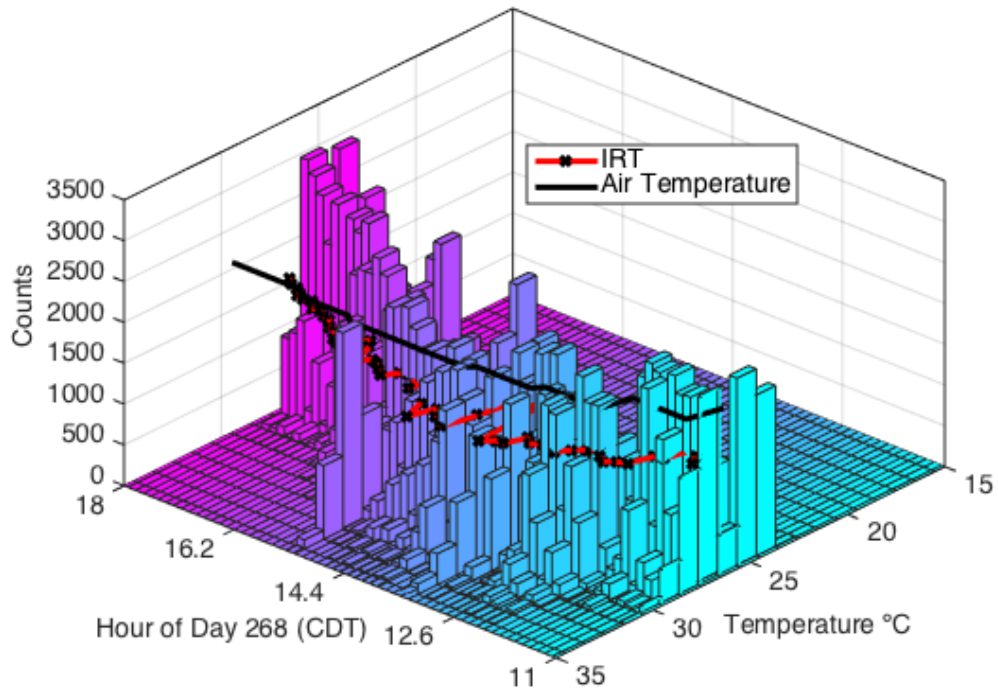
Figure 3.11. a) LWIR image of mature soybean plant canopy with soil visible from day 263 of 2016 at 1246 CDT. b) Daytime measurements from day 263, with median and standard deviation of each image plotted along with IRT temperature and hourly air temperature. c) Time-series of histograms of each image plotted with IRT temperature and hourly air temperature.



(a)

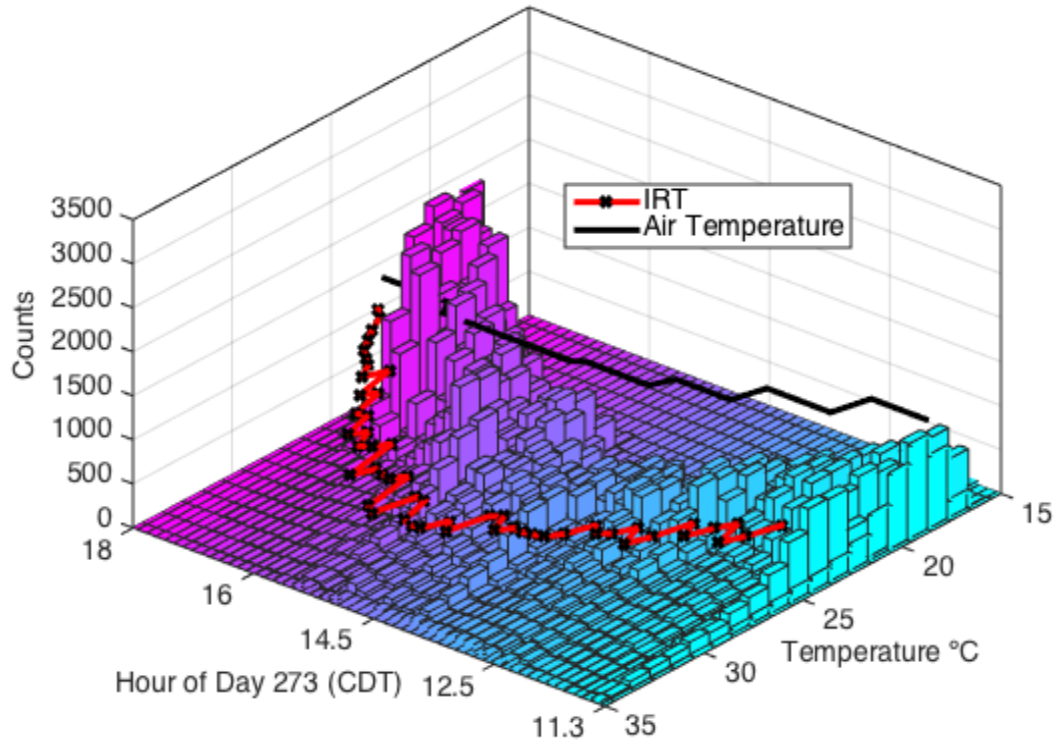
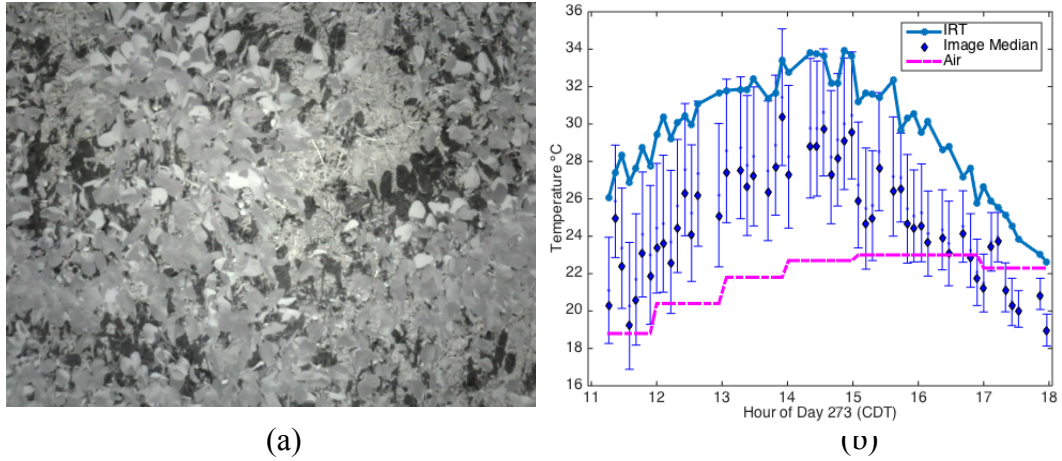


(b)



(c)

Figure 3.12. a) LWIR image of mature soybean plants with complete canopy and no soil visible from day 268 of 2016 at 1245 CDT b): Daytime measurements from day 268, with median and standard deviation of each image plotted along with IRT temperature and hourly air temperature. c) Time-series of histograms of each image plotted with IRT temperature and hourly air temperature.



(a)

(b)

(c)

Figure 3.13. a) LWIR image of young soybean plants from day 273 of 2016 at 1244 CDT. b) Daytime measurements from day 273, with median and standard deviation of each image plotted along with IRT temperature and hourly air temperature. c) Time-series of histograms of each image plotted with IRT temperature and hourly air temperature.

Image Segmentation

Calibration provided a way to calculate thermal values from the LWIR camera, and field experimentation compared this method with IRT results. Discriminating plant from soil using the visible image made it possible to calculate temperature of the crop alone. As with any dual imaging system, the physical layout of the LWIR and visible cameras required overlaying the images to ensure that they encompassed the same field of view. A mask that identified whether any given pixel represented plant was created from the visible image. Then, this mask was applied to the thermal map from the LWIR camera to eliminate pixels not representing plants, making temperature calculations possible.

The optical differences in the lens pair and their rigid mounting necessitated a slight offset in the mounting position of the imagers. Other systems that vary focal length based on location, such as Möller et al. (2007), require in-field static targets to match and process images. In contrast, data can be automatically processed in this system without using such targets because the parallax correction between the two imagers is fixed. In order to match the dual images of the MSICC, a black cross on an aluminum sheet, visible in both spectra (fig. 3.14a & b), was captured simultaneously by each camera. The resolution of the RGB image was down-sampled, and the translation needed to match the field of views was determined. Linear distortion of the lens was not corrected for either camera. Raw images recorded in the field needed to be translated by five pixels in each dimension to match correctly, yielding a usable sensor area of 4125 (55 x 75) pixels. This was tested at each location by imaging a target and matching images manually (fig. 3.14).

While a wider lens for the visible camera would correct this problem, it would also add linear distortion and require an additional correction step.

After alignment, the visible image was processed to identify plants within the field of view. Plants were identified from the visible spectrum image by using Otsu's method (Otsu, 1979) accessed by the MATLAB *graythresh* command. This command output a threshold value that determined if each pixel was considered crop or non-crop. The binary matrix formed a ROI and was applied to the LWIR image to determine which pixels to use to make plant temperature measurements. The processing steps of alignment and identification of the ROI can be seen in practice in figure 3.14a-d. The shaded non-plant areas between the rows of soybean are identified in 3.14c and then applied to the LWIR image in 3.14d. Segmentation based on plant color was not used because the visible camera did not have an optical filter to keep near infrared light from reaching the sensor. A lens with an IR cutoff filter would allow the visible camera to rely on color-based algorithms at full resolution.

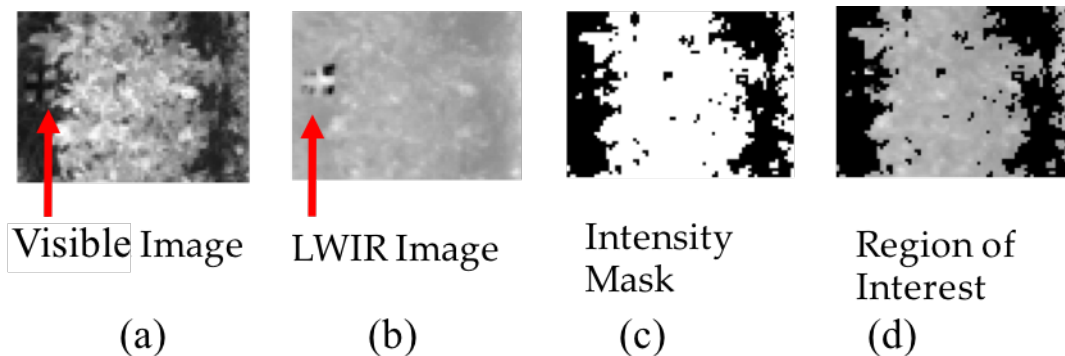


Figure 3.14. Processing steps for image segmentation. Visible (a) and LWIR (b) images were obtained. The intensity mask (c) was derived from processing the visible image. This binary mask was then applied to the LWIR image to form a region of interest (d) Red arrows note location of the alignment target described in the text.

The calibrated instrument provided a way to measure temperature from the LWIR camera output. Incorporating the calibrated LWIR output with the image segmentation algorithm completed the required image processing. In figures 3.15-3.17 the progression of this procedure is shown for the three data sets described earlier. The thermal image, figures 3.15c-3.17c, was produced by applying equation 3.2 to the LWIR image, shown in figures 3.15b-3.17b. Thermal images show the variation of canopy temperature with the sunlit tip of the plant hottest, while temperatures of shaded leaves and soil are lower. The segmented images, produced by applying the mask obtained from the visible images, are shown in figures 3.15d-3.17d.

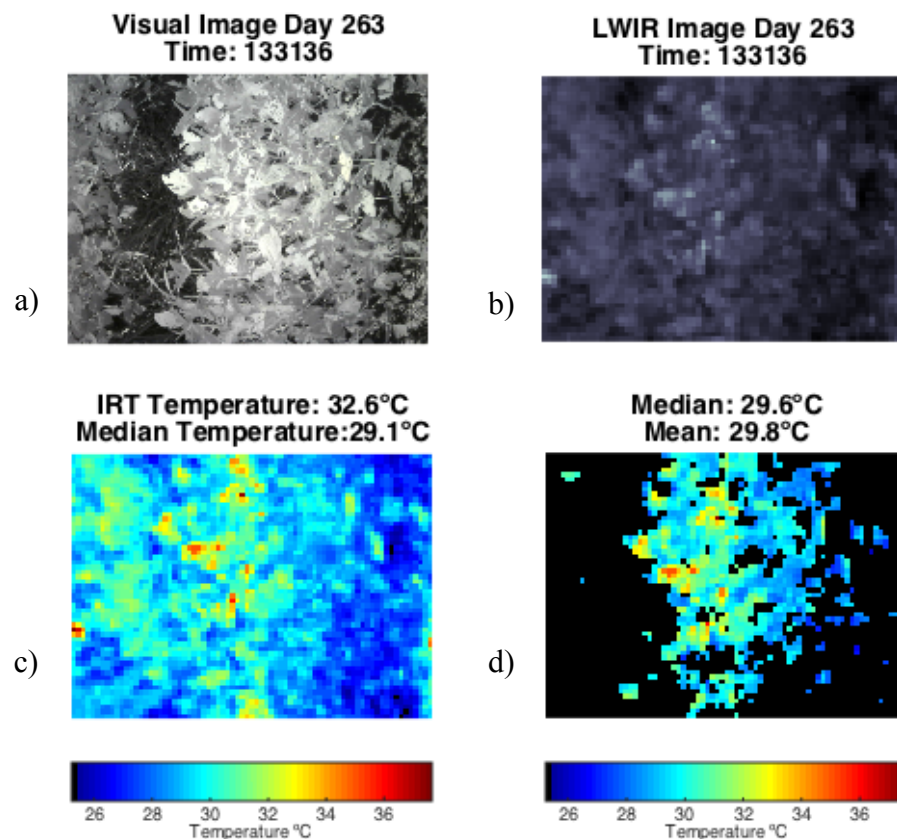


Figure 3.15. a) Visible image of open canopy, mature soybean scene representative of day 263. b) LWIR Image displaying contrast map of scene. c) Thermal image created after applying equation 3.2 to LWIR pixels. d) Segmented thermal image produced from processing visible and thermal images.

The median temperature of a segmented image should be higher in the test cases, because the cooler shaded area was removed. This is seen in the sample images where the median temperature increased from 29.1 to 29.8 °C in figure 3.15 and 26 to 26.2 °C in figure 3.16, and holds the same in figure 3.17. In figure 3.15 the temperature reported by the IRT is higher than the image average because its center point is on the hottest part of the canopy.

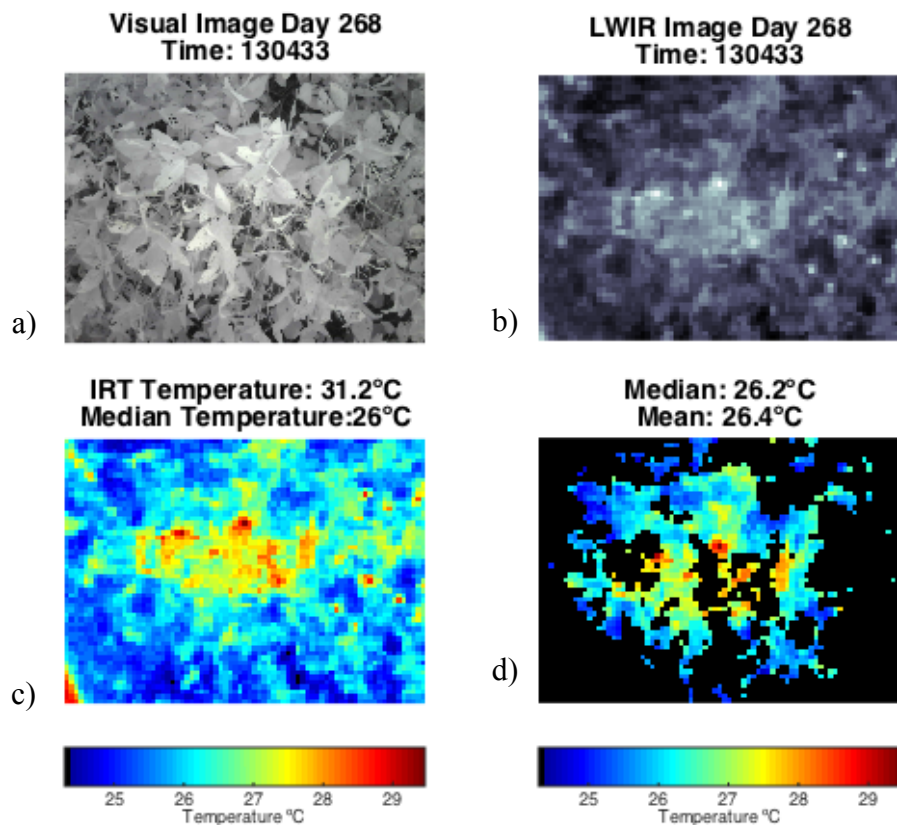


Figure 3.16. a) Visible image of complete canopy, mature soybean scene representative of day 268. b) LWIR Image displaying contrast map of scene. c) Thermal image created after applying equation 3.2 to LWIR pixels. d) Segmented thermal image produced from processing visible and thermal images.

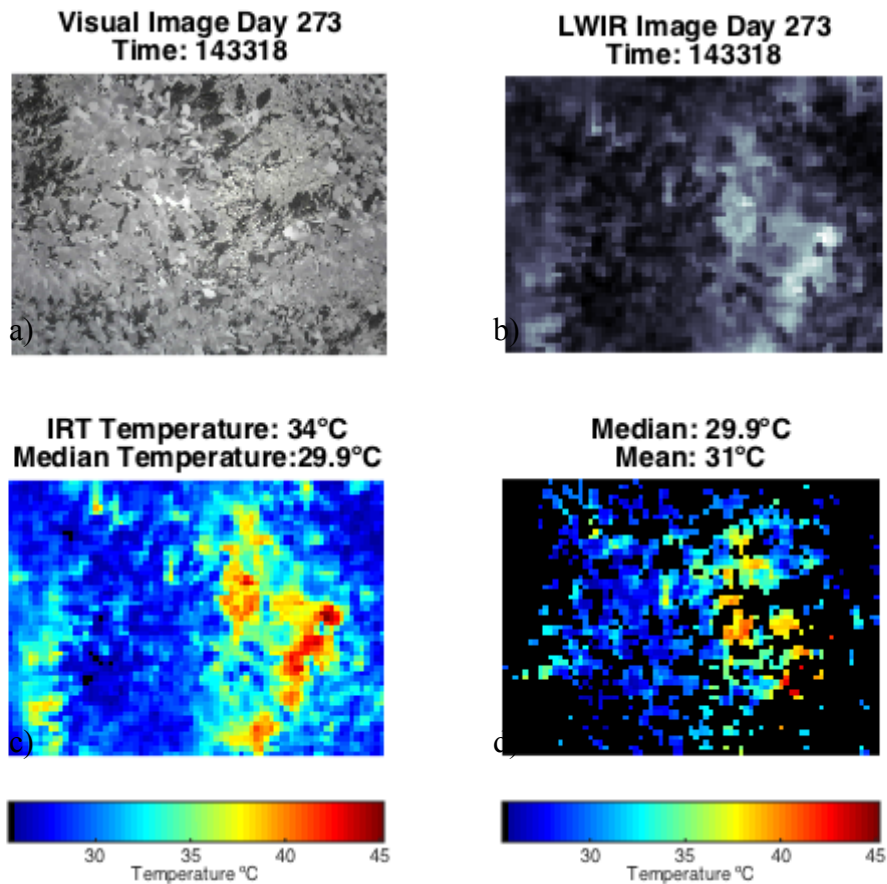


Figure 3.17. a) Visible image of young soybean scene representative of day 273. b) LWIR Image displaying contrast map of scene. c) Thermal image created after applying equation 3.2 to LWIR pixels. d) Segmented thermal image produced from processing visible and thermal images.

In figure 3.16, a full canopy scene, the algorithm worked to remove the shaded area of the intra-plant canopy. What was being removed was not soil, but cooler areas of the plant. The IRT also reports a higher temperature measurement for this scene and the median value of the image is increased after segmentation. Depending on what was included within the scene, the darker areas of the image removed through segmentation were either shaded soil or shaded leaves. For the young plants, shown in figure 3.17, the soil set the upper and lower temperature limits. This is why the median temperature of the image did not change appreciably after segmentation. The hottest pixels are in the center

and right, the area captured by the IRT, weighting the measurement to a much higher 34°C. A color based algorithm would be a more conservative method of identifying plant from soil. It should be adjustable to identify brighter green and omit shaded leaves and soil.

A time series of the difference between the median temperature of each segmented thermal image and that of the full thermal image is shown in figure 3.18. As shown in the sample images, the segmented and full image means do vary, but a pattern is hard to discern. The range of temperature difference for mature plants and shaded soil scene was 5.8 °C, while the full canopy scene had a range of only 4.6 °C. This was expected because the bulk of what was segmented in the open canopy scene, shaded soil, would respond more slowly to changes in temperature compared with the segmented shaded leaves of the complete canopy image. The scene with the young soybean plants had the largest range, 10.4 °C. This was because the soil was exposed to direct sunlight which influenced the temperature without segmentation.

As shown in the images of figures 3.15-3.17, the segmentation algorithm was not always accurate. A segmenting algorithm that could identify color, instead of relying on intensity contrast, would help to reduce the influence of soil temperature in calculations. Further study, with a wider variety of scenes, over a longer period, and during days with extreme temperatures would provide a better baseline from which to draw conclusions.

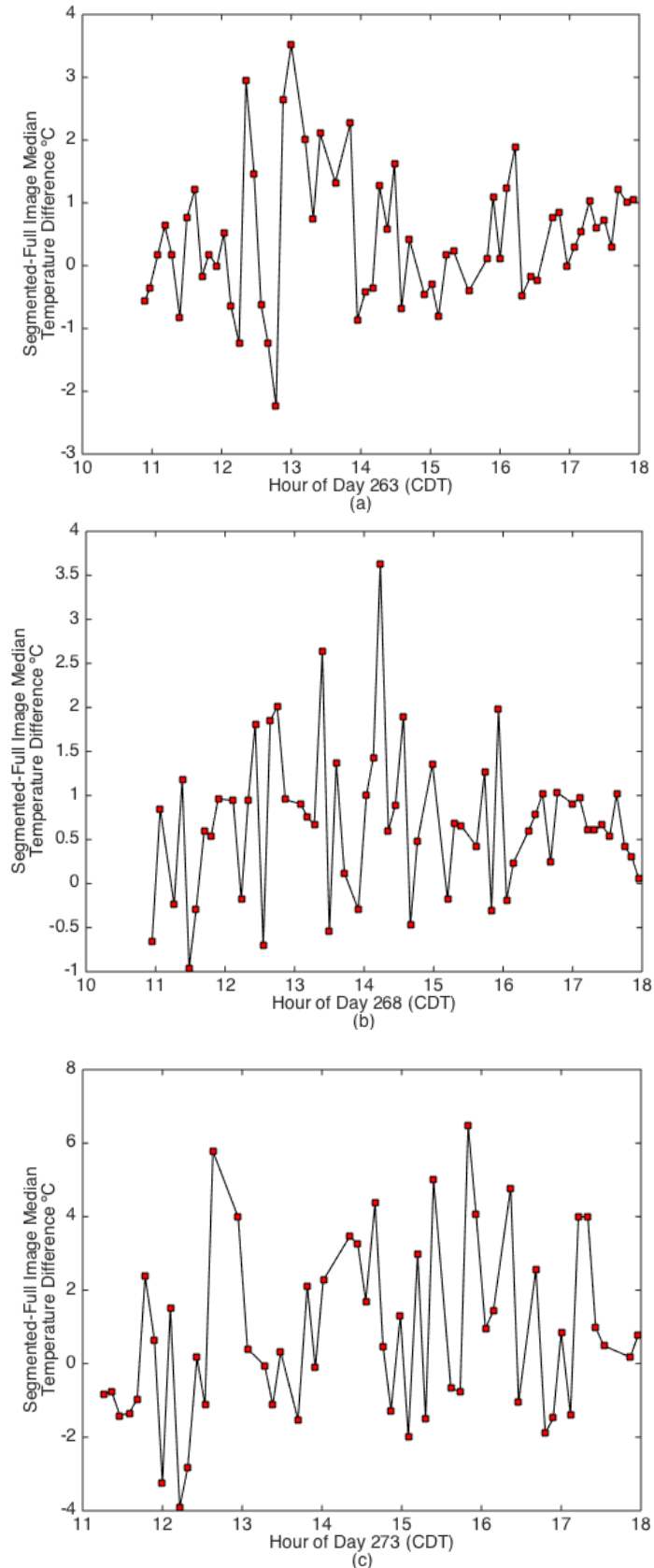


Figure 3.18. Difference in median temperature between the segmented and full thermal images for (a) mature, open canopy, (b) mature complete canopy, and (c) young plants with exposed soil.

CONCLUSION

An instrument that used miniature LWIR and visible cameras to image a crop canopy was built for the purpose of identifying plant temperature within a field of view. To accomplish this, a PCB was designed as a platform to connect both imagers to a microprocessor that automated tasks such as displaying and recording images. The PCB provided a platform for the instrument that could be modified to fit the experimental tasks at hand. This instrument could be operated as a self-contained data-logger, as was demonstrated in the calibration experiment, or in conjunction with a dedicated data logger as was demonstrated in the field tests.

A calibration procedure with circulating water as an emissive source was used to calibrate the radiometric, or thermal, output of the LWIR camera to scene temperature. The water acted as a uniform target that could be heated, while the PCB was able to set the desired camera temperature by means of a thermoelectric module on the LWIR camera housing. Within the limits of expected field conditions, 20 to 40 °C, a quadratic model that estimated scene temperature based on internal and external camera temperature, and camera pixel values had a RMSE of 0.65°C. This model could be implemented in the firmware of the MSICC, making real-time temperature conversions possible.

A segmentation algorithm that relied on intensity differences within an image was used to separate plant pixels from soil pixels. This method was tested with images recorded in field experiments. The algorithm had varying levels of effectiveness in identifying a plant within a scene, but performed best when soil was visible within the field of view. When the image was only of a plant canopy, the algorithm separated

shaded parts of the plant from those exposed to direct sunlight. Integrating a color-based algorithm, with the addition of an IR filter, would likely improve plant identification. Image alignment between the visible and LWIR cameras was accomplished by simply translating the images because both cameras had fixed focus lenses and were positioned with fixed geometry between the two.

Integrating the segmentation process in real time, along with the addition of radiometric output, would require additional processing power not available with a single microprocessor. Experiments in the field showed IRT measurements were similar to the output of the instrument validating that the multi-spectral system could be implemented as a non-contact, segmenting temperature measurement system.

CHAPTER 4

APPLICATIONS OF A MOBILE MULTISPECTRAL CROP CANOPY TEMPERATURE SENSOR

ABSTRACT

The Multispectral System for Imaging of a Crop Canopy (MSICC) that combines a miniature LWIR camera with a visible, or RGB, camera has been developed to capture a field of view and derive a plant-specific temperature measurement. This chapter encompasses hardware and image processing modifications to the MSICC as well as experiments using the instrument as a mobile sensor to identify spatial variability. The MSICC was operated on a mobile platform on two different sets of corn plots during June 2017. One set of plots was used to gauge the effectiveness of two segmentation approaches, finding that results depended on elements within the scene, such as the size of the plants and the amount of moisture in the soil. The second set of plots tested the ability of the instrument to identify variation in crop water stress due to varying topsoil depths. The MSICC was able to discern a significant difference in plant temperature between shallow and deep topsoil plots on a day with high temperature and low soil moisture.

INTRODUCTION

Proximal quantification of spatial and temporal variability has multiple applications in precision agriculture including controlling variable rate technology. Real-time quantification of in-field variables can also be used to create maps to inform management decisions. Determining crop stress within a growing season through optical

canopy measurements has been one approach used to identify within-field variability. Specifically, monitoring temperature of a plant in relation to ambient temperature can be used as a stress indicator (Tanner, 1963). A well-watered plant transpires, and its evaporation cools its leaves. A water stressed plant contracts its leaf stomata, restricting transpiration, reducing latent energy loss, and raising its temperature to satisfy its energy balance. Canopy temperature provides an indicator of this response to stress. This relationship has been related to soil water content and used by Jackson et al. (1981) to formulate a crop water stress index that has been applied widely to irrigation scheduling (Möller et al., 2007; O'Shaughnessy et al., 2011b). Plant stress of this nature can also be tied to such factors as soil depth and even leaf diseases (Lee et al., 2010).

Approaches to plant stress detection have focused on spectral reflectance indices in visible and near-infrared wavelength ranges and crop canopy temperature measurements by thermographic or radiometric methods, generally in the long wave infrared (LWIR) 8-14 μm wavelength range (Fuchs and Tanner, 1966). Sensing of canopy temperature has been widely practiced using single point radiometric sensors, such as infrared thermometers (IRT). Canopy temperature methods are useful in determining a water stress index for scheduling irrigation. To garner useful information about spatial variability throughout a field instruments need to be deployed to capture data spatially and for significant periods of time. Sadler et al. (2002) accomplished this by mounting multiple IRTs on a center pivot irrigation system to measure crop water stress of corn and identify spatial variations by logging variations in temperature. There are limitations to IRTs because the field of view may include non-crop components, particularly soil, which can make the plant canopy temperature measurement inaccurate.

Therefore, estimating canopy temperature in this manner requires eliminating the effect of the soil background in the sensor field of view. Thus, a complete canopy is desirable to make the most accurate measurements of plant temperature with an IRT.

Thermal imaging has been used to measure temperature within a field of view and identify parts of the image that are non-crop components. A thermal infrared camera captures electromagnetic emission of a surface, which would be critical in identifying a stressed plant (Cohen et al., 2005). Visible images capture light reflected from a surface allowing identification of soil or leaves that are shaded within a field a view (Lee et al. 2010). Compiling these two spectral images together it is possible to segment the regions of interest, eliminating the unwanted noise (i.e. soil and shaded leaves) that would contribute to error in an aggregate measurement. This multispectral method is not limited to use on a full canopy or at later crop growth stages (Zia et al., 2013; Mangus et al., 2016). However, implementation of imaging methods has been more cumbersome than the use of IRTs, requiring more equipment and processing abilities.

Thermal imaging of a crop canopy from above requires a sufficient distance above the crop to capture a wide area in the field of view. A truck crane for vineyards (Möller et al., 2007) and an unmanned aerial vehicle (UAV) in a pistachio orchard (Gonzalez-Dugo et al., 2015) were used to fulfill this height requirement. Although thermal imaging has been used on agronomic crops in a greenhouse (Mangus et al., 2016), previous field-based approaches have focused on tree and vine crops. Their discontinuous canopies and large physical size make it possible to use systems that capture a larger field of view with a lower resolution, such as 12 cm (Gonzalez-Dugo et al., 2012). The high cost of these systems, paired with the high spatial resolution

required due to the physical characteristics of a typical crop canopy has held back the use of this approach in grain crops.

Machine vision has been utilized in precision agriculture to discriminate areas within an image based upon vegetative properties. Algorithms that can automatically accomplish this can be used for mechanical or chemical site-specific treatments (Guijarro et al., 2011). Hamuda et al. (2016) reviewed the methods of identifying vegetation contained within a color image. The first stage of a two-step process was to apply pre-processing procedures such as color correction and contrast enhancement. In the second stage, a binary image was formed by classifying each pixel as background or as plant (Meyer and Camargo-Neto, 2008). There are three primary types of approaches used for this extraction: color index-based, threshold based, and learning based (Hamuda et al., 2016).

Commercial digital cameras provide an image output in which each pixel value is composed of components of red, green, and blue (RGB). Chromatic coordinates, r , g and b , are derived from the normalized RGB components, R^* , G^* , and B^* . These chromatic coordinates are used to create indices that focus on specific colors of interest.

$$R^* = \frac{R}{R_{max}}, G^* = \frac{G}{G_{max}}, B^* = \frac{B}{B_{max}} \quad (4.1)$$

where:

R , G , and B are the separate color components of each specific pixel, and

R_{max} , G_{max} , and B_{max} are the maximum values of each color component within an image

$$r = \frac{R^*}{R^*+G^*+B^*}, g = \frac{G^*}{R^*+G^*+B^*}, b = \frac{B^*}{R^*+G^*+B^*} \quad (4.2)$$

Woebbecke et al. (1995) concluded from a comparison of color vegetative indices that the Excess Green Index (ExG) was most successful due its near-binary output in separating plant from soil.

$$ExG = 2g - r - b \quad (4.3)$$

Meyer et al. (1999) used the Excess Red Index (ExR) coupled with shape parameters to identify plants within an image.

$$ExR = 1.3r - g \quad (4.4)$$

Otsu (1979) developed a method that converts pixels from a grayscale image to binary values based on intra-image intensity. A segmentation threshold was derived by treating the image histogram as bimodal, separating foreground and background by reducing in-class variance. Although this method is widely used, it suffers from mis-identification of pixels and slow processing when compared to using the mean intensity within an image for object discrimination (Hamuda et al., 2016; Guijarro et al., 2011). Meyer and Neto (2008) tested the efficacy of applying Otsu's method for thresholding to ExG. This was compared against a binary image created by subtracting a modified version of the ExR vegetative index from ExG.

$$ExG - ExR = 3g - 2.3r - b \quad (4.5)$$

It was found that the ExG-ExR (ExGR) and ExG+Otsu had similar performance with around 90% success when compared with manually processed images. The ExGR identified singular plants in a variety of backgrounds well because ExG is heavily weighted by soil.

Learning-based approaches have provided slight improvements in segmentation in varying illumination conditions through clustering to extract plant textures and use of

alternate color spaces besides RGB. These adaptive approaches require more complex computations and as such applications have been limited. Overall, the performance of each method has varied based upon lighting conditions, shadows, and the complexity of the background (Hamuda et al., 2016).

A number of limitations exist relative to using thermographic and thermometric approaches to mapping variability within a field. Infrared thermometers can be mounted on in-field equipment but these single point sensors do not provide the spatial resolution of thermal cameras. Using an IRT to measure temperature of a complete canopy would eliminate bias due to soil temperatures, but shaded areas of a crop can vary significantly from sunlit portions (Han et al., 2016). The height required to garner applicable data from thermal imaging of crop canopies has generally restricted use of this approach to aerial platforms such as cranes and UAVs (Gonzalez-Dugo et al., 2015; Möller et al., 2007).

The design of the MSICC, a system that used miniature LWIR and visible light cameras to identify a plant's temperature, was described in chapter 3. The initial experiments with the MSICC focused on its high time resolution capabilities by using it to image a single point in a field for a prolonged period. To make the MSICC capable of capturing images while being mounted on a mobile platform, hardware and software changes were needed. Implementation of color-based vegetative indices to be used in image processing required added filtering of the visible camera. The MSICC needed to be repackaged into a compact housing to make a system with the portability required for mobile data logging. The updated instrument could then be used in a field to capture high resolution images of the spatial variability of crop canopy temperature throughout a field.

Objectives

The overall objective of this research was to use the MSICC on a mobile platform to identify variability of plant stress within a field. Specific objectives were to:

- Adapt the MSICC to be used as a mobile instrument through hardware and software modifications.
- Facilitate identification of crop within an image using color-based vegetative indices by changing the lens/filter component of the visible camera.
- Evaluate ExG and ExGR vegetative indices for integration into a future version of MSICC capable of identifying crop temperature in real-time.
- Identify spatial variability within a field by using the MSICC to make temperature measurements from spatially dense sample points.

MATERIALS AND METHODS

Hardware and Platform

The development of the MSICC and initial evaluation of its capabilities are described in chapter 3. For this experiment, the MSICC was modified to allow it to be used on a mobile platform. The MSICC was updated to implement functions previously carried out by the data-logger. Without a dedicated data-logger or the need to mount it in the field, the instrument was housed in a compact enclosure without environmental sealing. The visible camera remained the same, but its lens was changed to a wider 2.8 mm, corresponding to a 75.6° field of view (the LWIR camera has a 51° lens). An infrared cutoff filter was added to the visible camera lens to limit the imager's sensitivity in the near-infrared region, enabling the use of color-based vegetative indices. The LCD

was mounted on the outside of the box, so that the area imaged by the LWIR camera could be displayed for alignment.

Hardware and software changes to the MSICC allowed it to incorporate functions that were performed previously by an external data-logger. The firmware utilized the Teensy Development Board (PJRC.COM LLC, Sherwood, OR) real-time clock library to time stamp images. The SDI-12 signal from the Apogee SI-411 IRT (Apogee Instruments, Logan, UT) was routed to an unused pin on the Teensy and an open source SDI-12 library was modified to work within the MSICC's firmware (see Appendix 2 for details). These created a mobile stand-alone MSICC that could acquire images on a time interval basis or by external triggering.

To remotely communicate with the MSICC, a Visual Basic (Microsoft, Redmond, WA) application was created. The application compiled a serial packet containing location information and number of images to capture, and transmitted it to the MSICC over USB. The MSICC would carry out the command and reply with a confirmation when the requested images had been captured. The MSICC stored the images as well as a table containing the image name and the corresponding received serial message containing the image metadata.

A mobile arm was fabricated to allow the MSICC to be easily adjusted over different row positions in a field. The MSICC was fastened to a tripod-mounted telescopic boom. The tripod was placed in the bed of a utility vehicle, adding height and making it mobile. A diagram of the setup is shown in figure 4.1. Mounted on the back of the vehicle, the tripod could be raised to a maximum nadir view height of 220 cm. The boom was able to extend to 2m beyond the side of the vehicle, making it capable of

capturing images from up to four rows from a given vehicle position.

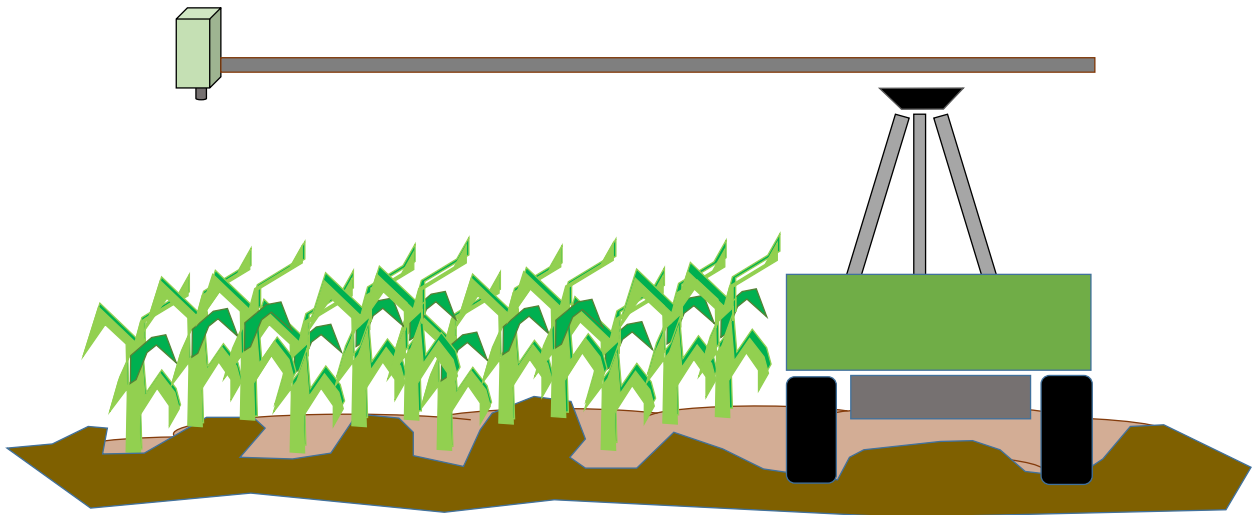


Figure 4.1. Diagram of tripod and boom structure used to capture images with the MSICC up to four rows away from the vehicle position.

Experiment Description

Two sets of experimental plots at University of Missouri's South Farm Research Center were used to test the capabilities of the MSICC in identifying variability of crop temperature throughout a field. Plot A was a field of corn planted at a population of 12100 plants/ha, 115 m long, with eight rows at 76 cm spacing, oriented North-South. Three 12.5 m long sections with three separate treatments were selected within the area. Treatment 1 (plot A1) was an area of the field that in the previous season was planted to sunflower. Corn plants in this area were larger and more vigorous than in the rest of plot A. Treatment 2 (plot A2) was directly adjacent to plot A1, but varied in that it had soybean planted in it the previous year. Treatment 3 (plot A3) had the same conditions as plot A2, but differed because the population was reduced uniformly by 50% to reduce crop cover and increase the visible area of soil.

Within each treatment block of plot A, points were marked at seven equidistant points separated by 1.5m. These flags are visible in the images of the MSICC in operation shown in figure 4.2. Each flagged location was sampled at two boom lengths, with a field of view that contained two rows. Each flag and boom position had a specific ID tag that enabled each set of measurements to be related back to a position within the field.

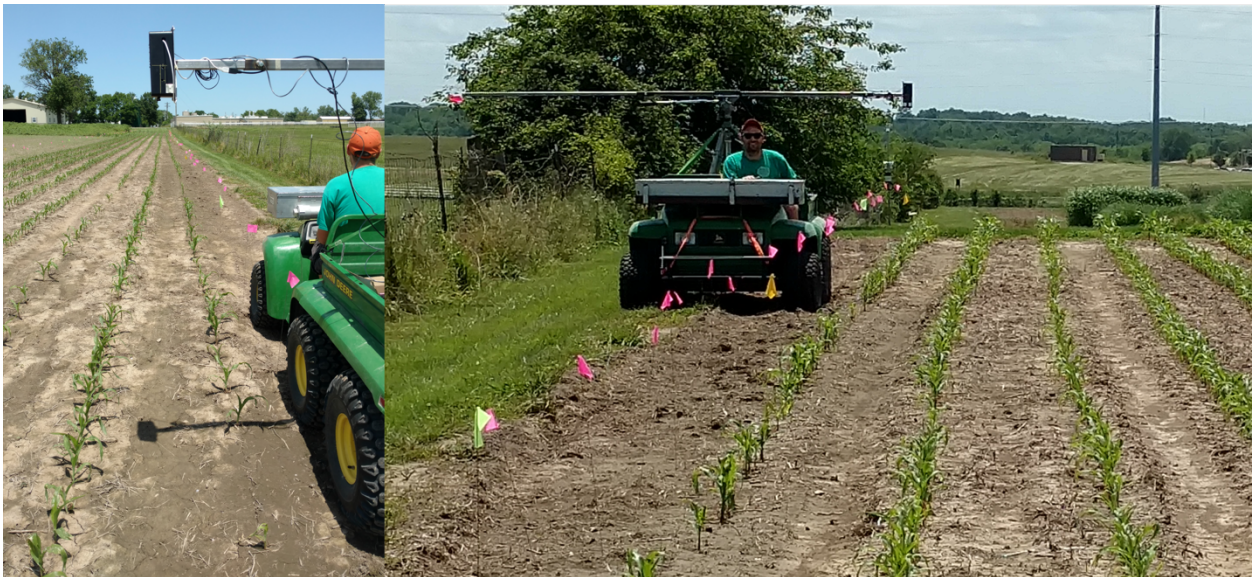


Figure 4.2 The MSICC is shown capturing data within Plot A. The flags in the photo on the right denote a location to be sampled.

Data from plot A were recorded by making two passes on each side of the field, each capturing plants from two rows, oriented parallel to the long dimension of the image, within each image. Thus the four images at each flagged point included a total of eight rows. Using plot A2 as a reference, the MSICC was fixed a height of 120 cm above the crop canopy on each day of data collection. Because adjusting the height of the boom was cumbersome, this height was fixed for the day and the varying heights of plants throughout the field affected the MSICC's measurement. Data were recorded on June 9, 12, 15, 19, 24, and 27 of 2017 on plot A. By June 24, the plants reached heights above

100 cm, so the boom was set at its maximum height of 220 cm. All images were captured within 2 hours of solar noon.

The second set of experiments was performed on four separate blocks of corn in the SPARC plots, referred to as plot B, planted at 12100 plants/ha. SPARC is a research site at South Farm of the University of Missouri that was created in 1982 to study the effect of topsoil depth on crop production (Gantzer and McCarty, 1987). The site is divided into 32 blocks (22.9 m x 9.1 m) that were constructed to different topsoil depths ranging from zero to approximately 1 m. After a decade of crop production research, the site was fallowed in 1993 until it was repurposed in the spring of 2009 as the site of two new experiments to study the relationship of topsoil depth to crop grain and switchgrass biomass production for renewable energy (Conway et al., 2017). Two eight row plots, plot B1 and B2, with shallow topsoil (5 cm), and two plots, B3 and B4, with deep topsoil (28 and 38 cm) were chosen to investigate differences in water stress due to topsoil depth. Measurements were taken on June 12, 15, 19, 22, and 27 of 2017 on plot B. Cloudy conditions existed only on June 22, while data were recorded in full sunlight on the rest of the days. The vehicle was driven adjacent to the end of the rows, instead of along the length of the rows like in plot A. While two rows were imaged at a time, the plants were oriented perpendicular to the long dimension of the image, or opposite that of plot A. On June 12, each position was measured with boom lengths of 100 and 200 cm into each end of the plot. During the remainder of the study, each position was measured with one boom length extending 150 cm into the plot.

Figure 4.3 shows the arrangement of image acquisition locations within plots A and B along with the location identifier used in this experiment.

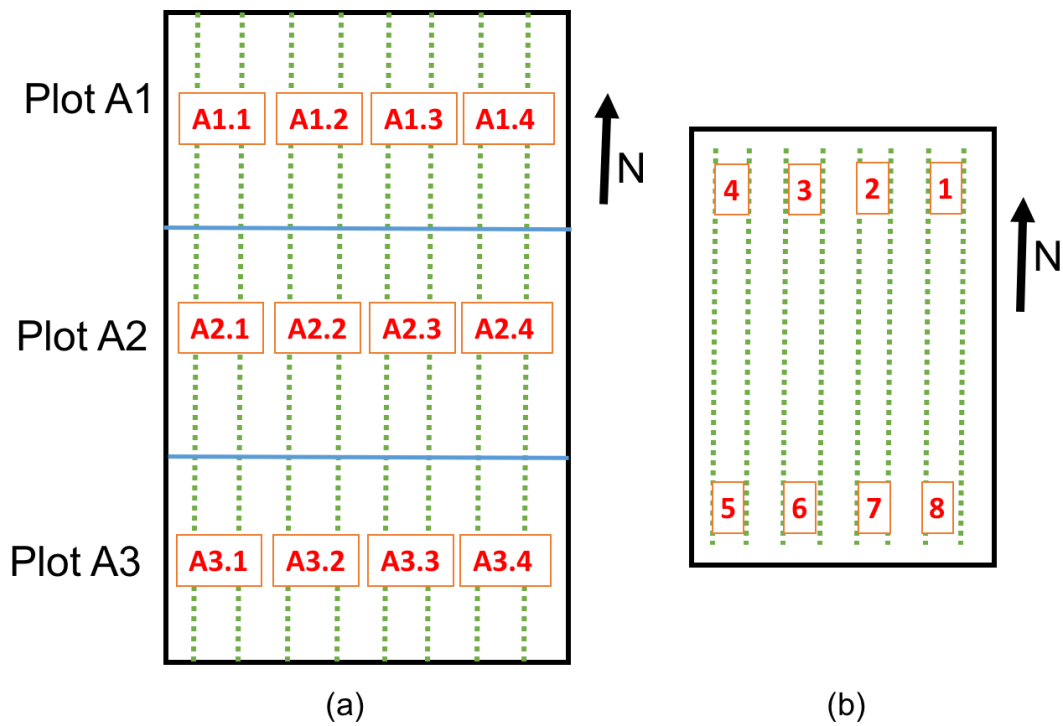


Figure 4.3. a) Imaging locations within plot A with location code. b) Locations of points within each B plot.

Image Processing

Images from the Lepton LWIR camera were saved as text files that recorded raw digital values as well as temperature information from the camera. The measured values were converted to temperatures using the calibration formula developed in chapter 3.

That formula, shown to have an accuracy of 0.65°C in a validation dataset, is shown in eq 4.6.

$$\begin{aligned}
 T_{pixel} = & A * 0.229 + B * 95.764 - C * 111.85 & (4.6) \\
 & -A * B * 0.009 + A * C * 0.011 \\
 & -B * C * 2.611 - A^2 * (1.575 \times 10^{-5}) \\
 & +B^2 * 1.1355 + C^2 * 1.486 - 727.5
 \end{aligned}$$

where

T_{pixel} =temperature of pixel (°C)

A= raw counts of pixel

B = camera shutter temperature (°C)

C = temperature of the camera sensor (°C)

Visible images were captured as compressed JPEG images. Prior to processing, contrast of the visible images was lowered for each RGB component equally using the MATLAB (MathWorks, Natick, MA) command *imadjust*. When operating in bright sunlight conditions the camera produced images high in contrast. Lowering the contrast of an image added detail to the brightest areas and improved segmentation performance. Without a lowering in contrast, pixels from the most reflective leaves would not be identified as vegetation.

Colors contained within an image background varied based on current soil moisture and shading from the plants. The visible camera lens had different geometrical distortion than the lens of the LWIR camera, and was corrected using an open source MATLAB application, *lendistort* (see appendix 2). The field of view of the corrected visible image was cropped to match the field of view of the LWIR camera lens. Images from the two cameras were aligned daily by imaging a fence, which provided a perpendicular set of straight lines that could be identified within the LWIR and RGB images. In figure 4.4 the LWIR image is imposed on a corrected visible image of the in-field alignment target.

Two vegetative indices were tested for their ability to identify plant pixels within an image that could then be used to form a region of interest in the thermal image. The ExG index (Woebbecke et al., 1995; equation 4.2) was calculated for each image and then an Otsu threshold (Otsu, 1979) was applied. The ExGR (Meyers and Neto, 2008)

was modified, as others have done, to work with the compressed images from the ArduCAM. This modified index was calculated as: $ExGR=3.3g-2.3r-b$, where g , r and b were the normalized red, green, and blue out of the camera (eq. 4.2).

Once a binary mask was produced from a vegetative index, image processing steps followed the procedure described in chapter 3: the image was down-sampled to 80x60 and applied to the thermal image derived from the LWIR camera.

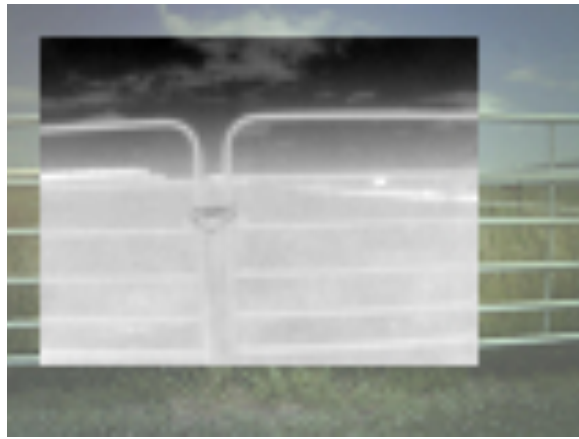


Figure 4.4. A LWIR image overlaid on a corrected visible image using the in-field target as alignment.

RESULTS AND DISCUSSION

Image Processing

Testing the MSICC in plots A1, A2, and A3 over several days resulted in images with varying soil color and crop canopy complexion. This range of conditions provided a data set to test machine vision techniques for identifying vegetation within an image. Figures 4.5-4.11 show visible, full thermal, and segmented images from the same location within Plot A2. Although the vehicle was positioned in the same location each time, slight variations in horizontal positioning of the boom and varying height above canopy caused the view to vary from day to day.

Figure 4.5c and 4.5d show images from June 9 segmented using ExG and ExGR, respectively,. Near the right edge of the frame, the ExGR vegetative index misclassifies the dry, reflective soil as vegetation. Under the dry conditions of June 9 and June 12 (fig. 4.5 and 4.6), ExG does not have such errors in classification, leading to a 1.37 °C lower median temperature compared to the ExGR segmented image.

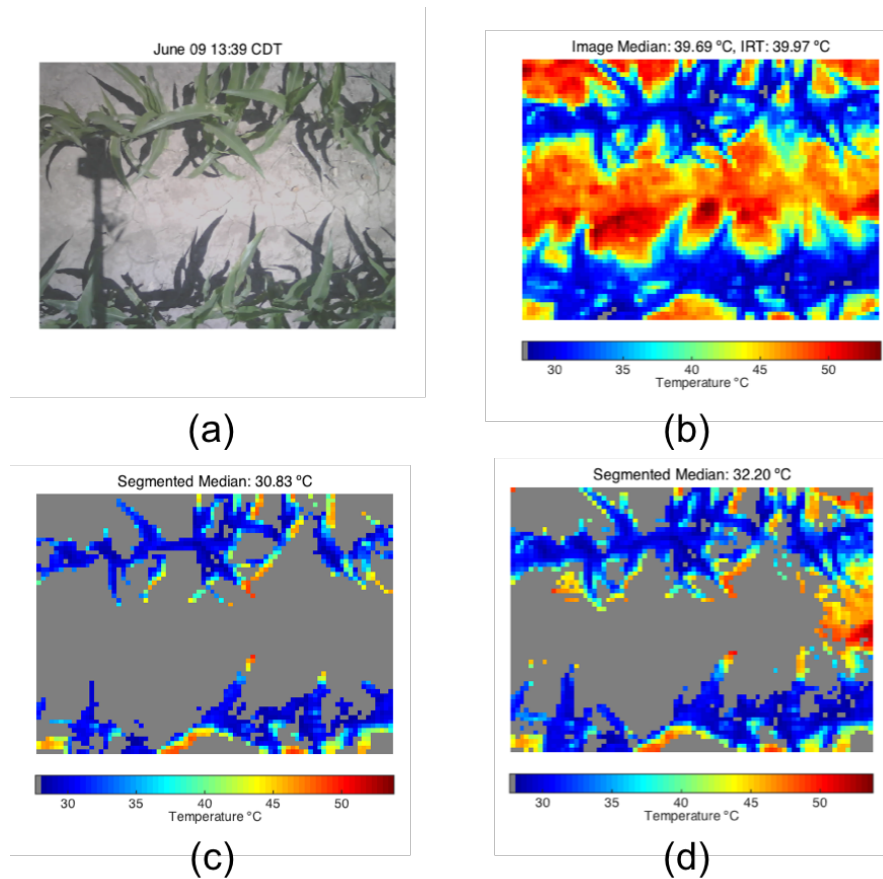


Figure 4.5 a) Visible camera image cropped to LWIR camera field of view on June 9. b) LWIR image with calibration applied. c) Segmented image using ExG technique. d) Segmented image using ExGR technique.

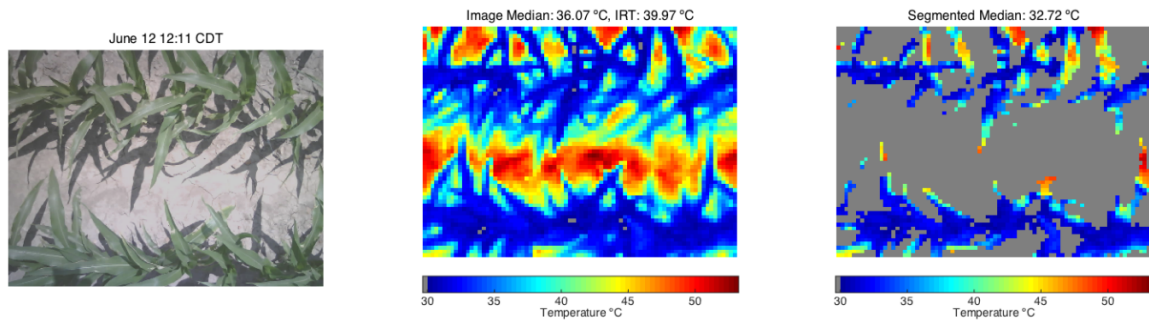


Figure 4.6. Left: Visible camera image cropped to LWIR camera field of view on June 12. Center: LWIR image with calibration applied. Right: Segmented image using ExG technique.

On June 15, the ExG vegetative index (fig. 4.7c) no longer classified pixels as well as ExGR (fig. 4.7d). Soil moisture increased, and the ExGR did not misclassify soil as vegetation, while the ExG was too conservative with identification of vegetation pixels. The moist soil was much cooler on this day, thus the difference between temperature measurements from images segmented by the two methods was only 0.19 °C.

Figure 4.8 shows that the fraction of total canopy included within the field of view began to decrease on June 19 because the tripod was adjusted to the maximum elevation and the MSICC could no longer maintain the same height above the top of the crop canopy. While some plant pixels were not identified as vegetation, the ExGR did not classify soil pixels as vegetation. June 19 had the lowest range of temperatures as the difference between shaded and unshaded soil was less than 10 °C, whereas on June 9, 12, and 15 differences were greater than 20 °C.

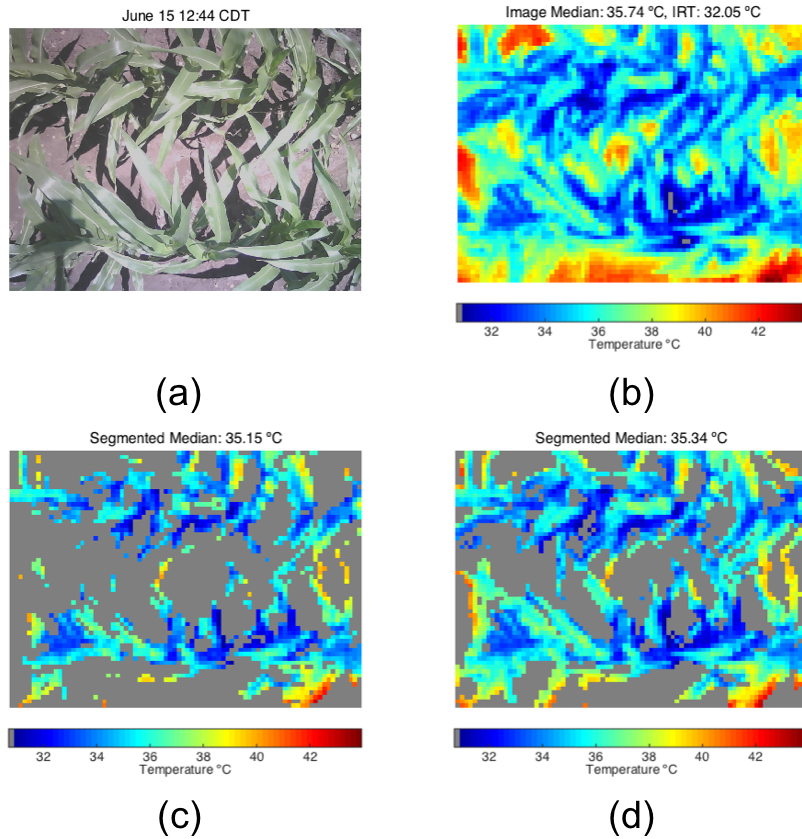


Figure 4.7 a) Visible camera image cropped to LWIR camera field of view on June 15. b) LWIR image with calibration applied. c) Segmented image using ExG technique. d) Segmented image using ExGR technique.

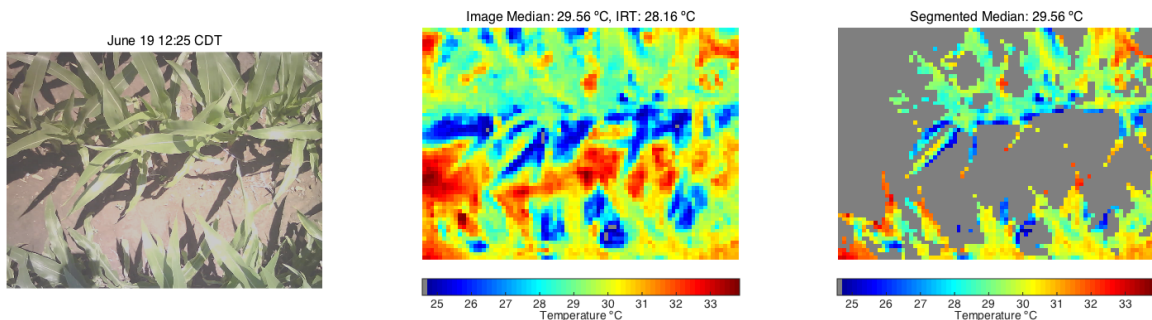


Figure 4.8 Left: Visible camera image cropped to LWIR camera field of view on June 19. Center: LWIR image with calibration applied. Right: Segmented image using ExGR technique.

On June 24 (fig. 4.9), the plant height within plot A2 was in excess of 100 cm. The maximum height limit of the MSICC boom limited the field of view at the top of the canopy to the area between the two rows. The topmost leaves between the rows are included, but segmentation fails to remove all of the shaded area pixels. The IRT field of view was wider and therefore measured more of the crop canopy, but soil pixels were included and were at a considerably higher temperature as shown in the thermal image. By Jun 27 (fig. 4.10) the height of the crop did not allow imaging of the upper canopy and was only capturing an area between plant rows. This led to a decrease in the ability of segmentation to identify plant pixels.

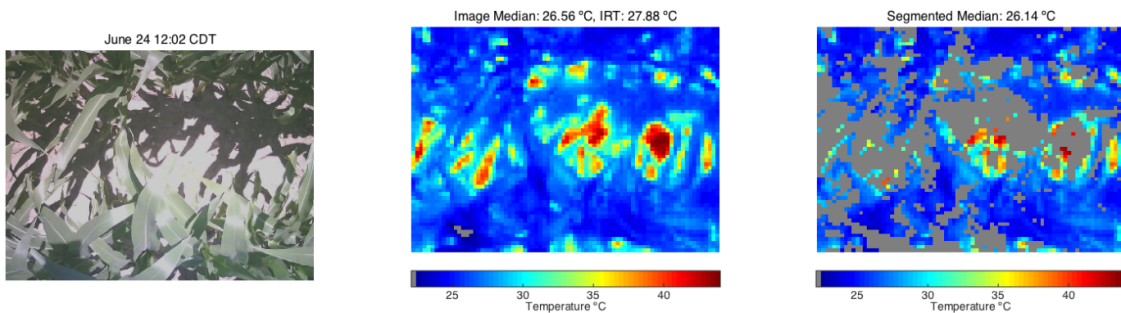


Figure 4.9. Left: Visible camera image cropped to LWIR camera field of view on June 24. Center: LWIR image with calibration applied. Right: Segmented image using ExGR technique.

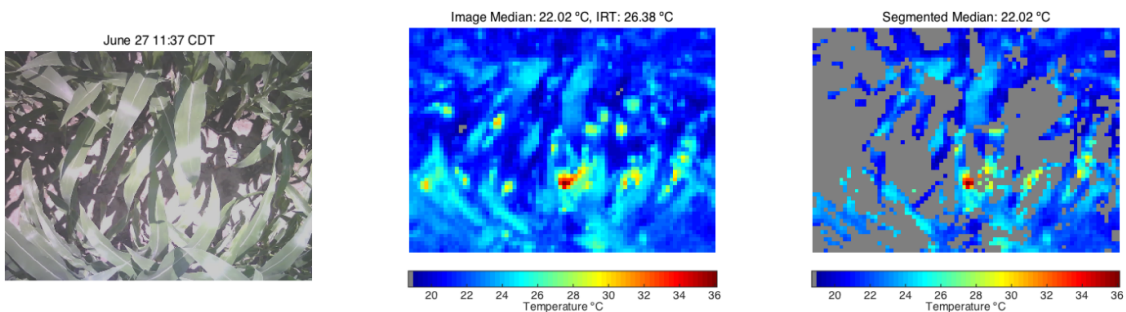


Figure 4.10. Left: Visible camera image cropped to LWIR camera field of view on June 27. Center: LWIR image with calibration applied. Right: Segmented image using ExGR technique.

Because these images were captured under a range of conditions they provided a good data set to evaluate different vegetative indices. ExG performed well with low plant cover, but ExGR was better at correctly identifying pixels as the plants matured. Several factors negatively impacted matching the images from the visible and LWIR cameras. The complex distortion of the visible camera made it difficult to apply corrections to accurately match the LWIR lens. The parallax introduced by using two separate imagers, located at separate locations, and coupled with requisite down-sampling of the visible image caused edge alignment issues between the two images. As the distance between the crop and imagers decreased this parallax made correctly matching the two images more difficult. Correcting distortion of the LWIR lens would lower the already limited resolution of the Lepton camera. A visible camera and lens that could be better corrected to match the distortion of the LWIR lens would be an alternative way to improve the image matching process.

The auto-white balance of the ArduCAM visible camera resulted in inconsistent color of its output JPEGs. Color balancing in post-capture was difficult to achieve with the compressed images. Even when a successful color balance was reached, there was not a noticeable improvement in segmentation results. Correcting this issue would require that the ArduCAM be replaced with a camera capable of capturing raw, uncompressed images.

Plot A Results

In figures 4.11-4.16, measurements for each spatial location in plot A are plotted as a series of values. The averages for each location of median temperature values

calculated from three pairs of images, both before and after segmentation, along with IRT measurements and percent cover calculated from the number of kept pixels, are shown. Air temperature was taken from data recorded on a two-minute interval at a weather station within 200 m. The IRT measurements are shown as a source of validation data.

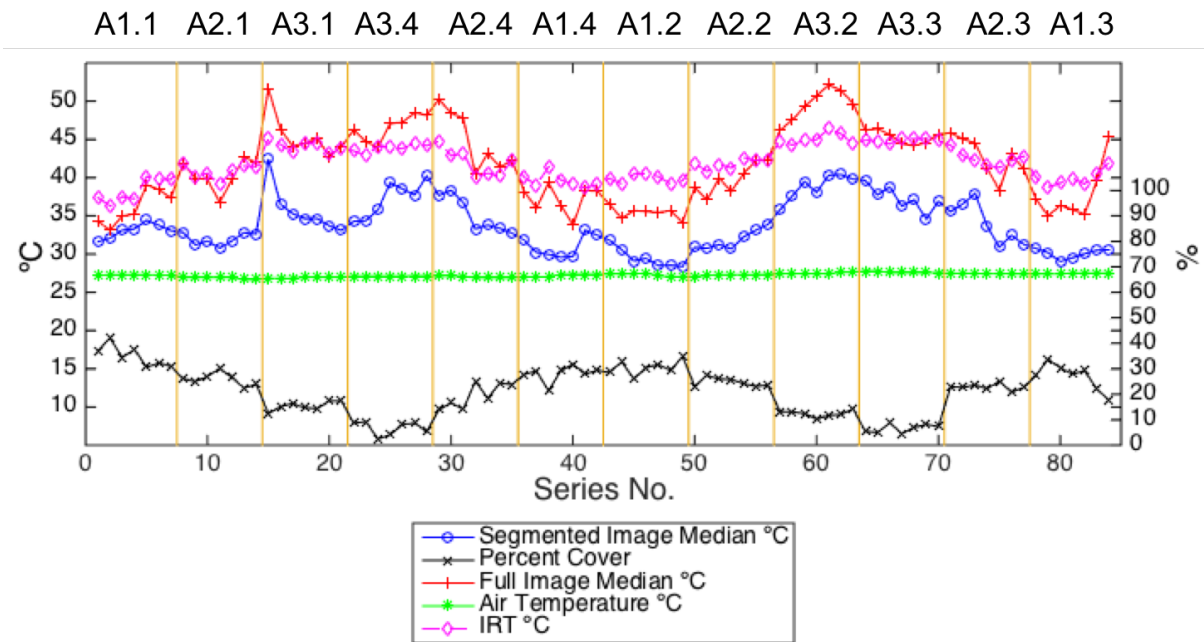


Figure 4.11. Data recorded within Plot A on June 9. Each point represents an average value from four measurements: LWIR full image and segmented image temperatures, IRT temperature, and percentage cover. Sections are labeled with codes described in figure 4.3a.

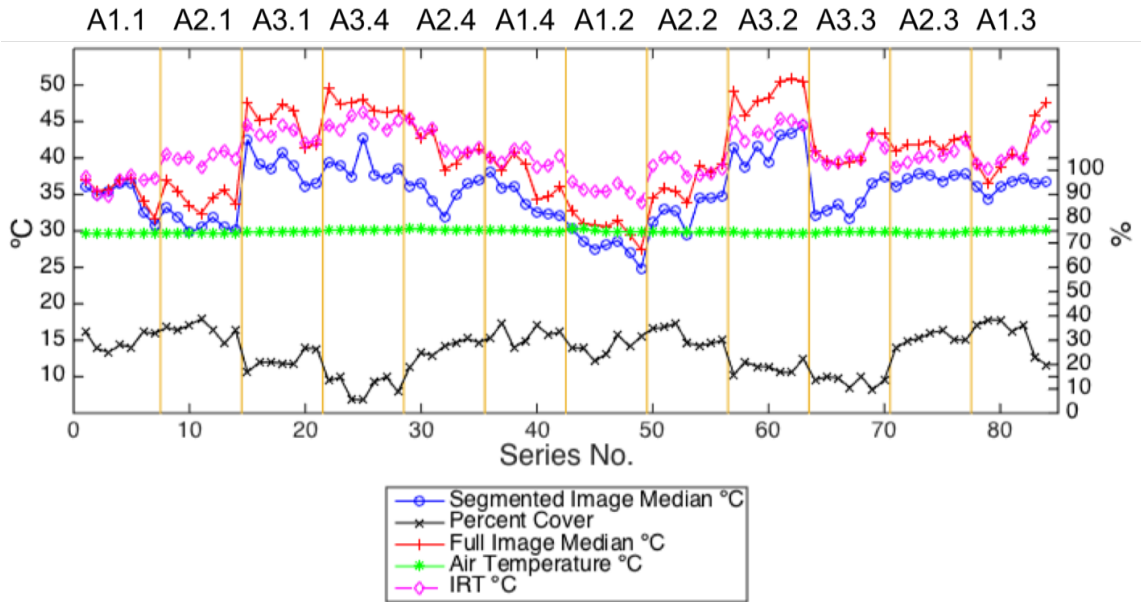


Figure 4.12. Data recorded within Plot A on June 12. Each point represents an average value from four measurements: LWIR full and segmented temperatures, IRT temperature, and percentage cover. Sections are labeled with codes described in figure 4.3a.

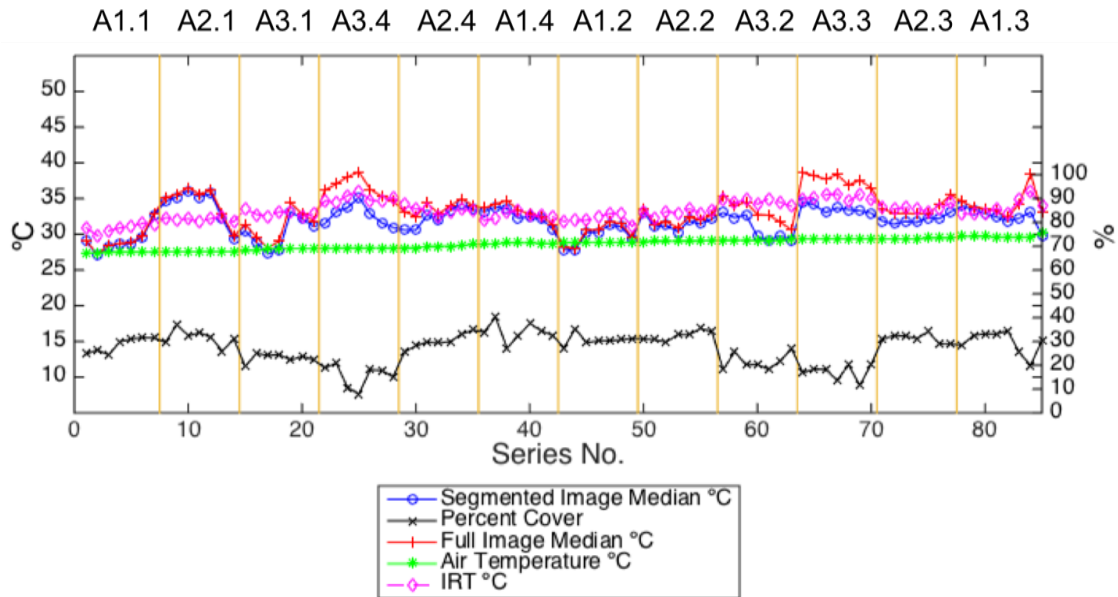


Figure 4.13. Data recorded within Plot A on June 15. Each point represents an average value from four measurements: LWIR full and segmented temperatures, IRT temperature, and percentage cover. Sections are labeled with codes described in figure 4.3a.

As the crop matured, the percentage of the image kept after segmentation increased to a point and then reversed. Percentage cover in plot A increased as expected through June 19. On June 24, the percent of an image kept after segmentation from locations within plot A1 and A2 decreased by as much as 20%. On June 27, similar decreases were seen at locations within plot A3. The boom of the MSICC had reached its maximum height on June 24, and was no longer high enough to capture the full canopy of two rows. The field of view on these dates was of the area between the two rows, which contained large amounts of shadow. The temperatures recorded by the MSICC were also lower because they captured more cooler, shaded leaves instead of sunlit leaves of an exposed canopy.

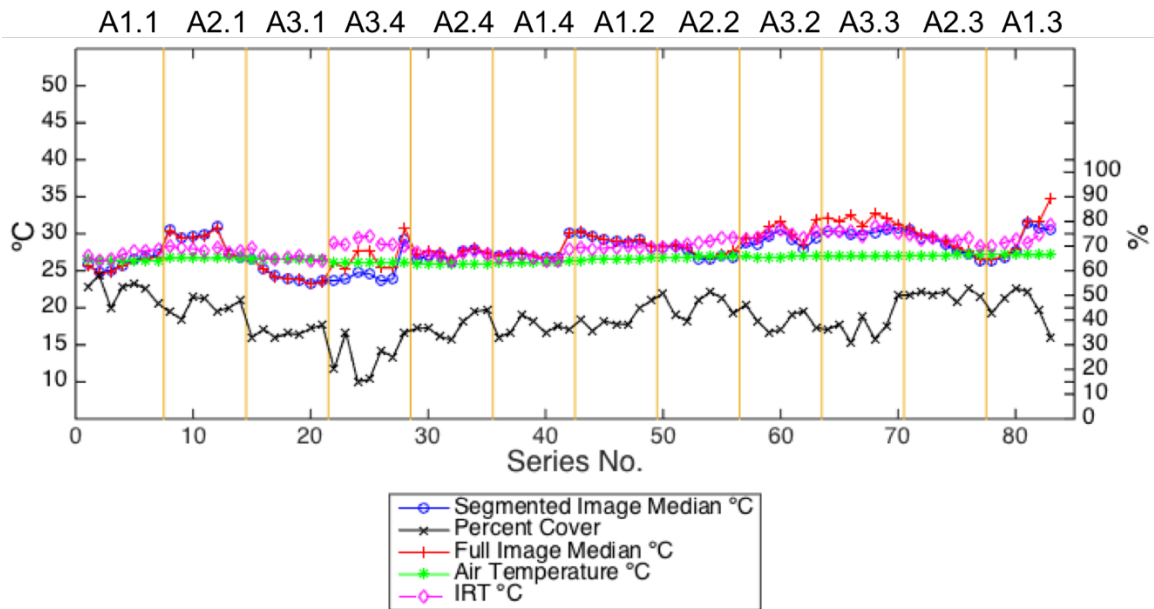


Figure 4.14. Data recorded within Plot A on June 19. Each point represents an average value from four measurements: LWIR full and segmented temperatures, IRT temperature, and percentage cover. Sections are labeled with codes described in figure 4.3a.

The reduced corn plant population within plot A3 allowed significant weed cover to develop within the images and this began to have an effect on segmentation on June 24. The mostly shaded weeds were identified as vegetation, and corresponding pixels from the LWIR were included in the calculation, lowering the median temperature.

IRT temperature measurements exhibited some differences compared to median image temperature values, but general point-to-point trends were similar between the two measurements. On June 24 (fig 4.17) median temperatures taken from images in Plot A1.1 deviated significantly from the IRT measurements. This was because the LWIR camera sensor was not given sufficient time to reach steady state before starting to record measurements.

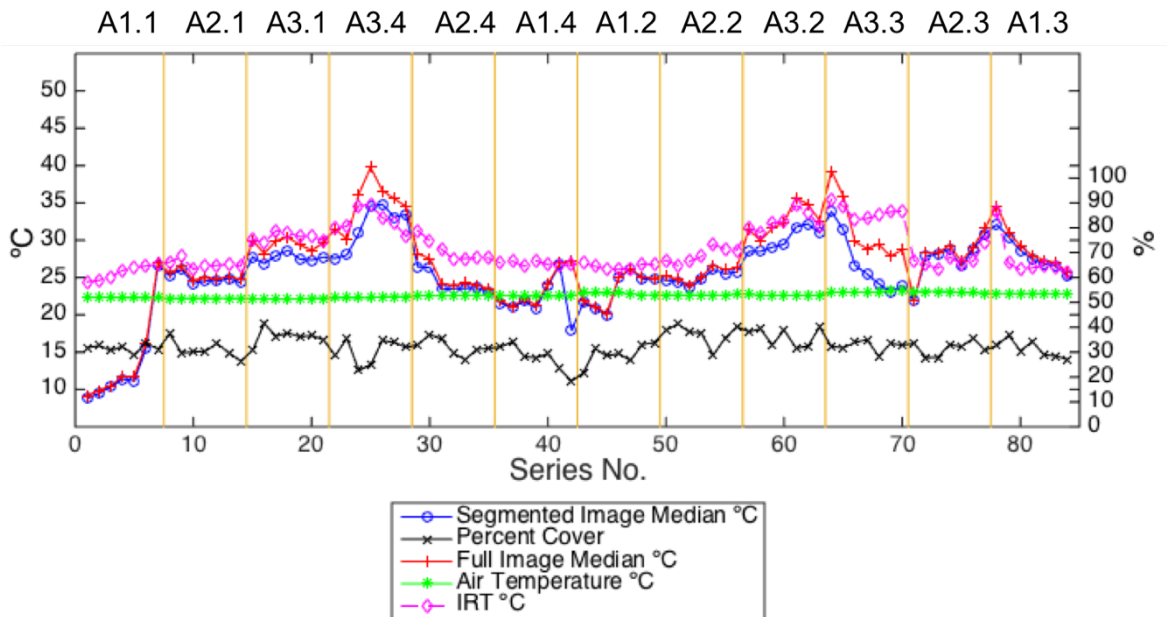


Figure 4.15. Data recorded within Plot A on June 24. Each point represents an average value from four measurements: LWIR full image and segmented image temperatures, IRT temperature, and percentage cover. Sections are labeled with codes described in figure 4.3a.

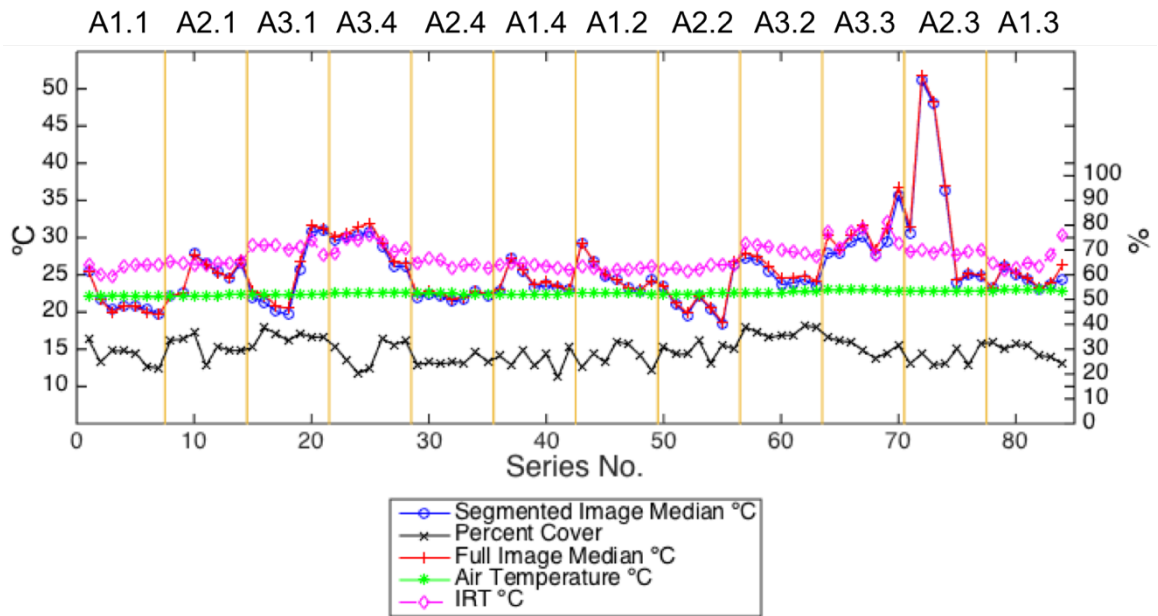


Figure 4.16. Data recorded within Plot A on June 27. Each point represents an average value from four measurements: LWIR full image and segmented image temperatures, IRT temperature, and percentage cover. Sections are labeled with codes described in figure 4.3a.

The difference between the median temperature of segmented images and air temperature from June 9 to 19 in Plot A are shown in figure 4.17. June 24 and 27 were not included because the insufficient height of the MSICC over the crop caused many images to only include the intra-row area. Each pair of rows imaged simultaneously with the MSICC is represented with a separate plot.

For most points within Plot A, temperature differences on June 9 and 12 were the highest. Specifically, Plot A3 and the southern portion of plot A2 had higher temperature differences on June 12 than June 15. This was expected, because of the low soil moisture and heat stress conditions that were present through June 12. The air temperature reached its highest throughout the study on June 12 with an average of 29.9 °C.

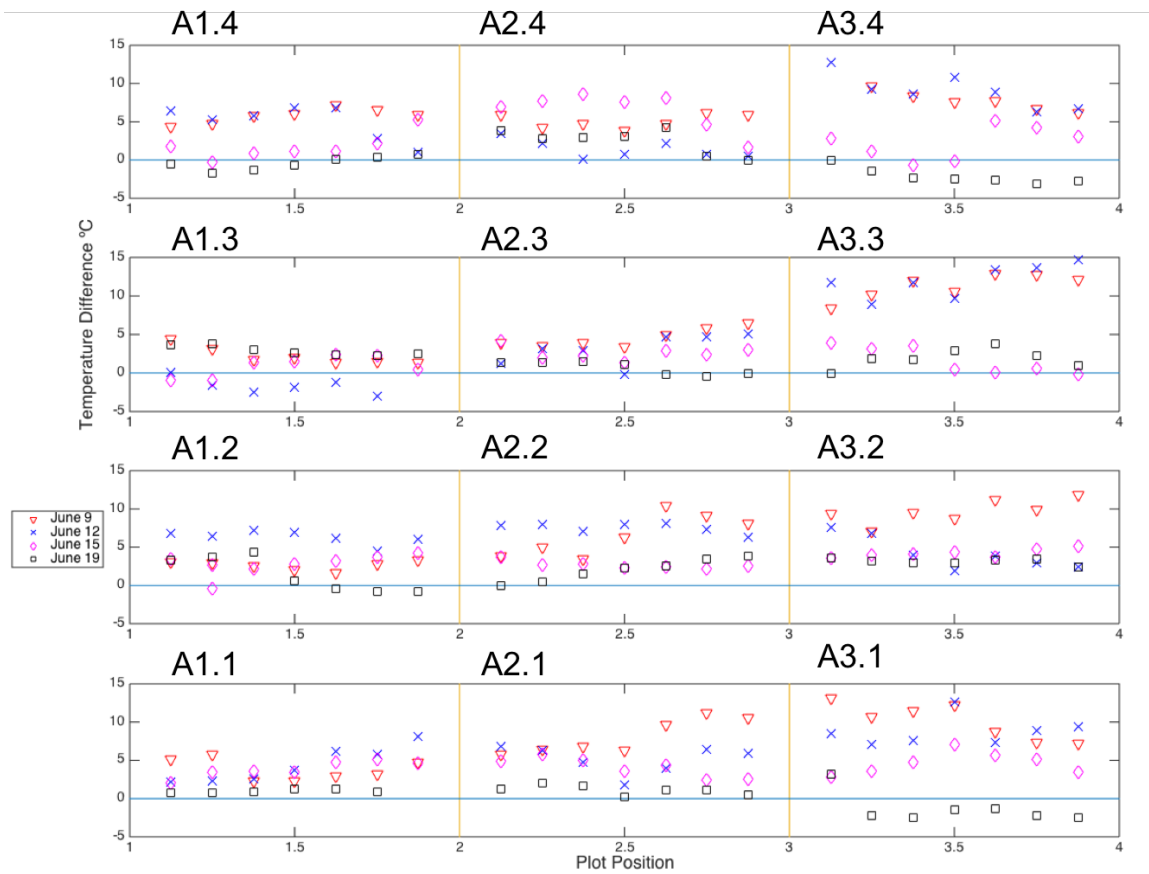


Figure 4.17. Difference between segmented median temperature and current air temperature plotted by location within each treatment area. Each point is an average of three measurements taken on the given day. The codes for location within plot A are shown in figure 4.3a. Plot position increases towards the south.

Between 0100 and 0400 CDT on June 15, 35 mm of precipitation was received on the plots. Soil moisture increased after this event, which led to lower temperature differentials in the areas that were more stressed on June 9 and 12. The difference between temperatures was less in plot A1 with larger, more mature plants compared to the other two treatments. Calculations made from images with a low percentage cover were biased toward higher temperatures because the segmented image still included some

soil pixels. The dry days occurred when cover was lowest, so it was possible the median temperature was driven up because dry soil was hotter than wet soil. With some exceptions, temperature differences were lowest on June 19, the coolest day included within figure 4.17.

Plot B Results

Data from plot B exhibited many characteristics similar to plot A. Figures 4.18-4.22 show the data series for the five days that data were collected on Plot B. On June 12 (fig 4.18), images were taken from two boom lengths on each the north and south side of each plot. Average temperatures for all segmented LWIR images on low-topsoil plots B1 and B2 were 46.1 and 44.35 °C, higher than the 40.6 and 40.3 °C recorded for high-topsoil plots B3 and B4. This was expected because for the shallow topsoil depth in those plots on hot, dry days the lack of available water led to stressed plants. The percent cover on B3 and B4 was higher because the plants were more mature due to less stress earlier in the growing season. The IRT measurements were similar to full image median temperatures on June 12. The difference between segmented and full image temperatures was greater in the plots with less cover (B1 and B2).

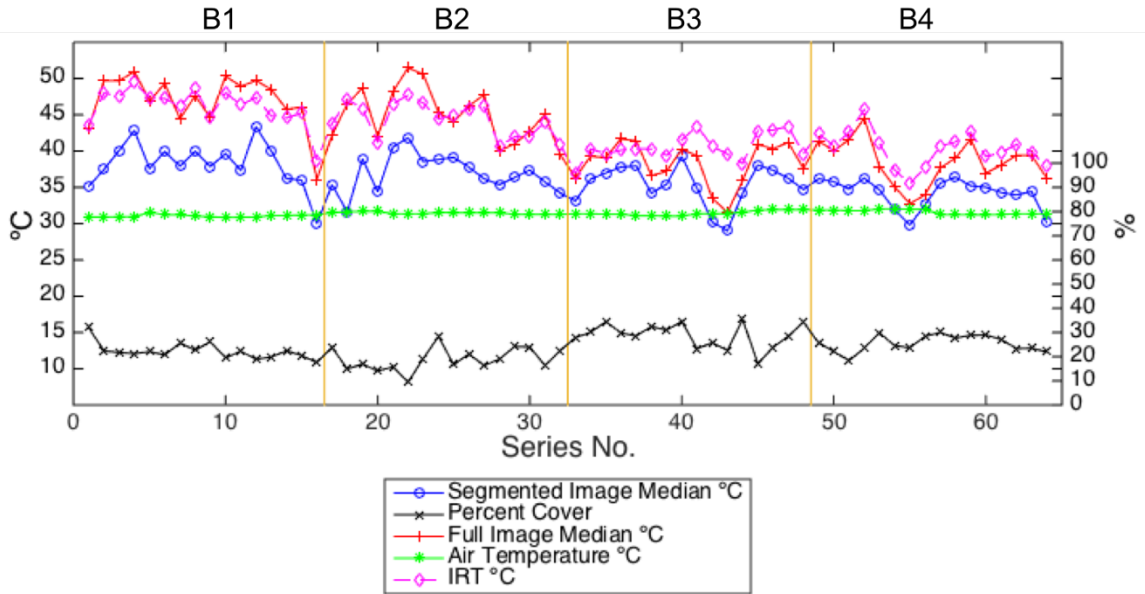


Figure 4.18 Data recorded within Plot B on June 12. Each point represents an average value from four measurements: LWIR full and segmented temperatures, IRT temperature, and percentage cover. Plot changes are denoted by a section break.

Images were recorded at only one boom length from June 15-27. On June 15, the differences in temperature between plots of different topsoil depths were not visually discernable. Plot B2 recorded the highest averages from LWIR segmented images at 37.1 °C, B1 and B3 had similar temperatures of 35.5 and 35.8 °C, and B4 was lowest at 32.6 °C. Percentage of kept pixels continued to increase for most locations on June 15 (fig. 4.19) and June 19 (fig. 4.20). On June 19 the average temperatures were higher for the low topsoil plots, with B1 and B2 at 31.3 and 33.5 °C compared with plot B3 and B4 at 29.1 and 30.3 °C. From June 15 on, the temperatures measured with the LWIR camera also appeared to be different depending on whether they were recorded on the north or south side of the plot. For example, in figure 4.19 the first four points (the north side of the plot) in B1 are all below 32.8 °C, while the next four (south side) are considerable higher reaching 40.0 °C.

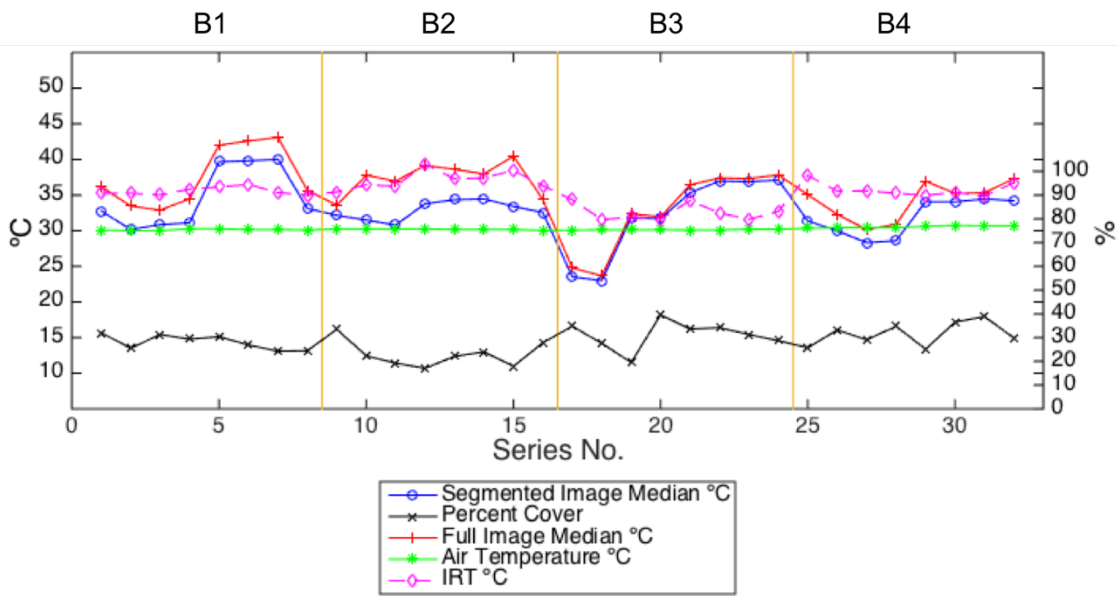


Figure 4.19 Data recorded within Plot B on June 15. Each point represents an average value from four measurements: LWIR full and segmented temperatures, IRT temperature, and percentage cover. Plot changes are denoted by a section break.

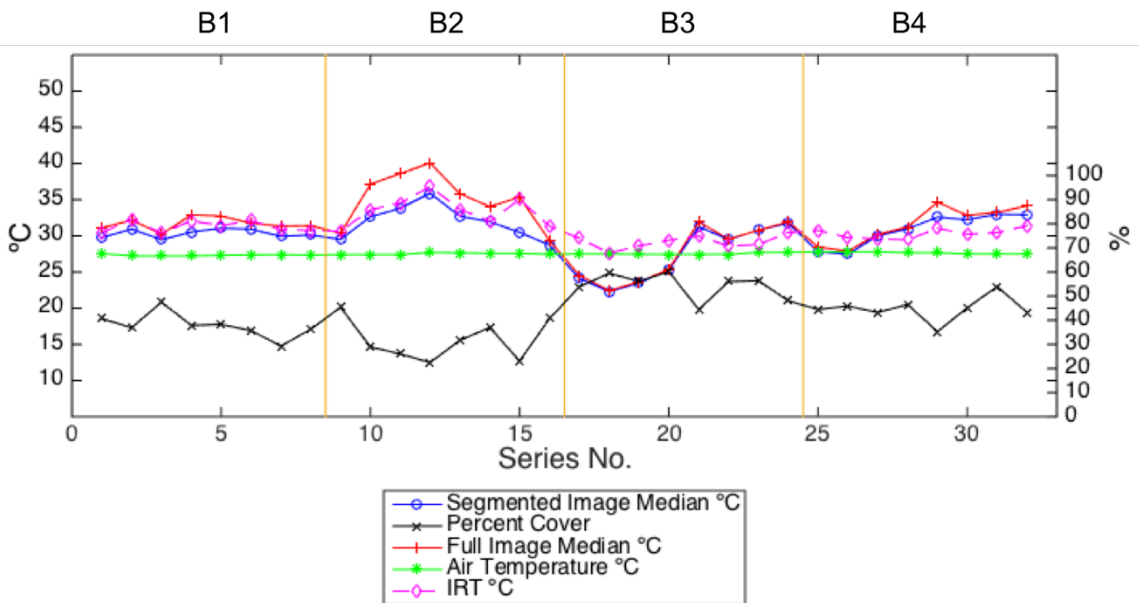


Figure 4.20 Data recorded within Plot B on June 19. Each point represents an average value from four measurements: LWIR full and segmented temperatures, IRT temperature, and percentage cover. Plot changes are denoted by a section break.

For images obtained on June 22 and 27, the segmentation faltered due to field of view limitations cause by insufficient height over the crop as described earlier for plot A. This can be seen in the large decline in percentage cover of plots B3 and B4 shown in figures 4.23 and 4.24. The low temperatures of the first four locations in Plot B1 on June 22 (fig 4.21) were due to recording of measurements before the LWIR camera sensor had approached steady state.

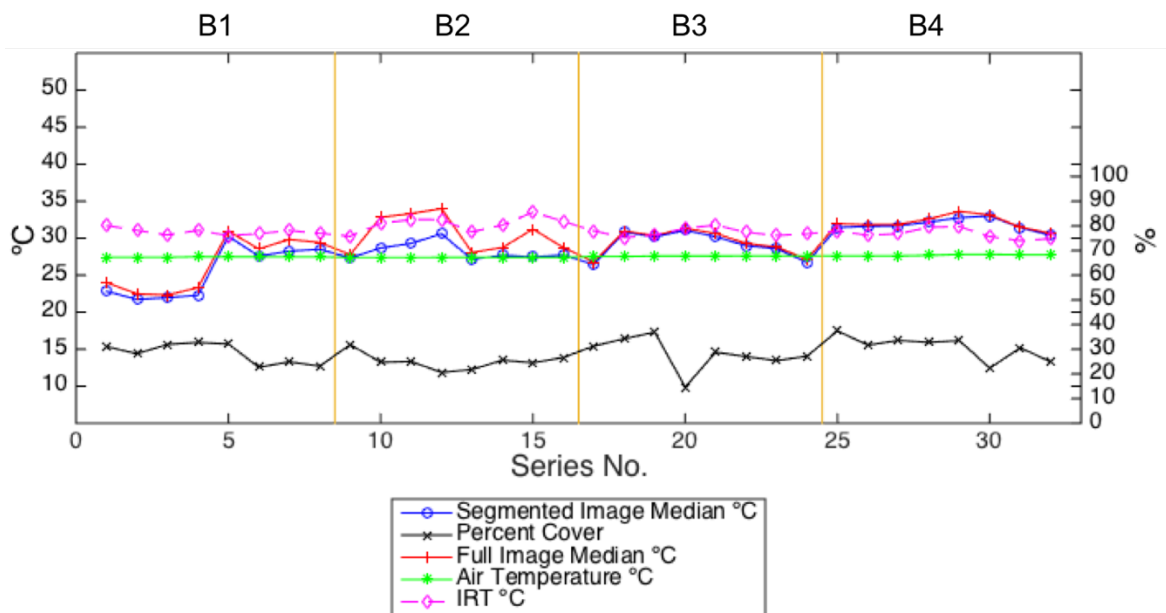


Figure 4.21 Data recorded within Plot B on June 22. Each point represents an average value from four measurements: LWIR full and segmented temperatures, IRT temperature, and percentage cover. Plot changes are denoted by a section break.

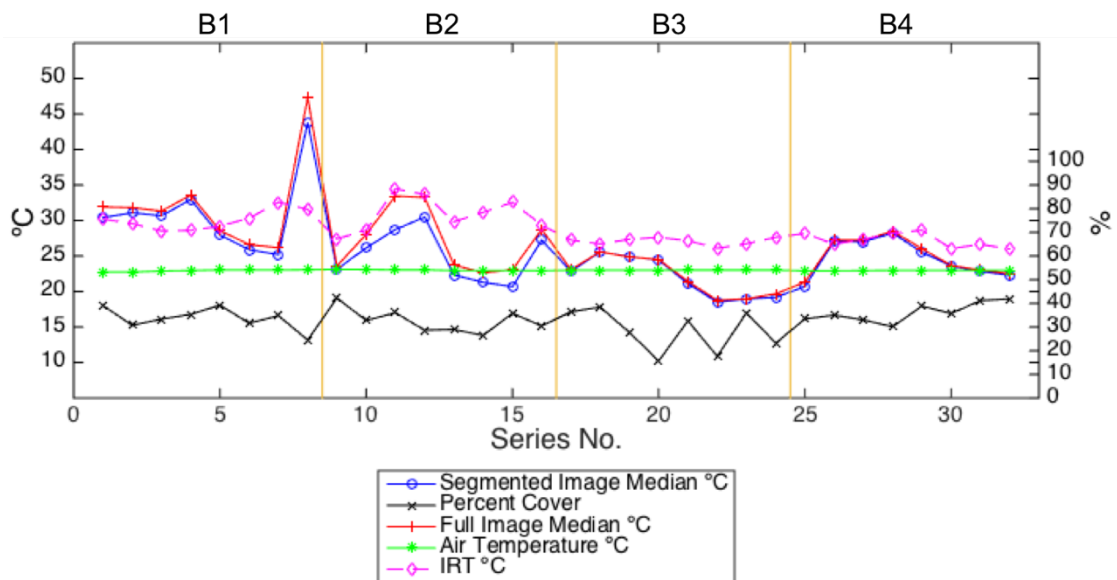


Figure 4.22 Data recorded within Plot B on June 22. Each point represents an average value from four measurements: LWIR full and segmented temperatures, IRT temperature, and percentage cover. Plot changes are denoted by a section break.

The differences between the median temperature of segmented images and air temperature from June 12 to 19 in Plot B are shown in figure 4.23. Data recorded on June 22 and 27 are not shown because the insufficient height of the MSICC over the crop caused many images captured to only include the intra-row area. The eight locations within each plot are represented by two points for June 12 corresponding to the two boom lengths from which measurements were taken. The shallow topsoil plots, B1 and B2, had higher temperature differentials than the deep topsoil plots on June 12 and June 19. On June 12 all plots had consistently elevated temperatures over ambient, ranging from 8.7 °C in B4 to 15.1 °C in plot B1. It was likely that all the plots were seeing heat stress on this date. On June 19, although the low topsoil depth plots had higher temperatures that

the shallow topsoil plots, the highest above ambient was B2 at 5.9 °C, 1.0 °C lower than on June 15 in the same plot.

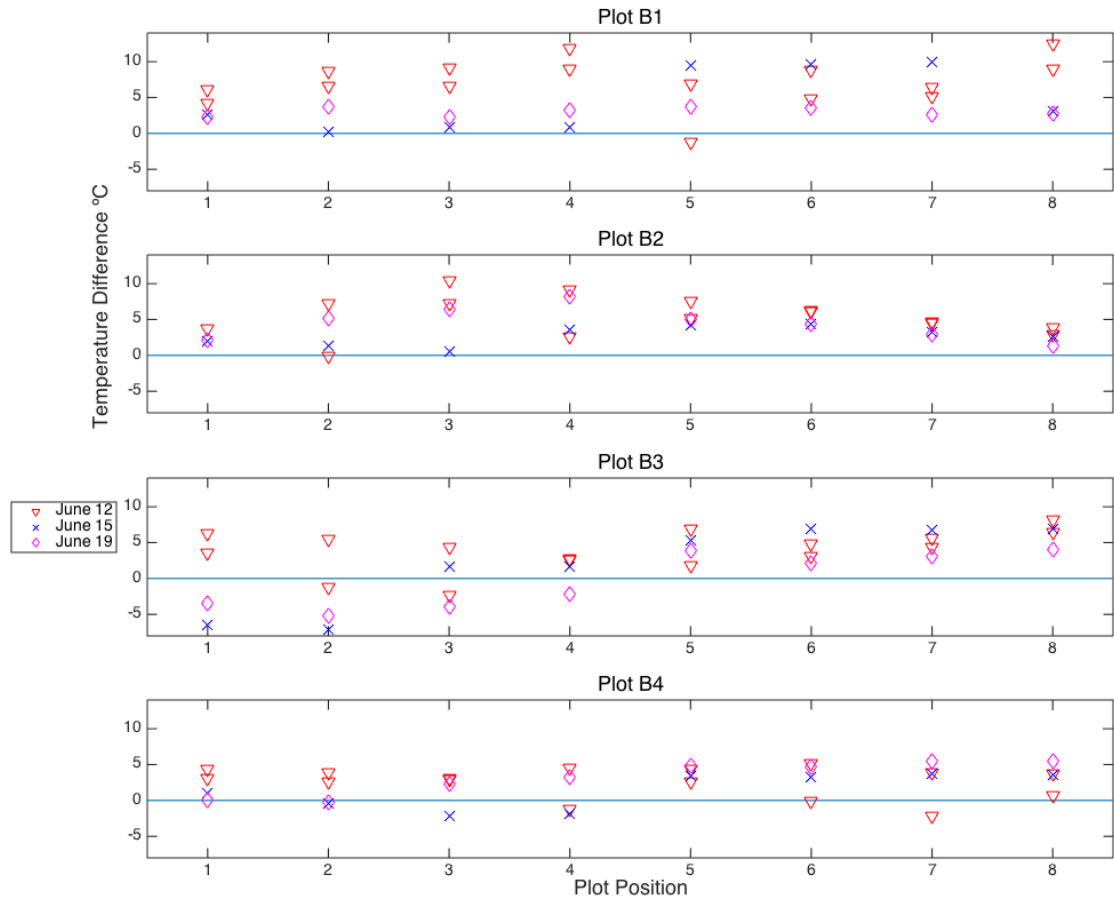


Figure 4.23. The difference between the median of the segmented temperature and air temperature at the eight locations within each plot is plotted for June 12, 15, and 19. Two measurements at each location are shown for June 12, representing the two separate boom lengths used. See figure 4.3b for location of each point.

Based on examination of figures 4.20-4.24 it appeared that temperature measurements were related, at least on some dates, to topsoil depth and end (north or south) of plots. To determine if these differences were statistically significant, full and segmented LWIR image temperature, percentage of image kept (i.e., percentage cover), and IRT temperature were analyzed as dependent variables at $\alpha=0.05$ using the MIXED procedure of SAS (SAS Institute, Cary, NC). Topsoil depth (TD) and north or south side positioning of the instrument (NS) and their interaction were held as fixed effects and data were analyzed separately by date for the first three dates. NS could not be randomized and was therefore considered a repeated effect in all analyses. Mean separation was conducted using Fisher's protected LSD at $\alpha=0.05$. Table 4.1 shows the significance of the F tests and table 4.2 presents the least squares means and mean separation for each dependent variable.

Table 4.1. Significance of F tests for effects of TD, NS, and their interaction on LWIR median temperatures for segmented and full images, IRT values, and percent of image used in segmentation. For each dependent variable, bolded data are significantly different at $\alpha=0.05$.

Date	Source	P>F			
		Segmented Median	Full Image Median	IRT	Percent Segmented
June 12	TD	0.019	0.002	0.002	0.024
	NS	0.791	0.205	0.039	0.299
	TD x NS	0.282	0.508	0.708	0.256
June 15	TD	0.258	0.047	0.164	0.034
	NS	0.016	0.022	0.892	0.965
	TD x NS	0.406	0.380	0.844	0.428
June 19	TD	0.256	0.128	0.871	0.028
	NS	0.225	0.343	0.041	0.589
	TD x NS	0.121	0.156	0.536	0.856

Table 4.2. Least squares means for LWIR median temperatures for segmented and full images, IRT values, and percent of image used in segmentation. Results are separated by date and classified by TD and NS. Low TD plots B1 and B2 are depth 1, deep TD plots B3 and B4 are depth 2. Measurements taken on the northern side of the plot are listed as 1, south as 2. No interaction terms are shown because no significance was found. For each dependent variable, data within a column with the same superscript are not significantly different at $\alpha=0.05$.

	June 12		June 15		June 19		
Segmented							
Median (°C)	Topsoil Depth	North/South	Topsoil Depth	North/South	Topsoil Depth	North/South	
	1	37.61 ^A	36.29 ^A	33.78 ^A	30.09 ^A	31.15 ^A	29.00 ^A
	2	34.76 ^B	36.08 ^A	31.96 ^A	35.65 ^B	29.09 ^A	31.25 ^A
Full Image Median (°C)							
	1	46.03 ^A	43.05 ^A	37.45 ^A	32.85 ^A	33.40 ^A	30.40 ^A
	2	38.37 ^B	41.34 ^A	33.43 ^B	38.03 ^B	29.55 ^A	32.55 ^A
IRT (°C)							
	1	45.23 ^A	43.80 ^A	36.32 ^A	35.15 ^A	32.37 ^A	30.98 ^A
	2	40.46 ^B	41.89 ^B	34.16 ^A	35.33 ^A	29.74 ^B	31.13 ^A
Percent Cover							
	1	20.56 ^A	22.73 ^A	25.50 ^A	28.40 ^A	34.87 ^A	43.47 ^A
	2	27.09 ^B	24.93 ^A	31.39 ^B	28.49 ^A	49.53 ^B	40.92 ^A

On June 12, TD significantly affected each dependent variable. Due to the heat stress conditions this was expected. TD significantly affected percent cover each day, showing that the larger plants were those growing in the deeper topsoil. On June 15, TD significantly affected full image median, possibly due to the smaller plants in the shallow topsoil plots having less shaded, hotter soil. On June 19, the IRT temperature was the only measurement that was significantly affected by TD.

The effect of NS was not significant on the percentage of crop cover. This suggests the size of the plants did not vary between the two plot ends, and did not cause the discrepancy in temperature measured by LWIR camera. On June 12, NS was significant for IRT measurements, but not for camera data. On June 15, the southern measurements were higher and both LWIR temperatures were significantly affected by north-south orientation, but this was not the case for the IRT measurements. The swings in temperature measured with the camera but not the IRT based upon location, seen in the series plots (fig. 4.18-4.20), were what prompted the test of NS significance. Perhaps this effect could be due to sun being to the south, exposing the plants to more radiation. No significance of the side of the plot was found on June 19.

CONCLUSION

Modifications were made to the MSICC to allow its use on a mobile platform capable of recording in-field measurements on demand. The data logger previously required to communicate with an IRT and provide image time stamps, was removed from the instrument by hardware modification and updating firmware. Without the need for an external data logger, all necessary data could be recorded on a removable storage drive on board the MSICC. An application was written so that a laptop could be used to transmit location data and to trigger measurements through serial commands. This allowed the MSICC to be mounted on a boom above the crop canopy so an operator could capture measurements while moving from location to location.

A wide angle lens with an infrared wavelength cutoff filter was added to the visible camera to make it capable of using color images to form a region of interest

within an image. The distortion introduced by using a much wider lens required an extra step in processing when matching visible and LWIR images. The color images allowed ExG and ExGR vegetative indices to be used for segmentation, instead of monochrome intensity levels as was done in chapter 3. Each index was capable of accurate pixel classification under specific conditions, but each had limitations due to soil color and the amount of vegetation within an image. Replacing the ArduCAM visible camera with an imager capable of capturing uncompressed images would be the next step to improving the visible imaging system. A visible lens better matched to the LWIR camera lens, or more effective geometrical distortion corrections, would help reduce errors in matching the two images.

The mobile MSICC was used to capture in-field temperatures at high spatial resolution in two experimental plots. In plot A, lower plant population count and different antecedent soil conditions created a range of canopy densities that provided conditions to test the effectiveness of segmentation based on vegetative indices. In plot B, the controlled spatial variability of the SPARC plots provided different topsoil depths that influenced crop growth. Temperature measurements taken on the same day varied between plots. These temperature differences were most pronounced on a day with low soil moisture; the lower topsoil depth (5 cm) plots had higher temperatures than those with deeper topsoil (28 and 38 cm).

Further study should focus on using the instrument on days where heat stress would be more evident, because only two days in this study would qualify as such. Mounting the MSICC on a higher platform would allow data to be captured later in the season, increasing the likelihood of heat stress days being captured. The modified system

would need to allow the LWIR camera to image the top of the crop canopy throughout the season, as the height of the imager above the crop directly influenced the quality of the data recorded.

CHAPTER 5

CONCLUSIONS

An instrument that used miniature LWIR and visible cameras to image a crop canopy was built for the purpose of identifying plant temperature within a field of view. To accomplish this, a PCB was designed as a platform to connect both imagers to a microprocessor that automated tasks such as displaying and recording images. The PCB allowed the performance of a dual camera system to be tested in the laboratory and the field.

To make the LWIR images into thermal images, a calibration procedure was performed using circulating water as an emissive source. The water was a uniform target that could be heated, while the PCB was able to set the desired camera temperature by a thermoelectric module on the LWIR camera housing. Within the limits of expected field conditions, 20 to 40°C, a quadratic model that estimated scene temperature based on internal and external camera temperature, and camera pixel values exhibited a RMSE of 0.65°C on a separate validation set.

Initially, the MSICC was a static instrument that recorded images in a fixed location in three separate plots in September 2016. Deployed along with a data-logger and an IRT, it was capable of recording temperature of a crop canopy with high temporal resolution. Pixels within the visible camera images were identified as plant or soil based on a monochrome intensity algorithm. The binary mask created from this algorithm was then applied to the thermal images to segment and provide a final crop-only temperature measurement. The segmentation algorithm had varying levels of effectiveness in identifying a plant within a scene, but performed best when soil was visible within the

field of view. When the image was only of a plant canopy, the algorithm separated shaded parts of the plant from those exposed to direct sunlight.

Modifications were made to configure the MSICC to record images and IRT temperature on a removable storage card on board the MSICC without a data-logger. The MSICC was mounted on a mobile boom and used serial commands sent from a laptop to trigger image capture. This allowed the MSICC to be suspended above the crop canopy, while an operator could capture measurements on demand to increase the spatial resolution of measurements.

The addition of an infrared band cutoff filter to the visible camera made it capable of using more complex algorithms to determine plant pixels. A region of interest within the LWIR camera field of view was identified with the visible camera using color based vegetative indices, ExG and ExGR, instead of monochrome intensity. Each index was capable of accurate pixel classification under specific conditions, but both were limited by soil color and amount of vegetation within an image. The ExG index worked well with reflective soil and low percentages of crop within an image, while ExGR functioned best when vegetation covered most of the image.

To capture in-field temperatures at high spatial resolution, the mobile MSICC recorded measurements at pre-defined positions within two experimental plots. In the first plot, reduced plant population and different antecedent soil conditions created a crop with varying growth stages and plant sizes. The second set of plots provided different topsoil depths which resulted in varying plant available water conditions. Temperature measurements taken on the same day varied between plots. These temperature differences

were pronounced on a day with low soil moisture; the lower topsoil depth (5 cm) plots had higher temperatures than the plots with deeper topsoil (28 and 38 cm).

Suggestions for Further Study

Improvements could be made to the current system without a complete design overhaul. Obtaining temperature measurements in real-time would require additional processing power not capable of being implemented with a single microprocessor. While converting the LWIR image to thermal values could be done with the current hardware, the visible image segmentation process is computationally intensive. A processor dedicated to the visible image system would be able to create a binary mask without the need of post-processing.

Future development of the MSICC would be aided by a change in the visible camera and lens pair. The current camera, the ArduCAM, is inexpensive but it provided limited speed and produced compressed images that were not ideal for applying vegetative indices for segmentation. The use of a component level camera with more powerful image processing built in would improve the MSICC dramatically. Initial testing was done with the Open MV (OpenMV, LLC, Atlanta, GA) camera, which has its own ARM processor capable of real-time image processing. The ExG or ExGR algorithms could be implemented on the raw images captured by the camera, negating some of the limitations that the ArduCAM JPEG files presented. The OpenMV camera is also capable of being integrated into the current MSICC design, limiting the amount of development needed. The Open MV camera has only 0.31 megapixels because real-time processing limits the resolution of the visible camera sensor. A visible lens better

matched to the LWIR camera lens, or more effective geometrical distortion corrections, would help reduce errors in matching the two images. This is an aspect of the relatively high-resolution sensor of the ArduCAM that was helpful, because distortions could be corrected without sacrificing too much resolution.

The FLIR Lepton camera, while its resolution was only 80x60 pixels, was the backbone of the MSICC. It provided enough resolution to segment images into plant and non-plant areas and to come up with a single plant temperature. However, when matching the LWIR camera with the visible image, this low resolution created some issues when down-scaling the visible image to match. The interpolation and distortion correction implemented on only the visible lens created misaligned pixels on the edges of vegetation. An updated version of the Lepton is available at four times the resolution (160x120 pixels) of the one used, and would be better able to be corrected. Although parallax would still be present, correcting both the LWIR and visible image for distortion would lead to a better matched image. The updated Lepton camera could be used with the current MSICC hardware, but its additional resolution would require more processing time.

As developed and tested, the MSICC would be a useful tool for monitoring temperature of a crop canopy on a static or slow moving platform, such as a center pivot irrigation system. Adding image processing to firmware would be possible, decreasing the turn-around time for measurements and making it possible to report singular temperatures from an image taken while in the field.

Further field study should focus on using the instrument on days where heat stress would be more evident, because only two such days were part of the dataset collected

here. When testing the mobile instrument, only the early growth stages of a corn crop were able to be measured. Mounting the MSICC on a higher platform would allow data to be captured later in the season, increasing the likelihood of heat stress days being captured. The top of the canopy would need to always be encompassed in the LWIR camera field of view, as the height of the imager above the canopy directly influenced the quality of the data recorded.

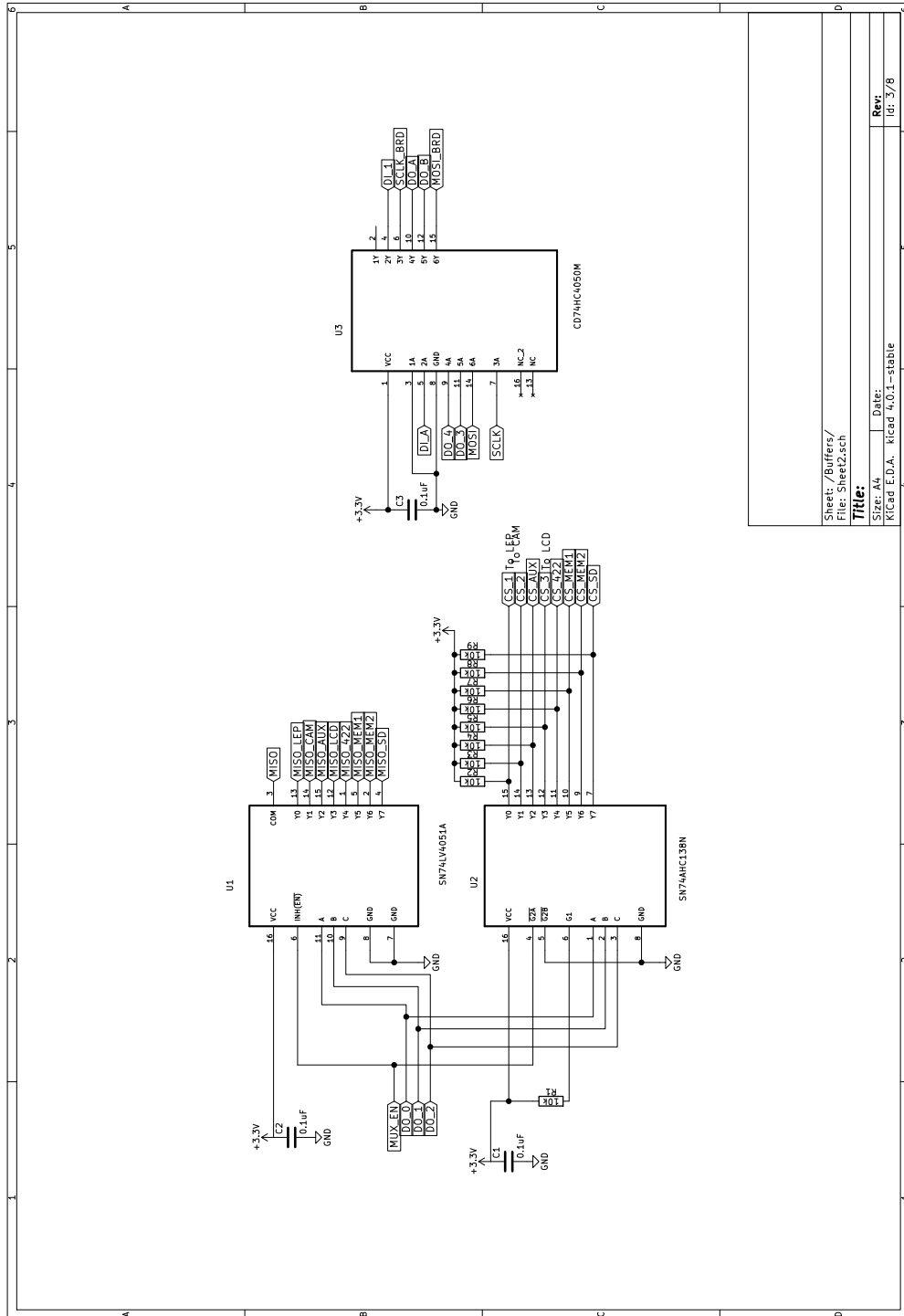
APPENDIX 1

ELECTRONIC SCHEMATICS

MSICC Schematic

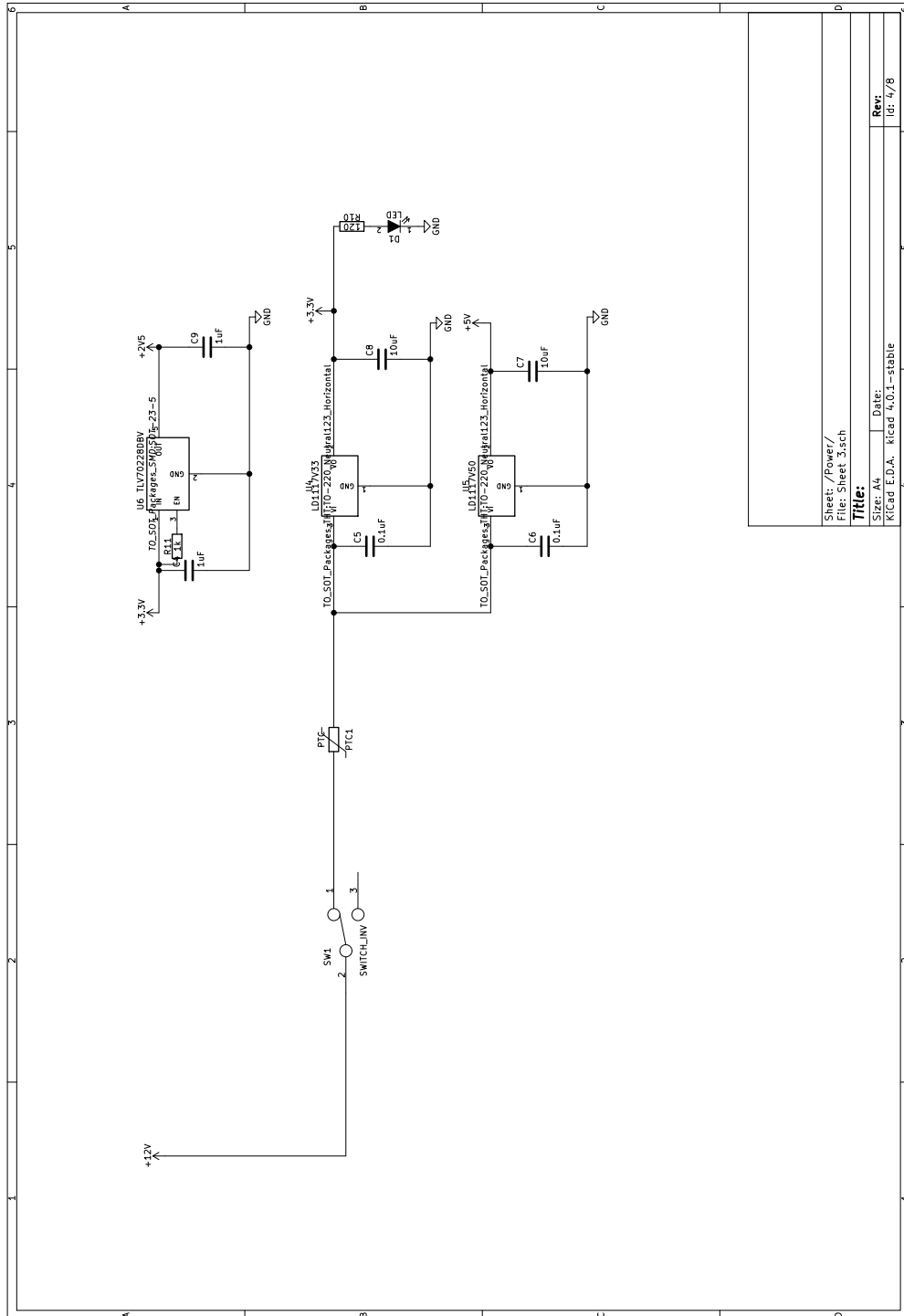
- Connectors
- Buffers
- Power
- Translation
- Memory
- Output Serial Signals
- Output Connectors

Buffers:



Sheet: /Buffers/
 File: Sheet2.sch
Title:
 Size: A4 Date:
 K/Cad E.D.A. - k/cad 4.0.1 - stable
 Rev:
 Id: 3/8

Power:



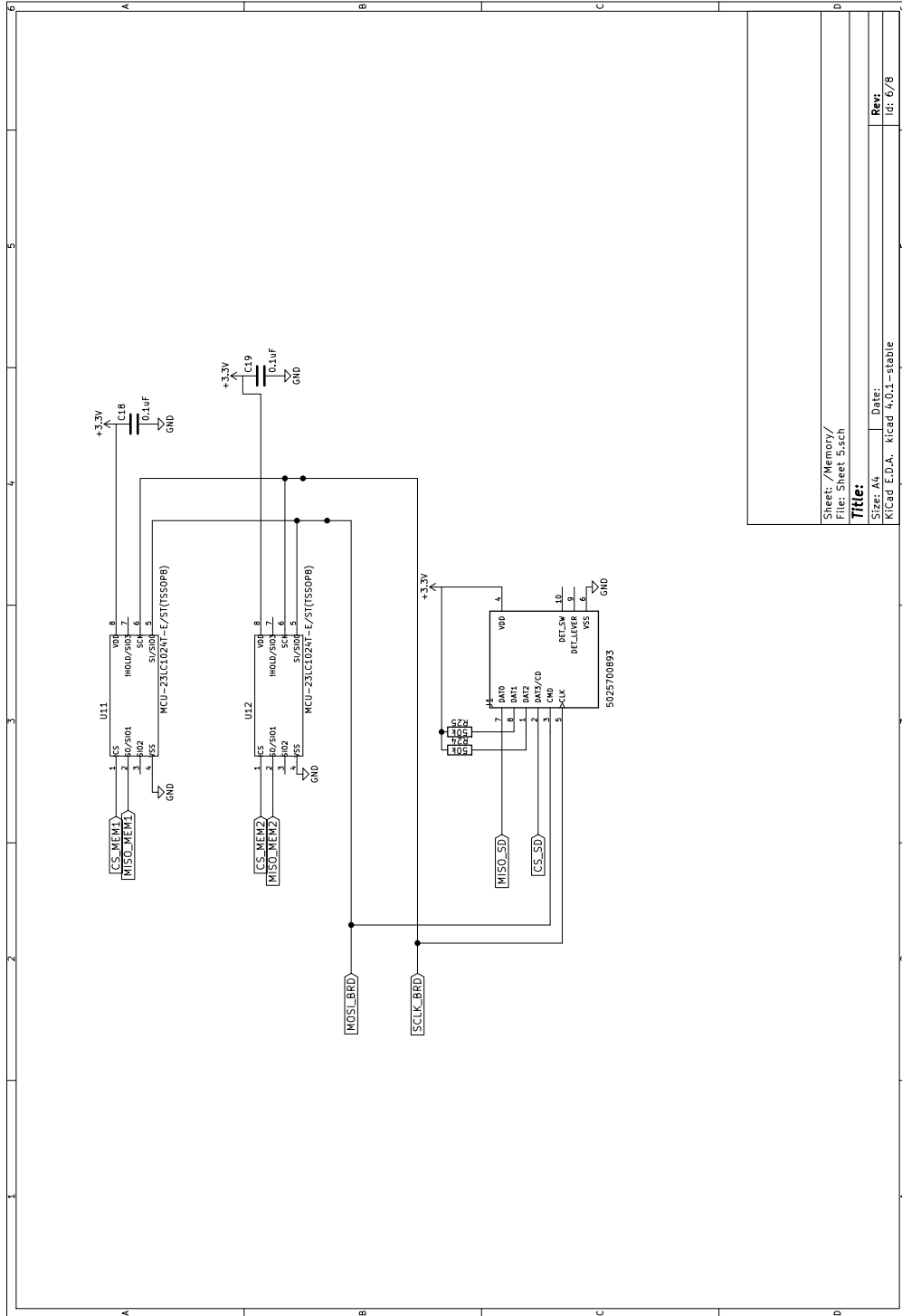
Sheet: /Power/
File: Sheet 3.sch

Title:

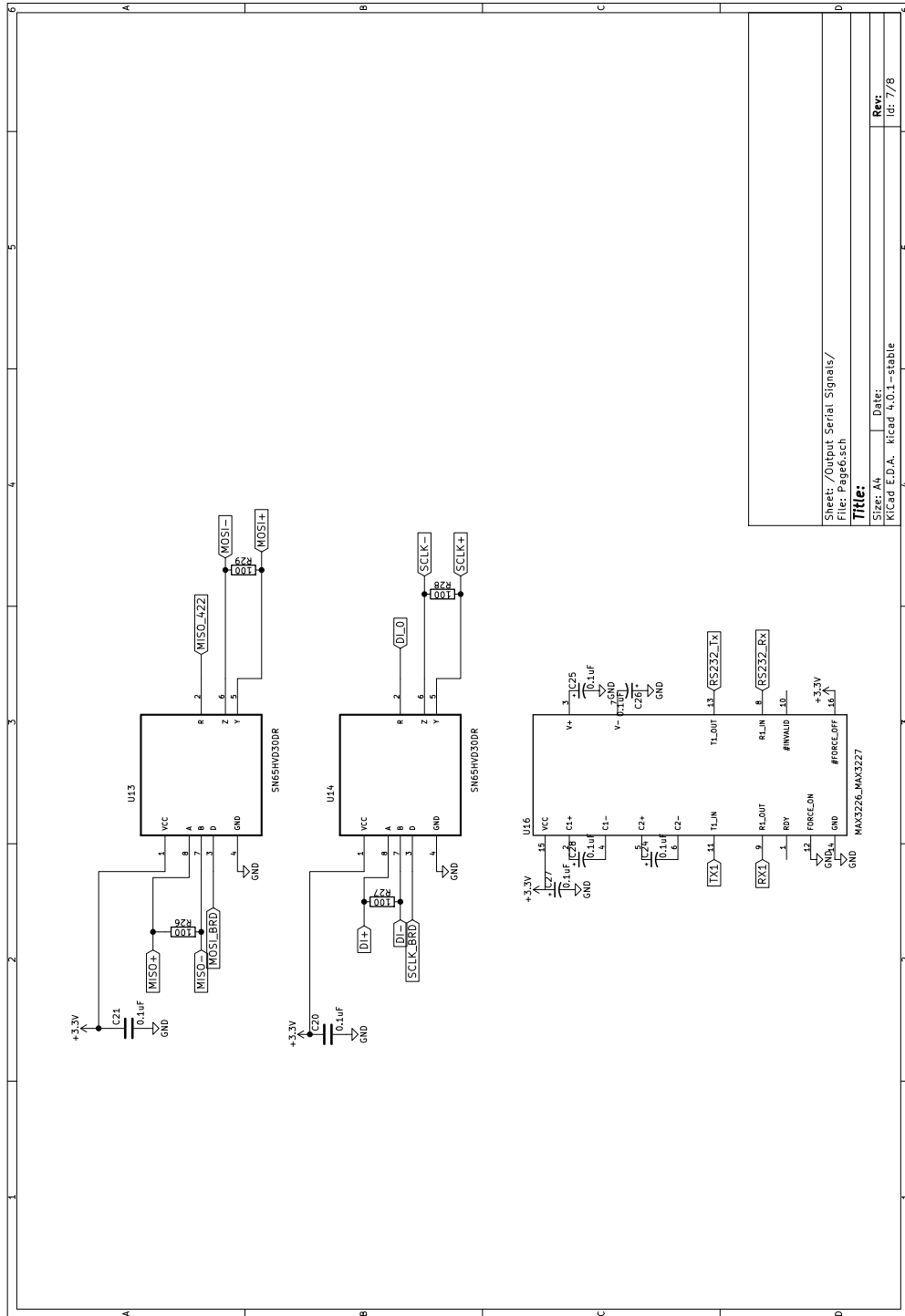
Size: A4 Date:
Kicad E.D.A. Kicad 4.0.1-stable

Rev:
Id: 4/8

Memory:



Output Serial Signals:



Sheet: /Output Serial Signals/
File: Page6.sch

Title:

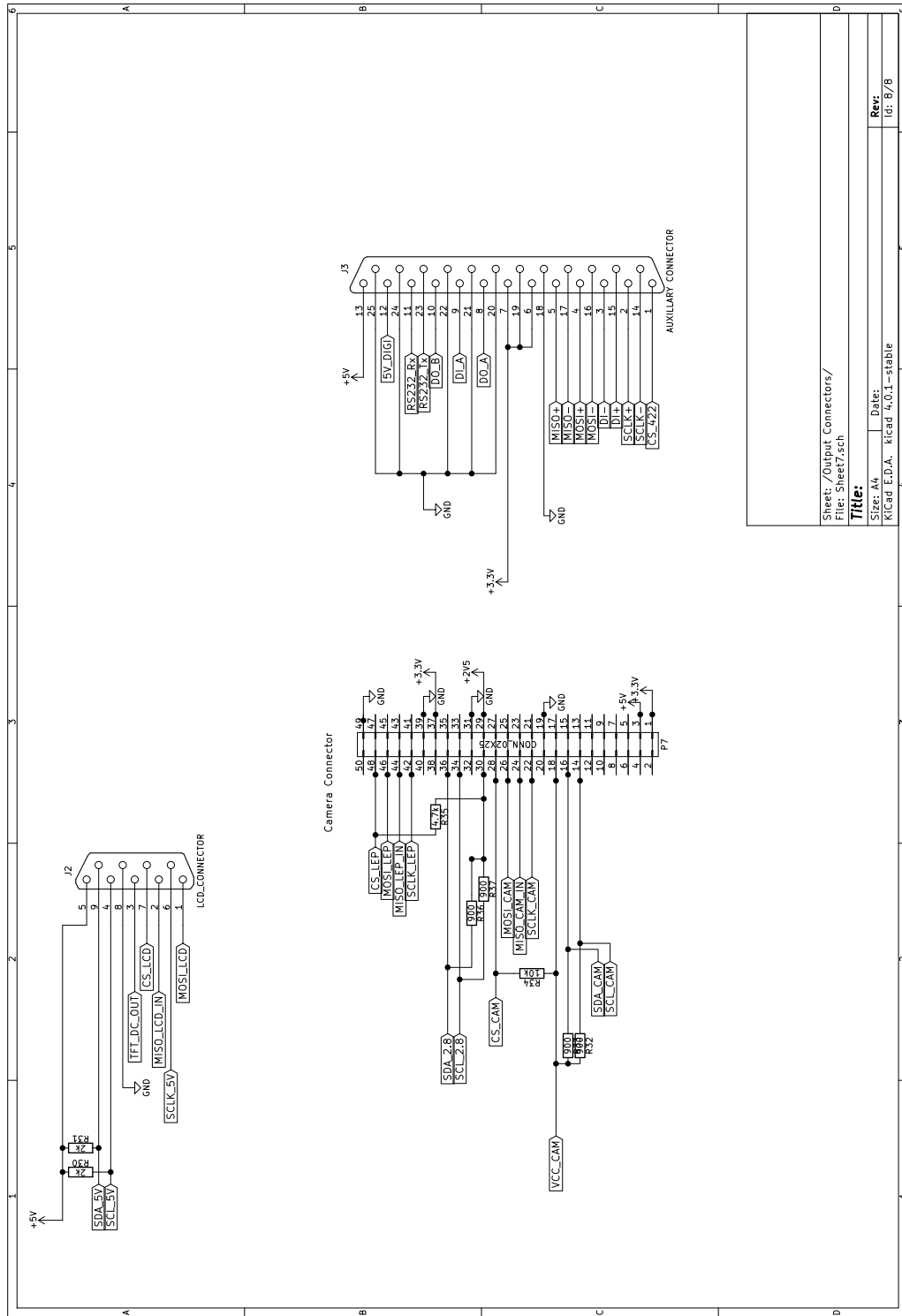
Size: A4 Date:

KiCad E.D.A. - KiCad 4.0.1 - stable

Rev:

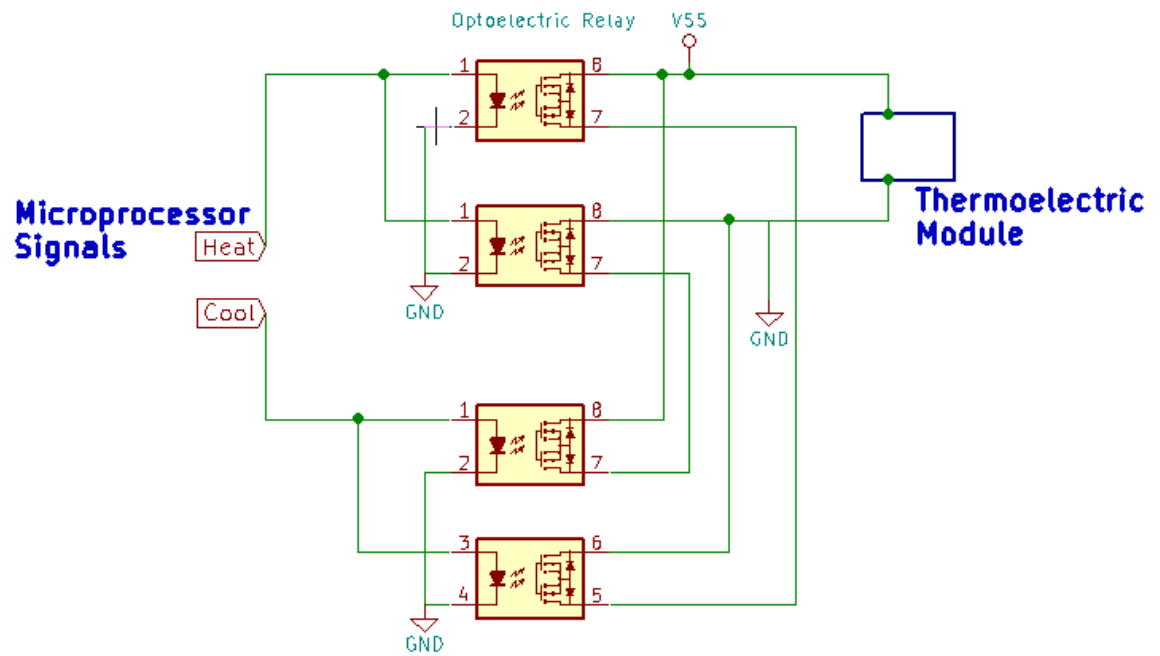
Id: 7/8

Output Connectors:



Sheet: /Output Connectors/
 File: Sheet7.sch
Title:
 Size: A4
 Date:
 R/Cad E.D.A. kicad 4.0.4-stable
 Rev: 8/8
 Id: 8/8

Thermoelectric module control system schematic



Thermoelectric module: CUI Inc. CP20251 2.0 A Peltier Module

APPENDIX 2

SOFTWARE REFERENCES

Table A.1 List of open source code that was used to build MSICC firmware and post-processing algorithms in MATLAB

Name	Type	Author	Location	Modifications made to code	Description
ArduCAM	Library	ArduCAM	https://github.com/ArduCAM	Chip select pins for SPI communication for use with MSICC PCB	Driver for ArduCAM, used to control camera and capture images
Adafruit_ILI9341	Library	Adafruit Inc.	https://github.com/adafruit	Chip select pins for SPI communication for use with MSICC PCB	Hardware driver for Adafruit LCD display
Adafruit_GFX	Library	Adafruit Inc.	https://github.com/adafruit	Chip select pins for SPI communication for use with MSICC PCB	Driver for graphics used on Adafruit LCD display
SDI12	Library	Colin Duffy	https://github.com/duff2013/SDI12_T3	Modified addressing to use UART3 from Teensy	SDI communication software
read_frame	Function	Max Ritter	https://github.com/maxritter/DIY-Thermocam	Chip select pins for SPI communication for use with MSICC PCB	Procedure to capture frames from Lepton camera over SPI and image compilation
Lens_Distort	Matlab Function	Jaap de Vries	https://www.mathworks.com/matlabcentral/fileexchange/37980-barrel-and-pincushion-lens-distortion-correction	Distortion set at -0.12 for 2.8 mm lens	Corrects geometrical distortion of visible images

LIST OF REFERENCES

- Adamchuk, V. I., Viscarra Rossel, R. A., Sudduth, K. A., & Schulze Lammers, P. (2011). Sensor fusion for precision agriculture. In: *Sensor Fusion: Foundation and Applications* (pp. 27-40). Rijeka, Croatia: InTech Open Access Publisher.
- Bartholic, J. F., Namkem, L. N., & Wiegand, C. L. (1972). Aerial thermal scanner to determine temperatures of soils and of crop canopies differing in water stress. *Agronomy Journal*, 64(5), 603-608.
- Bockhold, D. L., Thompson, A. L., Sudduth, K. A., & Henggeler, J. C. (2011). Irrigation scheduling based on crop canopy temperature for humid environments. *Transactions of the ASABE*, 54(6), 2021-2028.
- Bower, S. M., Kou, J., & Saylor, J. R. (2009). A method for the temperature calibration of an infrared camera using water as a radiative source. *Review of Scientific Instruments*, 80(9), 095107.
- Budzier, H., & Gerlach, G. (2015). Calibration of uncooled thermal infrared cameras, *J. Sensors and Sensor Systems*, 4, 187-197.
- Bugbee, B., Droter, M., Monje, O., & Tanner, B. (1998). Evaluation and modification of commercial infra-red transducers for leaf temperature measurement. *Advances in Space Research*, 22(10), 1425-1434.
- Clarke, T. R. (1997). An empirical approach for detecting crop water stress using multispectral airborne sensors. *HortTechnology*, 7(1), 9-16.

Cohen, Y., Alchanatis, V., Meron, M., Saranga, Y., & Tsipris, J. (2005). Estimation of leaf water potential by thermal imagery and spatial analysis. *Journal of Experimental Botany*, 56(417), 1843-1852.

Conway, L. S., Yost, M. A., Kitchen, N. R., Sudduth, K. A., Thompson, A. L., & Massey, R. E. (2017). Topsoil thickness effects on corn, soybean, and switchgrass production on claypan soils. *Agronomy Journal*, 109(3), 782-794.

DeWitt, D. P., & Nutter, G. D. (Eds.). (1988). *Theory and practice of radiation thermometry* (pp. 520-521). New York: Wiley.

Fuchs, M., & Tanner, C. B. (1966). Infrared thermometry of vegetation. *Agronomy Journal*, 58(6), 597-601.

Gantzer, C. J., & McCarty, T. R. (1987). Predicting corn yields on a claypan soil using a soil productivity index. *Trans. ASAE*, 30(5), 1347-1352.

Gonzalez-Dugo, V., Zarco-Tejada, P., Berni, J. A., Suárez, L., Goldhamer, D., & Fereres, E. (2012). Almond tree canopy temperature reveals intra-crown variability that is water stress-dependent. *Agricultural and Forest Meteorology*, 154, 156-165.

Gonzalez-Dugo, V., Goldhamer, D., Zarco-Tejada, P. J., & Fereres, E. (2015). Improving the precision of irrigation in a pistachio farm using an unmanned airborne thermal system. *Irrigation Science*, 33(1), 43-52.

Guijarro, M., Pajares, G., Riomoros, I., Herrera, P. J., Burgos-Artizzu, X. P., & Ribeiro, A. (2011). Automatic segmentation of relevant textures in agricultural images.

Computers and Electronics in Agriculture, 75(1), 75-83.

Hamuda, E., Glavin, M., & Jones, E. (2016). A survey of image processing techniques for plant extraction and segmentation in the field. *Computers and Electronics in*

Agriculture, 125, 184-199.

Han, M., Zhang, H., DeJonge, K. C., Comas, L. H., & Trout, T. J. (2016). Estimating maize water stress by standard deviation of canopy temperature in thermal imagery.

Agricultural Water Management, 177, 400-409.

Jackson, R.D., Idso, S.B., Reginato, R.J., & Pinter Jr., P.J. (1981). Canopy temperature as a crop water stress indicator. *Water Resources Research*, 17(4), 1133-1138.

Lee, W. S., Alchanatis, V., Yang, C., Hirafuji, M., Moshou, D., & Li, C. (2010). Sensing technologies for precision specialty crop production. *Computers and Electronics in*

Agriculture, 74(1), 2-33.

Mangus, D. L., Sharda, A., & Zhang, N. (2016). Development and evaluation of thermal infrared imaging system for high spatial and temporal resolution crop water stress

monitoring of corn within a greenhouse. *Computers and Electronics in Agriculture*, 121, 149-159.

- Meyer, G. E., Hindman, T. W., & Lakshmi, K. (1999). Machine vision detection parameters for plant species identification. In G.E. Meyer & J.A. DeShazen (Ed.) Precision agriculture and biological quality, Proc SPIE Vol. 3543, pp.327-335.
- Meyer, G. E., & Neto, J. C. (2008). Verification of color vegetation indices for automated crop imaging applications. *Computers and Electronics in Agriculture*, 63(2), 282-293.
- Möller, M., Alchanatis, V., Cohen, Y., Meron, M., Tsipris, J., Naor, A., ... & Cohen, S. (2007). Use of thermal and visible imagery for estimating crop water status of irrigated grapevine. *Journal of Experimental Botany*, 58(4), 827-838.
- Moran, M. S., Clarke, T. R., Inoue, Y., & Vidal, A. (1994). Estimating crop water deficit using the relation between surface-air temperature and spectral vegetation index. *Remote Sensing of Environment*, 49(3), 246-263.
- Mulla, D. J. (2013). Twenty five years of remote sensing in precision agriculture: Key advances and remaining knowledge gaps. *Biosystems Engineering*, 114(4), 358-371.
- Nielsen, D. C. (1990). Scheduling irrigations for soybeans with the Crop Water Stress Index (CWSI). *Field Crops Research*, 23(2), 103-116.
- Nugent, P. W., Shaw, J. A., & Pust, N. J. (2013). Correcting for focal-plane-array temperature dependence in microbolometer infrared cameras lacking thermal stabilization. *Optical Engineering*, 52(6), 061304-061304.

O'Shaughnessy, S. A., Evett, S. R., Colaizzi, P. D., & Howell, T. A. (2011a). Using radiation thermography and thermometry to evaluate crop water stress in soybean and cotton. *Agricultural Water Management*, 98(10), 1523-1535.

O'Shaughnessy, S. A., Hebel, M. A., Evett, S. R., & Colaizzi, P. D. (2011b). Evaluation of a wireless infrared thermometer with a narrow field of view. *Computers and Electronics in Agriculture*, 76(1), 59-68.

O'Shaughnessy, S. A., Evett, S. R., Colaizzi, P. D., & Howell, T. A. (2012). A crop water stress index and time threshold for automatic irrigation scheduling of grain sorghum. *Agricultural Water Management*, 107, 122-132.

O'Shaughnessy, S. A., Evett, S. R., Colaizzi, P. D., & Howell, T. A. (2013). Wireless sensor network effectively controls center pivot irrigation of sorghum. *Applied Engineering in Agriculture*, 29(6), 853-864.

Otsu, N. (1979). A threshold selection method from gray-level histograms. *IEEE Transactions on Systems, Man, and Cybernetics*, 9(1), 62-66.

Perez, A. J., Lopez, F., Benlloch, J. V., & Christensen, S. (2000). Colour and shape analysis techniques for weed detection in cereal fields. *Computers and Electronics in Agriculture*, 25(3), 197-212.

Sadler, E. J., Camp, C. R., Evans, D. E., & Millen, J. A. (2002). Spatial variation of corn response to irrigation. *Transactions of the ASAE*, 45(6), 1869-1881

Scharf, P. C., Shannon, D. K., Palm, H. L., Sudduth, K. A., Drummond, S. T., Kitchen, N. R., ... & Oliveira, L. F. (2011). Sensor-based nitrogen applications out-performed producer-chosen rates for corn in on-farm demonstrations. *Agronomy Journal*, 103(6), 1683-1691.

Tanner, C. B. (1963). Plant temperatures. *Agronomy Journal*, 55(2), 210-211.

Van Bavel, C. H., Nakayama, F. S., & Ehrlert, W. L. (1965). Measuring transpiration resistance of leaves. *Plant Physiology*, 40(3), 535.

Wanjura, D. F., Upchurch, D. R., & Mahan, J. R. (1995). Control of irrigation scheduling using temperature-time thresholds. *Transactions of the ASAE*, 38(2), 403-409.

Wiegand, C. L., & Namken, L. N. (1966). Influences of plant moisture stress, solar radiation, and air temperature on cotton leaf temperature. *Agronomy Journal*, 58(6), 582-586.

Woebbecke, D. M., Meyer, G. E., Von Bargen, K., & Mortensen, D. A. (1995). Color indices for weed identification under various soil, residue, and lighting conditions. *Transactions of the ASAE*, 38(1), 259-270.

Zia, S., Romano, G., Spreer, W., Sanchez, C., Cairns, J., Araus, J. L., & Müller, J. (2013). Infrared thermal imaging as a rapid tool for identifying water-stress tolerant maize genotypes of different phenology. *Journal of Agronomy and Crop Science*, 199(2), 75-84.